A DISSERTATION

FOR THE DEGREE OF DOCTOR OF PHILOSPHY

Synthesis of Functional Nanostructured and Nanocomposite Materials for Printed Electronic Devices

Ghayas Uddin Siddiqui

Department of Mechatronics Engineering

GRADUATE SCHOOL

JEJU NATIONAL UNIVERSITY

2017. 08

Synthesis of Functional Nanostructured and Nanocomposite Materials for Printed Electronic Devices

Ghayas Uddin Siddiqui

(Supervised by Professor Kyung Hyun Choi)

A thesis submitted in partial fulfillment of the requirement for the degree of Doctor of Philosophy

2017. 06

The thesis has been examined and approved.

Thesis director, Jong-Hwan Lim, Professor, Department of Mechatronics Engineering

Yang-Hoi Doh, Professor, Department of Electronic Engineering

Chul-Ung Kang, Professor, Department of Mechatronics Engineering

Chang-Nam Kang, Professor, Department of Mechanical Engineering

Kyung-Hyun Choi, Professor, Department of Mechatronics Engineering

June 2017

Date

Department of Mechatronics Engineering
GRADUATE SCHOOL
JEJU NATIONAL UNIVERSITY
REPUBLIC OF KOREA

Dedicated to

My Beloved Parents

Acknowledgments

The first and foremost gratitude to my Almighty Allah Who Bestows His Grace on me in every phase of my life and then to my beloved parents as they have continued to shower their prayers and most precious love for me even after departing the world. I miss them intensely in every step of my life and their immortal love makes me more and more strong.

I am immensely grateful to my supervisor Prof. Dr. Kyung Hyun Choi for his skillful guidance, support and confidence on me throughout my stay at Advance Micromechatronics (AMM) lab. It has been an honor for me to work under his supervision as he has always provided decent funding, accurate direction, and motivation to flourish my research.

I am very thankful to Ms. Qamar Naz and Dr. Nauman Malik for believing in me and recommending me in AMM lab. I would like to say a special thanks to my younger brother Waqas Uddin Siddiqui who managed all the family matters so nicely in my absence. An adorable gratitude to my loving sisters, sweet nephews and nieces who bless me always with their prayers and love. I am also very thankful to my uncles, aunts and cousins for their affectionate countenance even when I was unable to contact them oftenly.

I will always be grateful to my seniors in AMM lab including Dr. Maria Mustafa, Dr. Adnan Ali, Dr. Navaneethan, Dr. Muhammad Zubair, Dr. Syed Murtaza, Dr. Kamran Ali, Dr. Junaid Ali, and Dr. Shahid Aziz as I have learned a lot from them. I am fortunate enough to have Memoon Sajid, Muhammad Muqeet Rehaman, Jahanzeb Gul, J. Srikanth, Imran Shah, Muhammad Mutee ur Rehman, Shital Kumar and Muhsin Ali as my dear friends and in AMM lab as they are nothing short of amazing persons.

I am very thankful to my Korean friends and colleagues including Dr. Hyun Woo Dong, Dr. Bong Su Yang, Dr. Young Jin Yang, Go-Bum Kim, Hyeon Beom Kim, Soo Wan Kim, Young

Soo Kim, Hyu Tae Kim, Kyung Huwan, Jae Wook, Dae-You Kim, Ms. Jae Hee Park and Ms. Jiyun; without their assistance my stay at Jeju would not have been so comfortable and pleasant.

I am really grateful to my dear friends in Jeju including Waqar Kayani Sahab, Dr. Jamil Ahmed, Dr. Farrukh Israr, Dr. Safdar Ali, Dr. Rashid Ahmed, Dr. Zahid Manzoor, Dr. Sohail khan, Dr. Shawkat Ali, Dr. Waqar Abbasi, Dr. Afaq Muhammad, Dr. Anil Kumar, Dr. Karthi Krish, Dr. Konstantin Lyakhov, Aleem Khaliq, Zubair Amjad, Irshad Ali, Waseem Abbas, Gul Hassan Khan, Muhammad Arshad, Fasihullah Khan, Rafiq Mansoor, Fazli Wahid, Israr Ullah, Muhammad Fayaz, Khurram Javed, Adeel Farooq, Tahir Abbas, Muhammad Umair, Kanak Kanti Kar and Shahin Ur Rehman. These all wonderful people have impact of best memories in my life and will be remembered by me forever in my pleasant memories.

I have surely missed many names but I would like to thank all who even have tiny contribution in my success.

Ghayas Uddin Siddiqui

Table of Contents

List of Figures

List of Tables

Abstract

There has been growing interest in the field of nanotechnology during the last two decades and nanostructured materials have the enormous contribution in this development. After the progress in synthesis of nanostructured materials, their functional characteristics were investigated and thus peculiar optical, chemical, electrical, mechanical and magnetic properties have been exploited. These nanostructured materials can be tailored to obtain desired characteristics by making their nanocomposites with various organic polymers or inorganic nanoparticles and their usage as thin films and coatings can further explore their applications in several fields.

This thesis reports a complete study based on synthesis, characterization, ink preparation, thin film fabrication and applications of functional nanostructured and nanocomposite materials.

In this study, various low dimensional functional nanostructured materials have been synthesized and developed including zero dimensional (0D) molybdenum sulfide (MoS_2) quantum dots (QDs), one dimensional (1D) zinc oxide (ZnO) nanowires (NWs), two dimensional (2D) MoS_2, and hexagonal boron nitride (hBN) nanosheets; and three dimensional (3D) zinc stannate ($ZnSnO_3$) nanocubes (NCs). Moreover, the nanocomposites of as synthesized low dimensional nanostructured materials have also been reported that include nanocomposite of $ZnSnO_3$/PMMA, $ZnSnO_3$/PVOH, hBN/PVOH, ZnO/$ZnSnO_3$, and MoS_2-PEDOT:PSS. Applications of these nanostructures and nanocomposite materials have been presented by fabricating non-volatile resistive switching and humidity sensing devices using printing techniques like EHDA, reverse offset, SAW-EHDA, RPC, and EHD patterning. The morphological, structural, chemical, and optical characteristics of nanostructured and nanocomposite materials were analysed by using different characterization techniques like HR-TEM, FE-SEM, AFM, XRD, Raman, FTIR, EDX and UV/VIS spectroscopy. Furthermore, the

electrical and mechanical results have also been reported to show the performance and mechanical robustness of the fabricated devices.

Chapter -1. Introduction

1.1 Functional Nanostructured materials

Nanostructured materials are the materials having at least one dimension lies between 1-100 nm in their structure. These may have various electronic nature based upon their electronic structure including conducting, semiconducting or dielectric so they may be termed as functional nanostructured materials. The synthesis of nanostructured materials is immensely significant research in the field of nanotechnology and captivating a large number of researchers. Their characterization and thin film fabrication for various devices has exploited numerous potential applications such as light emitting devices, memory devices, thin film transistors, photovoltaic devices, humidity sensors and bio-sensors.

1.2 Low-dimensional nanomaterials

Beside the composition and arrangement of atoms in materials, dimensionality plays a vital role in determining their fundamental characteristics. On the basis of dimension, nanostructured materials are categorized as 0D, 1D, 2D and 3D materials.

1.2.1 Zero-dimensional materials: Quantum dots

During the last two decades, a great deal of attention has been focused on quantum dots (zero-dimensional) which are few nanometre-scale (1-10 nm in diameter) [1] crystals of semiconducting materials. They have entirely different electronic, spectroscopic, and photophysical properties from their bulk because of quantum confinement and edge effects. Quantum dots (QDs) are being intensively investigated for applications such as light-emitting diodes, solid-state lighting, lasers, and solar cells. One useful feature of quantum dots is that the colors of light they absorb and emit can be tuned simply by varying their size [2], and this is because dots of the same material but different sizes have different band gaps, which absorb and emit different frequencies. Each semiconductor has a characteristic band gap, but when the diameter of a piece of the material is shorter than the quantum-mechanical wave function of its

electrons, the "squeezed" electron wave function makes the band gap wider. It means the smaller the quantum dot, the wider the band gap.

1.2.2 One-dimensional materials: Nanowires

One-dimensional nanomaterials may include whiskers, fibers or fibrils, Nanorods and nanowires but we have focused our studies on nanowires. They can be grown on various substrates from rigid to flexible. They exist in many forms including metals, semiconductors, insulators and organic compounds and are being studied for use in electronics, energy conversion, optics and chemical sensing, among other fields. The structure of nanowires is so simple that there is no room for defects, and electrons pass through unimpeded. The electrons and photons within these nanowires experience quantum confinement effects. The diameter of as grown nanowires is of few nanometers but their length can be extended for hundreds of micrometers and because of this, they have high ratio of surface are to volume. This unique characteristic makes them very good detectors, because all that surface area can be treated to bind with specific chemical or biological molecules. The electrical signal generated by that binding can then easily be transmitted along the wire.

1.2.3 Two-dimensional materials: nanosheets or flakes

Two-dimensional materials or layered materials had become very popular after the discovery of graphene and since then the 2D materials are being explored in terms of their exfoliation methods, their electronic properties and their applications. They are consist of two-dimensional platelets weakly stacked to form three-dimensional structures [3]. They have strong in-plane chemical (covalent) bonds within each layer but weak out-of-plane van der Waals bonds. To get the maximum advantage of 2D materials, they must be exfoliated or delaminated to mono or few layers and over the past decade, a number of methods have been introduced that include ultra-sonication [4–6], mechanical cleavage [7–10], Li-intercalation [11,12], and Sodium naphthalenide [13]. The mono or few-layer exfoliated MoS_2 has intriguing applications such as super capacitor [14],

electro catalyst for hydrogen evolution reaction (HER) [15,16], sensor [17], field effect transistor [18,19], and solar cells [20,21].

1.2.4 Three-dimensional Materials: nanocubes

Nanocubes are the cube shaped nanoparticles having size of few nanometers. The distinctive morphology and homogeneity of the nanocubes makes them ideal for use in: surface-enhanced Raman scattering (SERS), metamaterials, plasmonic catalysis and photovoltaics and other energy harvesting devices. $ZnSnO_3$ NCS have been used more oftenly for different application then other nanocubes such as gas sensor, humidity sensor, nanogenerator, memristor and photocatalysis [22–26].

1.3 Nanocomposites

Nanocomposites are combination of two materials usually organic-inorganic based materials that incorporate nanosized particles into a matrix of standard material. Polymer based or organic-inorganic nanocomposite materials are promising systems for a variety of applications due to their extraordinary properties, which arise from the synergism between the properties of the components. There are several routes to these materials, but probably the most prominent one is the incorporation of inorganic nanostructures in organic polymers. These materials have gained much interest due to the remarkable change in properties such as mechanical, [27] thermal, [28] electrical, [29] and magnetic [30] compared to pure organic polymers. They have the combined distinct characteristics of organic and inorganic materials and both type of materials have certain advantages when used in electronic devices. Organic materials are manifold in their properties such as easy and low temperature processing, economical fabrication, high flexibility, and large area fabrication. Inorganic materials have excellent thermal and mechanical stability, high carrier mobilities, and wide range of optical, electrical, magnetic and dielectric properties.

Chapter 2- Synthesis of Nanomaterials and Nanocomposites

2.1. Synthesis of MoS_2 QDs

MoS_2 QDs were prepared by wet grinding followed by mechanical shaking, bath sonication, ultrasound probe sonication and centrifugation. MoS_2 powder was ground in NMP in a mortar for 6 hours; after grinding, the gel like mixture was dried for 1 hour at 100 ℃. The dried MoS_2 powder was then dissolved in equal volumes of NMP and DCB and kept on magnetic stirrer for 30 min followed by mechanical shaking for 4 hours at 300 rpm. Bath sonication of MoS_2 solution was carried out for 4 hours followed by ultrasound probe sonication for 1 hour. After performing these processes, the solution was kept undisturbed for overnight and top 2/3 portion of the MoS_2 solution was carefully taken out for centrifugation. The centrifugation was carried out for 30 min at 8000 rpm and supernatant was obtained by decantation. Thus the solution of MoS_2 QDs was obtained and used for further characterizations. The solution was finally dried in order to calculate the concentration (yield) of as synthesized MoS_2 QDs. The schematic diagram to synthesize MoS_2 QDs is also depicted in Fig. 2.1.

MoS_2 QDs were prepared by wet grinding in NMP assisted bath and probe sonication in NMP and DCB. The color of the bulk MoS_2 solution is dark grey but after performing all the processes it becomes faint yellow as shown in Fig. 2.1.

In fact, the direct dispersion of TMDs in solvents causes the low concentration of mono or few layers [31,5]. Hence, grinding makes a useful effect in exfoliation of layered materials because it generates shear forces to detach the layers of 2D materials. Many organic solvents like N-cyclohexyl-2-pyrrolidone, tetrahydrofuran, ethylene glycol, dimethylformamide, dimethyl sulfoxide, chlorobenzene, pyridine and many others have been used for liquid exfoliation of layered materials but both NMP and DCB are suitable solvents for exfoliation and stable

dispersion of 2D materials [32]. For the better dispersion of TMDs, solvents having surface tension values in range of 40 mN/m to 50 mN/m or surface energy value close to 70 mN/m are

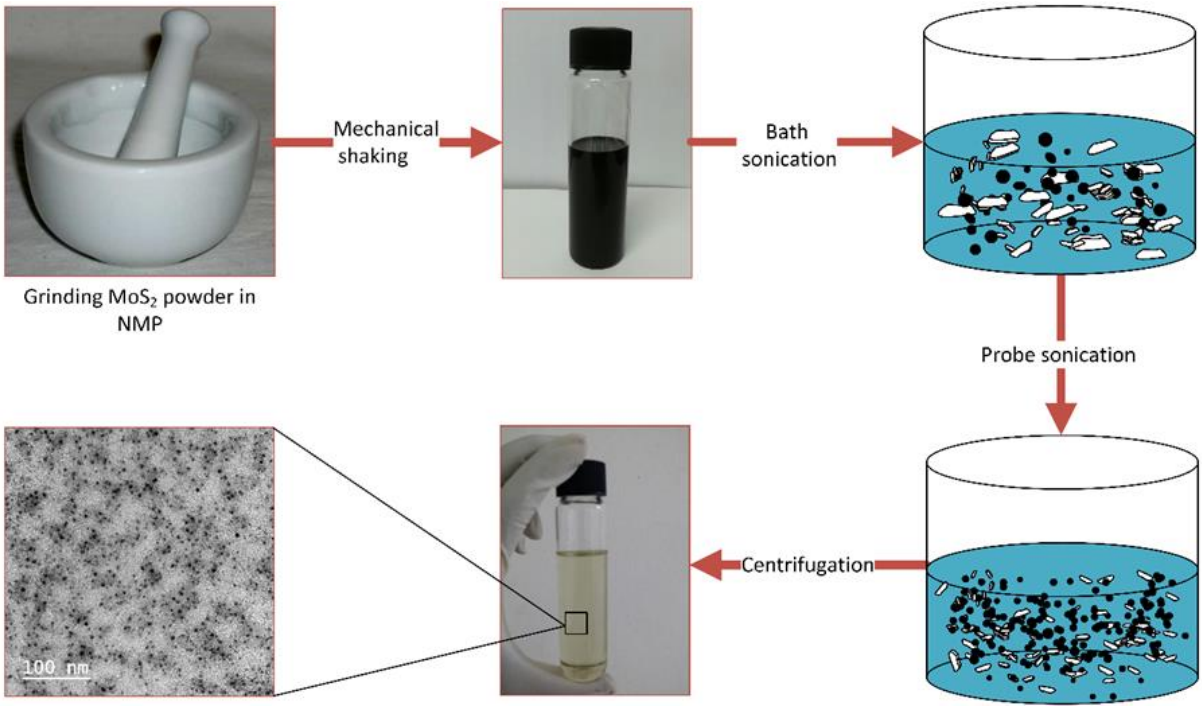

Fig. 2.1. Schematic diagram for the synthesis of MoS_2 QDs consist on wet grinding in NMP followed by mechanical shaking for 4 h, bath sonication for 4 h, probe sonication for 1 h and centrifugation at 8000 rpm for 30 min.

preferred [5,33]. When surface energy values of organic solvents and TMDs match with each other, a good dispersion is observed [31]. For the synthesis of MoS_2 QDs, ultrafine MoS_2 powder was used because it has smaller flakes, and creates dispersion with smaller particle size whereas micropowder requires more sonication and will result flakes with larger lateral dimensions. In this experiment, we used NMP first for wet grinding and further for dispersion because it acts as a stabilizing agent to avoid the restacking of the MoS_2 nanosheets or nanoparticles [34] while DCB also improves exfoliation, stable dispersion and high concentration of MoS_2 nanosheets [35]. Ultrasound sonication in mixed solvents is an attractive route to exfoliate TMDs [5,36,37]. We also used this strategy to synthesize MoS_2 QDs using bath and probe sonication in NMP and DCB and it was found to be an efficient method because the concentration (yield) of the as synthesized MoS_2 QDs was found to be 7 mg mL^{-1}. During

sonication, the increase in temperature and pressure of the solution results the generation of hydrodynamic forces which cleave larger particles into smaller particles [38].

The size and morphology of the as synthesized MoS2 QDs was measured by HR-TEM. In Fig. 2.2 (a) it can be clearly observed that most of the MoS2 QDs synthesized by this method are very small, uniform in size and their concentration is appreciable as well. The distribution of quantum dots is shown by plotting histogram as shown in Fig. 2.2 (b), (the size is statically calculated from more than 200 QDs in TEM image) all the QDs are ≤ 7.5 nm and majority lies in the range of 2-5 nm which indicates the efficacy of our strategy to synthesize MoS_2 QDs. Typical selected area electron diffraction (SAED) pattern as shown in Fig. 2.2 (c) reveals the six-fold symmetry hexagonal lattice and high crystallinity of MoS_2. In Fig. 2.2 (d) magnified TEM image shows the hexagonal lattice structure and high crystallinity of MoS_2 QDs with lattice spacing of 0.23 nm which corresponds to the (103) plane of MoS_2 and similar to hexagonal pattern of MoS_2 mono or few layer.

Raman spectroscopy is a powerful non-destructive characterization tool in the study of layered materials in which the coupling between electronic structure and phonons is studied. Generally, four phonon modes E^2_{2g}, E_{1g}, E^1_{2g} and A_{1g} are observed in bulk MoS_2 but only two of them E^1_{2g} and A_{1g}, are associated with the thickness of the MoS_2 layer [39]. Generally, in the exfoliated MoS_2 monolayer, E^1_{2g} mode is red-shifted and A_{1g} mode is blue-shifted [2,39,40].

In Fig. 2.3, two phonon modes of pristine MoS_2, E^1_{2g} at 380 cm^{-1} and A_{1g} at 404 cm^{-1} were observed, while these phonon modes were shifted at 382 cm^{-1} (red-shift) and 402 cm^{-1} (blue-shift) in MoS_2 QDs. The results of this study are in well agreement with already reported Raman analysis of exfoliated MoS_2 monolayer [2,39,40]. The E^1_{2g} mode is associated with opposite vibration of two sulfur atoms with respect to molybdenum atom and A_{1g} mode is attributed to the out of plane vibration of sulfur atoms in opposite direction [39].

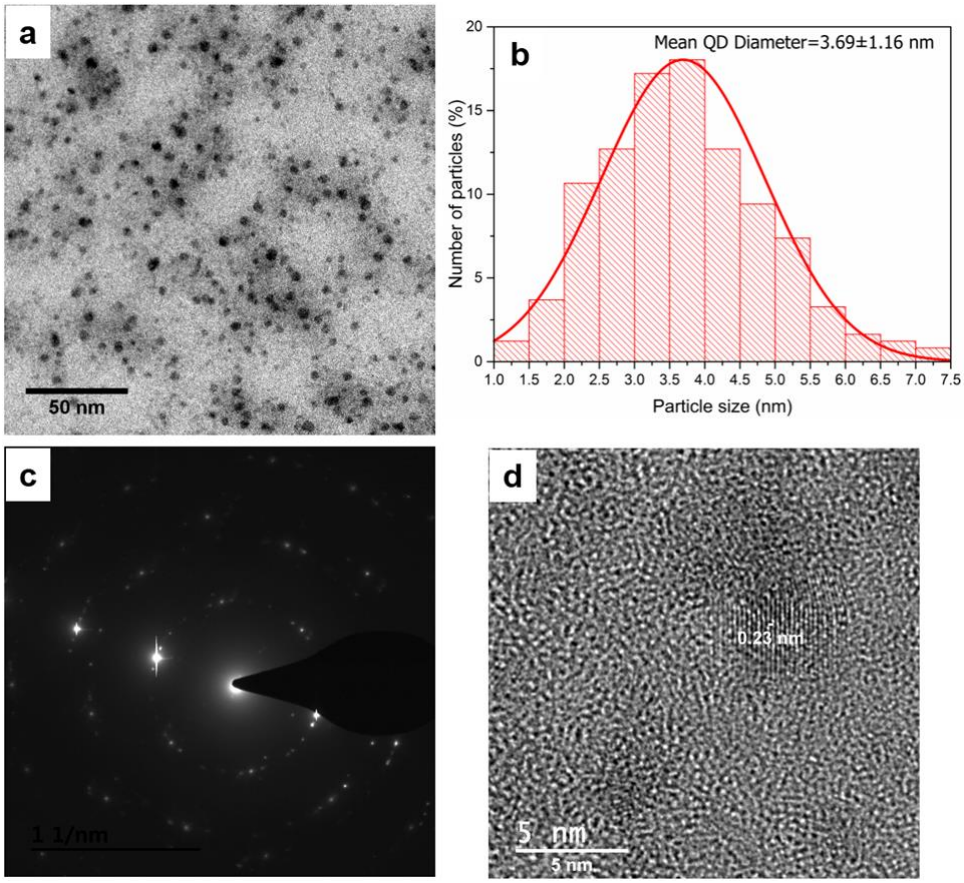

Fig. 2.2. (a) High resolution TEM image of MoS_2 QDs showing good concentration and uniformity. **(b)** Histogram showing the distribution of QDs, most of the QDs are in range of 2-5 nm. **(C)** SAED pattern which reveals the six-fold symmetry hexagonal lattice and high crystallinity of MoS_2 QDs. **(d)** Magnified TEM image showing the lattice spacing 0.23 nm corresponds to (103) plane.

The Raman frequencies of these two phonon modes vary monotonously with the layer numbers of MoS_2 and are reliable features to identify the number of layers with much higher accuracy than the intensities and width of the peaks. The gap between the frequencies of these two phonon modes depends upon the method of exfoliation, a close gap shows that monolayer structure is more prominent. Frequency of the E^1_{2g} mode decreases and A_{1g} mode increases, when number of layers of MoS_2 are increased [41,42].

The optical properties of as synthesized MoS_2 QDs were explored by PL spectroscopy. PL spectroscopy is a contactless, non-destructive technique of probing electronic structure of materials. The absence of luminescence in bulk MoS_2 and strong emerging photoluminescence in exfoliated MoS_2 is an indicative of the transition from indirect to direct band gap [34]. For

the synthesis of strong photoluminescence MoS_2 QDs, the exfoliation of bulk MoS_2 to monolayer is a pre-requisite and important step.

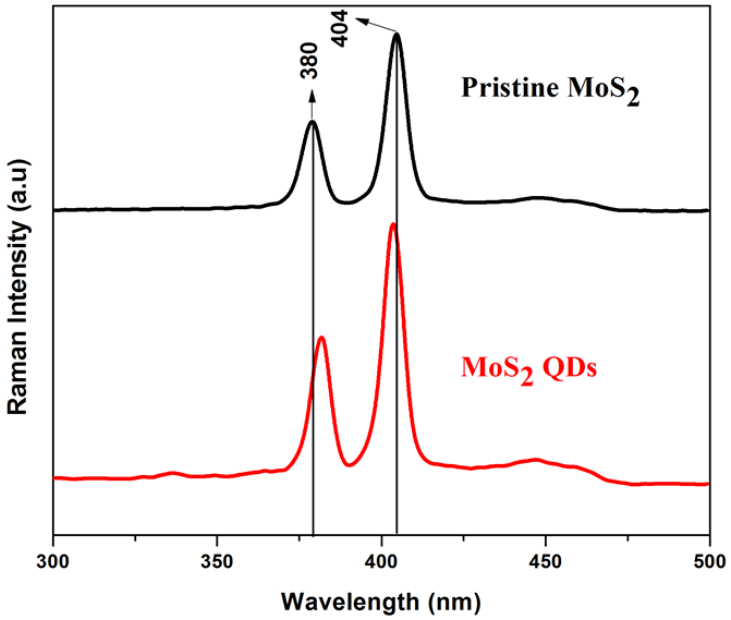

Fig. 2.3. Raman spectra of pristine MoS_2 depicting two phonon modes E^1_{2g} at 380 cm^{-1} and A_{1g} at 404 cm^{-1} respectively, while MoS_2 QDs show red shift of E^1_{2g} mode at 382 cm^{-1} and blue shift of A_{1g} mode at 402 cm^{-1}.

When the size of the exfoliated mono layer MoS_2 is less than 100 nm, it leads to the confinement and edge effects which causes the photoluminescence emission [38]. Due to the transition from indirect to direct band gap MoS_2 nanostructures show unique photoluminescence properties. Fig. 2.4 (a) exhibits that as synthesized MoS_2 QDs emitted a distinct blue PL at 448 nm regardless of the excitation wavelength when they were excited at various excitation wavelengths ranging from 260 nm to 350 nm which shows high homogeneity. This range also confirms that size of MoS_2 QDs synthesized by this approach is very small because luminescence properties of QDs are dependent upon their size [38]. The as synthesized MoS_2 QDs showed a distinct blue luminescence (Inset of Fig. 2.4 a) when illuminated under 365 nm UV illumination.

Optical properties were further investigated by UV-Vis spectroscopy. Two absorption band were observed at 290 nm (4.26 eV) and at 362 nm (3.42 eV) respectively as shown in Fig. 2.4 (b). These two absorption bands corresponded to the small size of MoS_2 QDs most of which

are 3.5 nm in size (as shown in Fig. 2.2 b) and are in well agreement with previously reported absorption spectra of MoS_2 nanoclusters [43].

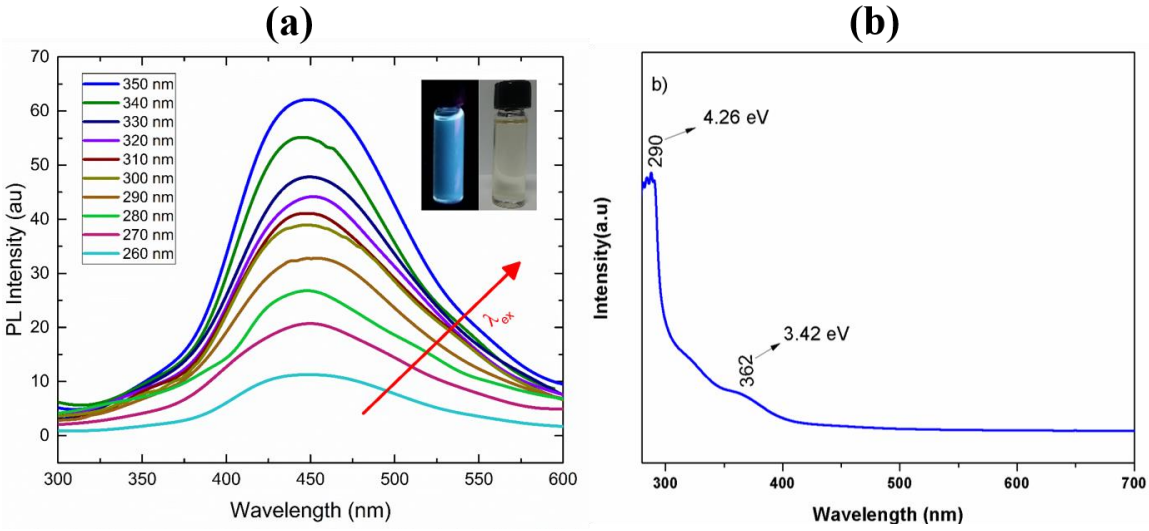

Fig. 2.4. (a) PL spectra of MoS_2 QDs showing a distinct blue PL at 448 nm recorded at various excitation wavelengths ranging from 260 to 350 nm. Inset: digital images of as prepared MoS_2 QDs solution (right) and blue photo luminescent MoS_2 QDs solution upon the UV illumination at 365 nm. (b) UV-Vis absorption spectrum showing two bands at 290 nm and 362 nm.

Chemical and elemental composition were analysed by FTIR spectroscopy and energy dispersive X-ray (EDX) spectroscopy shown in Fig. 2.5 (a) and 5 (b) respectively. In Fig. 2.5 (a), a very weak absorption peak can be observed at 467 cm^{-1} which is attributed to the Mo−S stretching vibration mode of MoS_2. FTIR spectra of the exfoliated MoS_2 remain same as of bulk MoS_2 [42]. EDX analysis was also applied to determine the elemental composition of as synthesized MoS_2 QDs which confirms the presence of Mo and S as shown in Fig. 2.5(b). The peaks indicate that sample contains Mo, S and Cu. The highest peak recorded belongs to Cu grid support for measurement. The atomic ratio of S to Mo was calculated about 2.12 which is quite close to the theoretical value of MoS_2. These values confirm that the products were stoichiometric MoS_2.

The crystal structure of as synthesized MoS_2 QDs was investigated using XRD system. The reflection peaks can be assigned to the family lattice planes of hexagonal MoS_2 (JCPDS card no.77-1716). In Fig. 2.6, XRD spectra of MoS_2 QDs is compared with the pristine MoS_2.

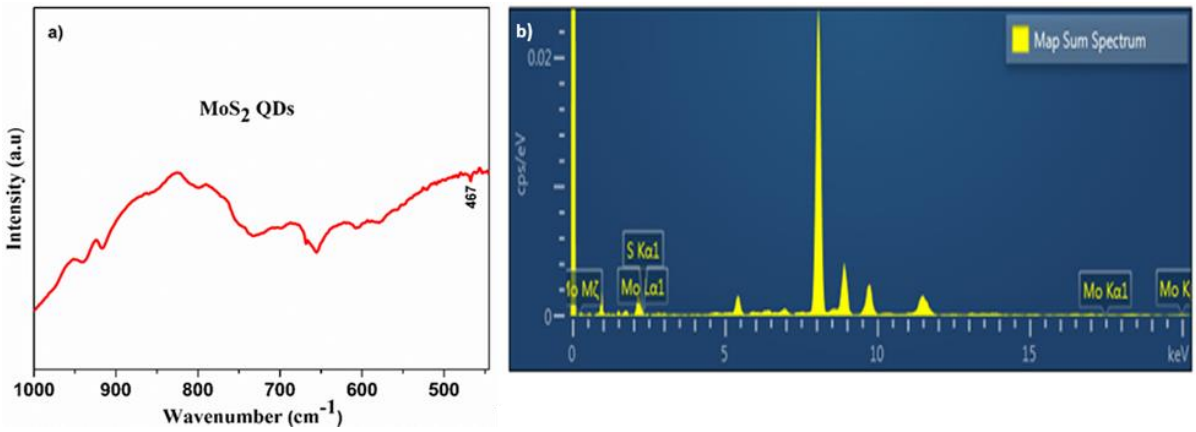

Fig. 2.5. (a) FTIR spectra of MoS_2 QDs showing a very weak absorption peak at 467 cm^{-1} which is attributed to the Mo−S stretching vibration mode of MoS_2. (b) Energy dispersive X-ray spectrum confirming the elemental composition of MoS_2 QDs.

Three dominant peaks can be observed at 14.2° (002), 39.5° (103) and 49.8° (105) respectively in pristine sample whereas only one weak peak is obtained in case of MoS_2 QDs that is attributed to (002) plane and occupies the similar position to pristine MoS_2 which means no other new phases are introduced into MoS_2 QDs. So it can be concluded from XRD data that pristine MoS_2 and MoS_2 QDs both are identified as 2H MoS_2 with prominent peak at 14.2° belonging to (002) plane.

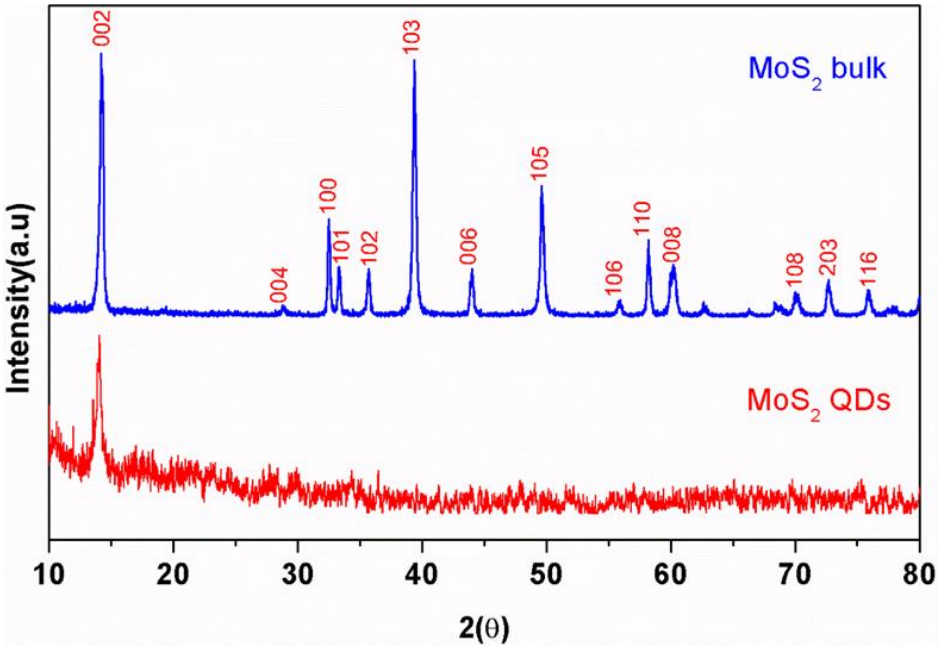

Fig. 2.6. XRD spectra of MoS_2 bulk and MoS_2 QDs, common peak for both phases of MoS_2 is observed at a value of 2θ of 14.2° which corresponds to (002) plane.

2.2. Hydrothermal growth of ZnO nanowires

For vertically aligned, highly dense and uniform growth of ZnO NWs, the deposition of ZnO seed layer is considered prerequisite so first, for deposition of ZnO seed layer, 20 mM $Zn(CH_3COO)_2.2H_2O$ solution was prepared by dissolving it in anhydrous ethanol. ZnO seed layer was deposited on top of as fabricated bottom electrode patterns on PET by reverse offset. ZnO seed layer solution was spin coated in such a way that after depositing one layer, PET was annealed at 95 ˚C for 10 min and this process was repeated 5 times and finally annealed at 95 ˚C for 3 hours. The all process was repeated once again to get a distinct white layer to ensure the better growth of ZnO seed layer.

ZnO NWs were grown by hydrothermal synthesis using equimolar (40 mM) aqueous solutions of $Zn(NO_3)_2.6H_2O$ and HMTA in deionized water. The PET substrate printed with bottom electrodes and ZnO seed layer over it was immersed in the aqueous solution upside down in an autoclave and heated at 95 ˚C for 3 hours. Finally, after heating the PET substrate was taken out and washed with deionized water several times to remove surface contaminations and dried in an open air.

The growth of the ZnO nanowires may take place through the following chemical reactions:

$$(CH_2)_6N_4 + 6H_2O \rightarrow 6HCHO + 4NH_3 \quad (1)$$

$$NH_3 + H_2O \rightarrow NH_4^+ + OH^- \quad (2)$$

$$Zn^{2+} + 2OH^- \rightarrow Zn(OH)_2 \quad (3)$$

$$Zn(OH)_2 \rightarrow ZnO + H_2O \quad (4)$$

2.2.1 Material Characterization

Morphology of the deposited ZnO seed layer and as grown ZnO NWs on ZnO seed layer has been analyzed by FESEM images as shown in Fig. 2.7. ZnO NWs grown by hydrothermal

synthesis were found to be highly dense, aligned and vertically oriented with hexagonal crystal structure as shown in Fig. 2.7 (b) & (c). Their size was also observed very uniform, average diameter was found to be 100 nm, average length (0.5 µm), and average density ($1\times2\ 10^{9}$ cm^{-2}). In fact, the growth of such highly aligned and dense ZnO NWs is related to the quality of the ZnO seed layer; unsmoothed, defected ZnO seeding layer results in the non-vertical and random distribution of ZnO NWs. Fig. 2.7 (a) shows the FESEM image of the compact ZnO seed layer proving that the surface morphologies of these hydrothermally grown ZnO NWs strongly depend upon the ZnO seeding layer.

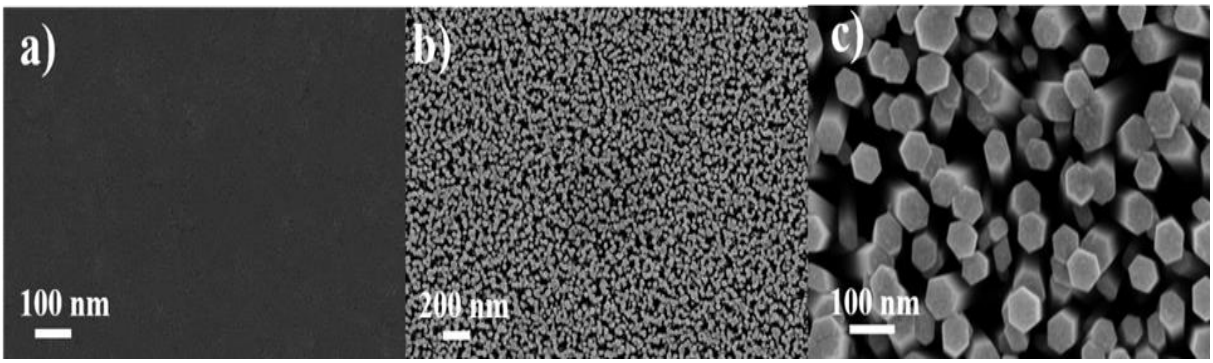

Fig. 2.7. (a) SEM image of ZnO seed layer (b) Highly dense and vertically aligned ZnO NWs grown over the ZnO seed layer (c) SEM image on higher resolution showing truly hexagonal shape of ZnO NWs.

X-Ray diffraction patterns of ZnO nanowires, has been shown in Fig. 2.8. The patterns clearly reveal the diffraction peaks at 31.61, 34.49, 36.27, 56.32 and 62.63 corresponding to (100), (002), (101), (110) and (103) planes that can be indexed to hexagonal wurtzite crystal structure of ZnO NWs.[44] These diffraction peaks indicating the purity of ZnO NWs due to absence of other peaks related to impurities and are in well agreement with JCPDS card no. 36-1451 with cell constants of a = 3.25 Å and c = 5.19 Å. The dominant diffraction peak at 2θ = 34.49 corresponding to the (002) plane indicates high degree of anisotropic growth of ZnO NWs along *c*-axis perpendicular to the PET substrate and highly crystalline in nature.

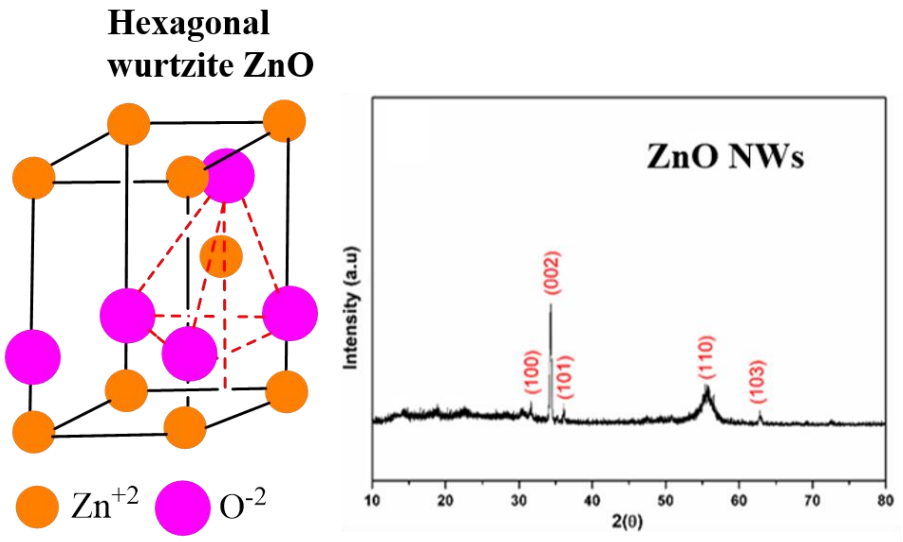

Fig. 2.8. Crystal structure of hexagonal wurtzite ZnO, and X-ray diffraction patterns of as synthesized ZnO NWs grown on PET substrate showing high crystallinity.

2.3. Liquid based exfoliation of 2D materials

Liquid exfoliation of layered or 2D materials has certain advantages as it is solution processable, easy to make inks and composite and ease of fabrication of thin film on various substrate from rigid to flexible substrates.

2.3.1 Exfoliation of MoS_2 and characterization

MoS_2 nanoflakes ink was prepared by exfoliating the MoS_2 multi flakes by aqueous exfoliation method. MoS_2 pristine powder was ground in ethanol for 1 hour in a mortar followed by heating at 100 ℃ for 1 hour to evaporate the solvent. Furthermore, ground MoS_2 was dispersed in 50/50 % solution of ethanol and deionized water for probe sonication for 1 hour as grinding and sonication both are effective in exfoliation of MoS_2 flakes. Finally, centrifugation at 4000 rpm was carried out for 30 min to remove the larger flakes and partially exfoliated crystallites. The supernatant was collected and placed on magnetic stirrer for overnight.

Morphology of the as exfoliated MoS_2 flakes by aqueous exfoliation has been shown in Fig. 2.9 (a). It cab seen that MoS_2 flakes of various size from several nanometer to few micrometer have been obtained through aqueous exfoliation assisted grinding and sonication method. Fig.

2.9 (b) shows the morphology of as deposited thin film of MoS_2 flakes through EHDA, a uniform film of MoS_2 flakes of various size and it can be seen that MoS_2 exfoliated flakes are dispersed uniformly on PET surface.

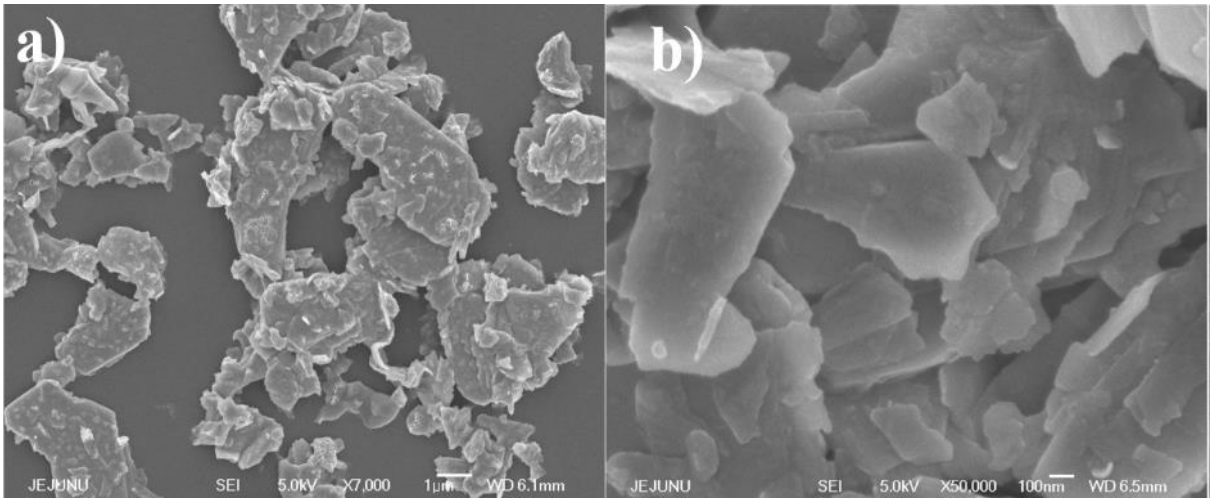

Fig. 2.9. Morphology of the materials used in the humidity sensor (a) FESEM image of the as exfoliated MoS_2 flakes by aqueous exfoliation (b) FESEM images of MoS_2 flakes thin film deposited by EHDA showing the large lateral size flakes are uniformly dispersed on PET surface.

2.3.2 Exfoliation of h-BN and characterization

Exfoliation of bulk BN flakes was conducted on liquid based method to make a stable solution. First of all the wet grinding was carried out of pristine BN in a mortar by adding few drops of IPA for 2 hours and after drying the wet mixture it was dispersed in IPA. This dispersion was sonicated in an ultrasonic bath sonicator for 1 hour followed by ultrasonic probe sonication for 1 hour at high frequency. Further to separate the bulk or large unexfoliated flakes, the as prepared dispersion was centrifuged at 4000 rpm for 30 min and top 3/4 supernatant was taken out in a vial.

The surface morphology, topography and orientation of the as exfoliated hBN nanosheets was investigated using FESEM. Fig. 2.10 (a) shows the microstructure and lateral size of as exfoliated hBN nanoflakes. The AFM image has been shown in Fig. 2.10 (b) which shows the thickness of a single exfoliated hBN nanoflake up to 3 nm along the red line and its

corresponding height profile. This AFM data exhibits that the liquid based exfoliation has also potential for producing thin nanosheets of 2D materials as these very thin nanosheets are useful for resistive switching effect.

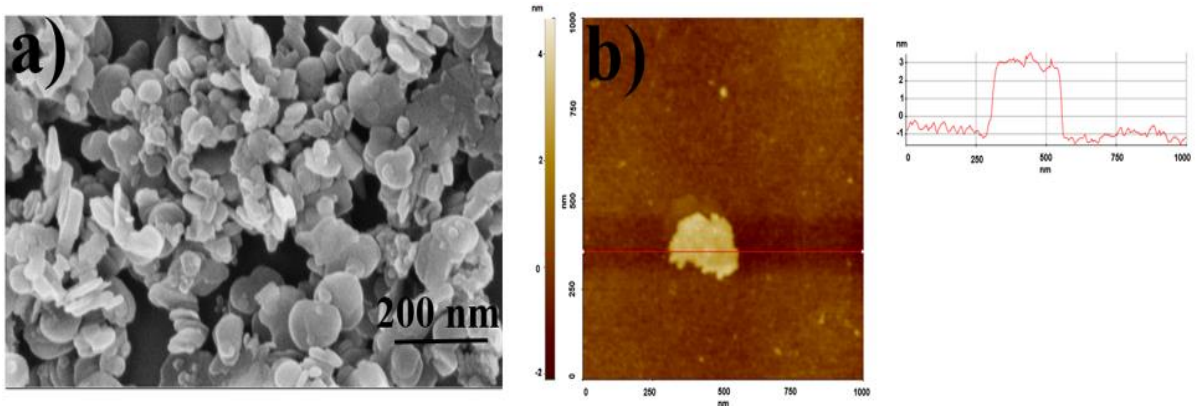

Fig. 2.10. Morphology of the as exfoliated hBN nanosheets by liquid exfoliation method and its nanocomposite; (a) showing the FESEM image of the as exfoliated hBN nanoflakes. (b) AFM image of a single nanoflake after exfoliation showing the thickness up to 3 nm.

Raman spectroscopy was used to investigate the exfoliation of BN 2D flakes. Fig. 2.11 shows the Raman spectra of both bulk and exfoliated BN flakes. The E_{2g} vibrational mode is observed in unexfoliated or pristine and exfoliated hBN which is the characteristic of hBN structure. In pristine hBN the E_{2g} mode is observed at 1367 cm^{-1} while in exfoliated hBN it is observed at 1370 cm^{-1} [45,46]. So, there is a blue shift of the E_{2g} vibrational mode up to 3 cm^{-1} in exfoliated hBN which is quite comparable with the earlier reported results[46,47].

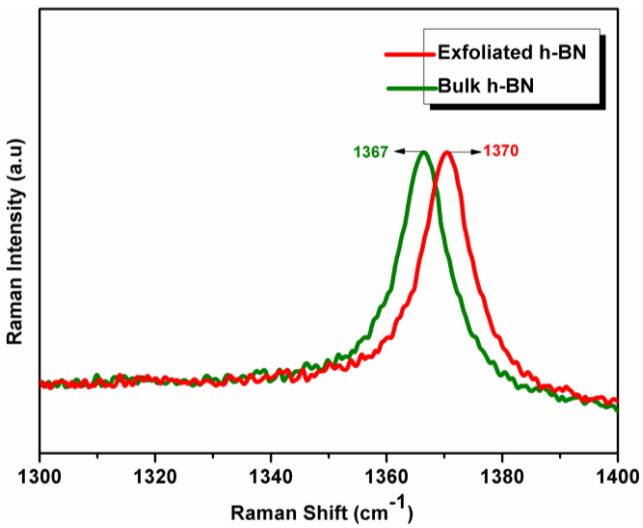

Fig. 2. 11. Raman spectra of as exfoliated hBN nanosheets showing E_{2g} vibrational mode of bulk and exfoliated phases at 1367 cm^{-1} and 1370 cm^{-1} respectively.

2.4. Synthesis of $ZnSnO_3$ Nanocubes

Synthesis of crystalline $ZnSnO_3$ nanocubes was carried out via aqueous solution method; 100 mmoles of $ZnSO_4.7H_2O$ were added in 100 ml of deionized (DI) water and stirred at room temperature until the complete dissolution of $ZnSO_4.7H_2O$. Then 100 mmol of $Na_2SnO_3.3H_2O$ were added into the preliminary solution and was kept on magnetic stirrer at 80 ˚C for 5 h. A white suspension of an intermediate product $ZnSn(OH)_6$ was formed which precipitates were collected from the solution by vacuum filtration and were washed with DI water several times to remove residual products and were then dried in air at 100 ˚C for 1 h. Afterwards, the as synthesized $ZnSn(OH)_6$ powder was calcinated at 600 ˚C for 3 h. Finally, we got the $ZnSnO_3$ nanocubes by the following possible reaction:

$$Zn^{2+} + 2OH^- \rightarrow Zn(OH)_2 \quad (5)$$

$$Zn(OH)_2 + SnO_3^{2-} + 3H_2O \rightarrow ZnSn(OH)_6 + 2OH^- \quad (6)$$

$$ZnSn(OH)_6 \rightarrow ZnSnO_3 + 3H_2O \quad (7)$$

2.4.1 Material Characterization

$ZnSnO_3$ nanocubes was investigated by FE-SEM as shown in Fig. 2.12 (a,b). It reveals clearly the cubic shape of $ZnSnO_3$ nanostructures having an average size of approximately 70 nm and also showing the large-scale, uniform cubic crystallites yielded with this approach.

An intermediate product zinc hydroxystannate ($ZnSn(OH)_6$) is formed before the yield of $ZnSnO_3$ nanocubes. They were obtained by carrying out the chemical reaction between $ZnSO_4.7H_2O$ and $Na_2SnO_3.3H_2O$ at 80˚C for 5 h which on further calcination at 600 ˚C for 3 hours converted to the desired product, i.e. $ZnSnO_3$ nanocubes. Fig. 2.13 (a) shows the XRD patterns of the $ZnSn(OH)_6$ material obtained at 80 ˚C . All the diffraction peaks are in good agreement with the values reported previously [48].

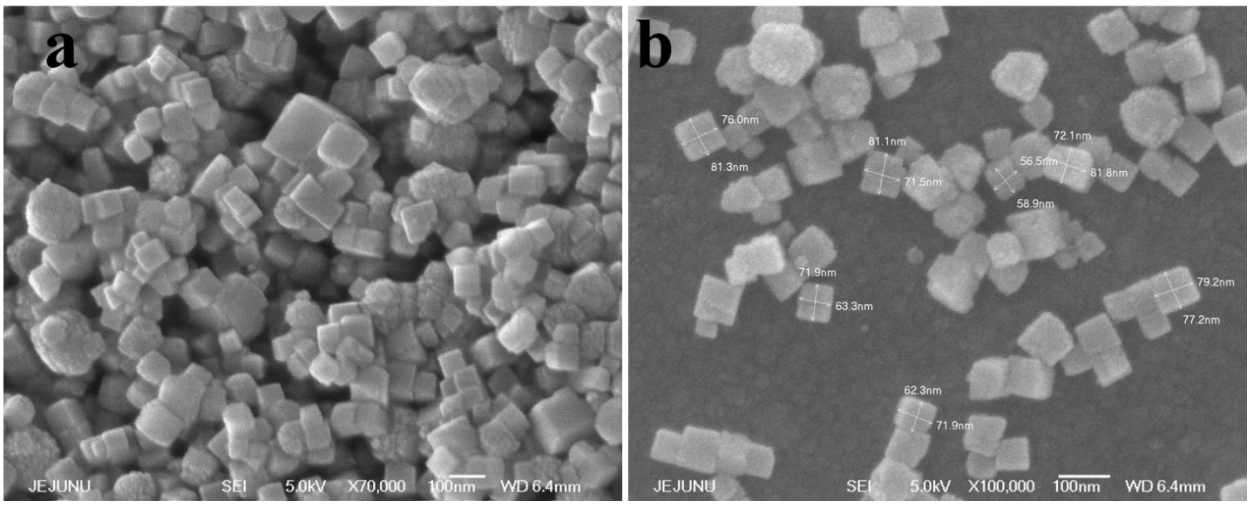

Fig. 2.12. (a,b) FESEM images showing cubic shape and uniform size of as synthesized ZnSnO3 NCs via an aqueous solution method.

The crystalline structure of $ZnSnO_3$ nanocubes is confirmed by XRD as shown in Fig. 2.13 (b), all of the indicating diffraction peaks can be indexed to the JCPDS card No. 28-1486. The XRD spectrum also indicates that $ZnSnO_3$ nanocubes have pure crystalline structure and there are no impure phases in it. So, overall it shows a large surface area, high crystallinity, smaller particle size and uniform morphology.

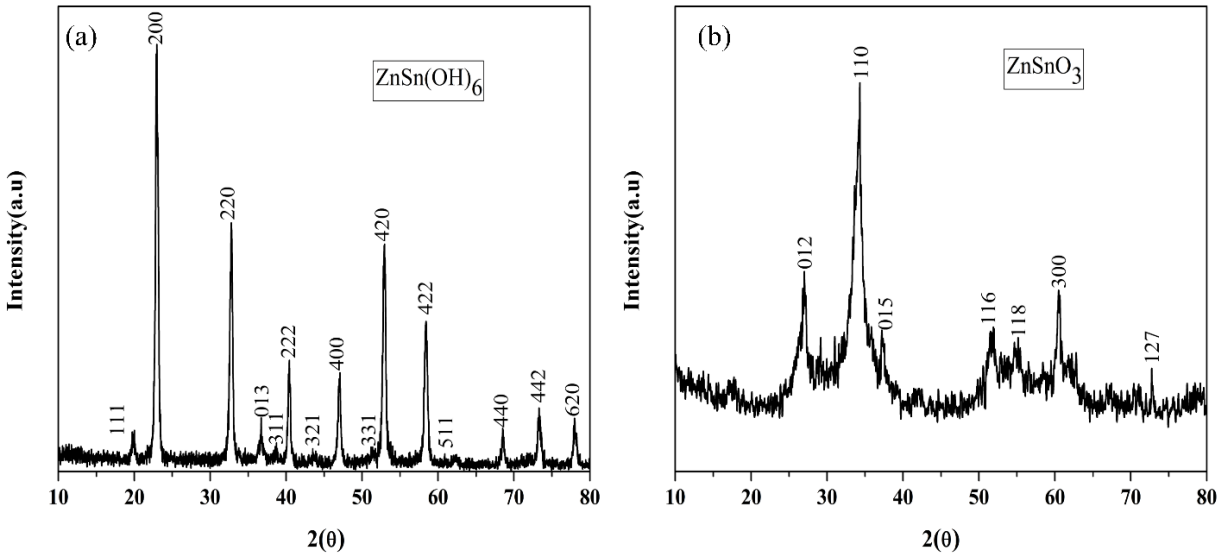

Fig. 2.13. (a) XRD patterns of $ZnSn(OH)_6$ synthesized via an aqueous solution method at 80 ˚C. (b) XRD patterns of $ZnSnO_3$ nanocubes obtained after the calcination at 600 ˚C.

To investigate the composition of $ZnSn(OH)_6$ and $ZnSnO_3$, Raman and FTIR spectra were obtained and obtained values of both spectra resemble well with the values reported in literature

[49,26]. Fig. 2.14 (a) represents the Raman spectra of both materials $ZnSn(OH)_6$ and $ZnSnO_3$ in which four Raman modes can be seen at 299, 372, 436 and 608 cm^{-1} for $ZnSn(OH)_6$ arising from the breathing vibrations of the long M–OH bonds and M–OH–M (bridging OH group) bending modes. After heating the $ZnSn(OH)_6$ at 600 ˚C for 3 hours the above mentioned four Raman modes were slightly shifted to two new Raman modes at 538 and 671 cm^{-1}. The broad peak at 671 cm^{-1} corresponds to the distinctive Raman shift of $ZnSnO_3$ and is imputed to stretching vibrations of short M–O bonds in the MO_6 octahedron that protrude into the structure spaces. The peak at 538 cm^{-1} is assorted with internal vibrations of the oxygen tetrahedron.

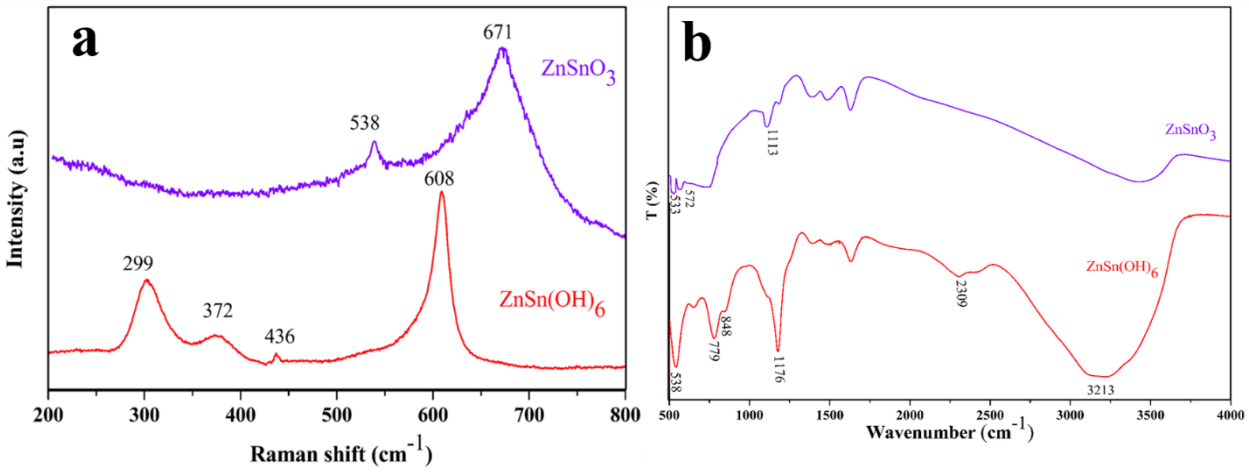

Fig. 2.14. (a) Raman spectra of $ZnSn(OH)_6$ and $ZnSnO_3$ nanocubes showing shifting of four Raman modes to two new Raman modes after calcination at 600 ˚C for 3 h. FTIR spectra of $ZnSn(OH)_6$ and $ZnSnO_3$ nanocubes exhibiting the conversion of $ZnSn(OH)_6$ to $ZnSnO_3$.

The FTIR spectra of both $ZnSn(OH)_6$ and $ZnSnO_3$ are shown in Fig. 2.14 (b). The bands at ~3213cm^{-1} is ascribed to the bending and stretching vibration modes of hydroxyl (–OH) group in the structure of $ZnSn(OH)_6$. The bands at 779, 848, 1176, and ~2309 cm^{-1} may be attributed to vibration of M–O or M–OH–M groups for $ZnSn(OH)_6$ while the bands at 533, 572, and 1113 cm^{-1} are assigned to vibrations of M–O or M–O–M groups for $ZnSnO_3$. It was observed from the spectral data that, after calcination the peaks of the (–OH) group almost disappeared while the peaks attributed to the M–O bond became prominent which testified the conversion of $ZnSn(OH)_6$ into $ZnSnO_3$.

2.5. Nanocomposite of $ZnSnO_3$/PMMA

The $ZnSnO_3$ nanocubes were synthesized by aqueous solution method as described in detail in section 2.4. The PMMA solution was prepared by dissolving 0.10 g of PMMA in 10 ml of toluene and kept on bath sonicator for 5 min and then kept for stirring at 40 ˚C for 24 hours. The as synthesized $ZnSO_3$ nanocubes were then dispersed in PMMA solution. For the better dispersion of $ZnSnO_3$ nanocubes into PMMA solution, it was sonicated for 30 min and a non-ionic surfactant, i.e. 0.01% Triton X-100 (Sigma Aldrich) was also added for the same purpose and kept on stirrer at room temperature for overnight to check the stability of the synthesized ink. To improve the quality of the film and to meet the conductivity requirements for electrospray deposition, the co-solvent approach was adopted [50,51] and dimethyl sulfoxide (DMSO) was added to $ZnSnO_3$/PMMA ink in a ratio of 1:5.

2.5.1 Characterization of $ZnSnO_3$/PMMA nanocomposite thin film

FE-SEM image of $ZnSnO_3$/PMMA thin film has been presented in Fig. 2.15 (a,b) showing that the film surface is mainly covered by the PMMA and $ZnSnO_3$ nanocubes are buried PMMA. Moreover, the film is highly uniform and compact and has the potential to be used in various electronic devices.

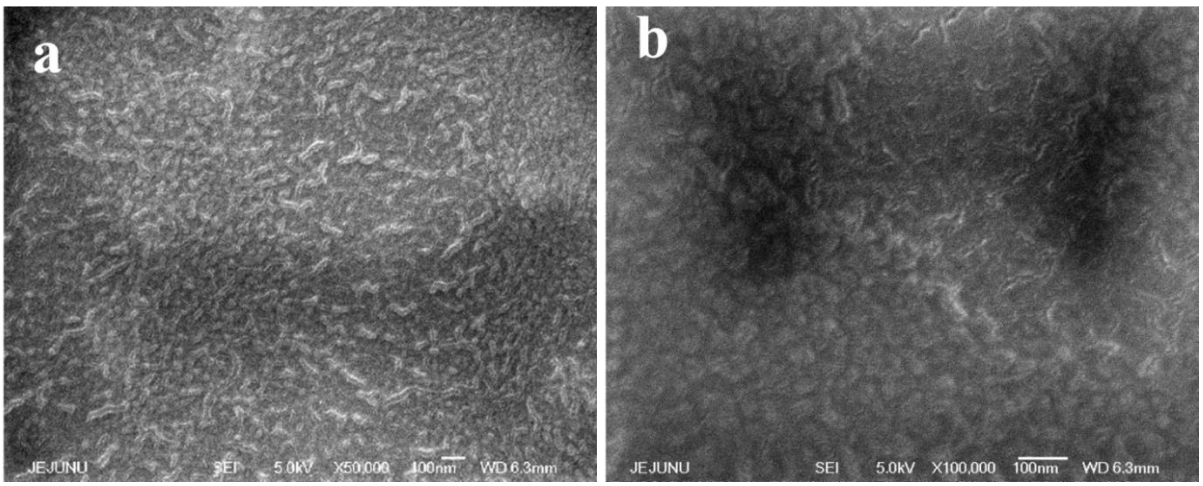

Fig. 2.15. (a,b) FESEM images of the as deposited ZnSnO3/PMMA nanocomposite thin film through EHDA showing that ZnSnO2 NCs are fully covered by the blanket of polymer i.e. PMMA and film is uniform and smooth.

The FTIR spectra of $ZnSnO_3$-PMMA nanocomposite thin film is shown in Fig. 2.16 (a) in which both $ZnSnO_3$ and PMMA peaks are present, but most of the peaks belong to PMMA and agree well with the values of the FTIR spectra of PMMA reported in the literature [52,53]. The peaks at 538 and 617 cm^{-1} are attributed to the vibrations of M–O or M–O–M groups for $ZnSnO_3$. The peaks at 696 and 750 cm^{-1} are assigned to out of plane OH bending. The band at 987 cm^{-1} is the characteristic absorption of PMMA, together with the band at 1067 cm^{-1}. The peak observed at 1151cm^{-1} is assigned to C–O stretching, whereas the peak observed at 1452 cm^{-1} is assigned to O–CH_3 bending and at 1733 cm^{-1} is attributed to C=O stretching which shows the presence of the acrylate carboxyl group. The two peaks at 3446 and 1541 cm^{-1} can be attributed to the –OH group stretching and bending vibrations of physisorbed moisture [54].

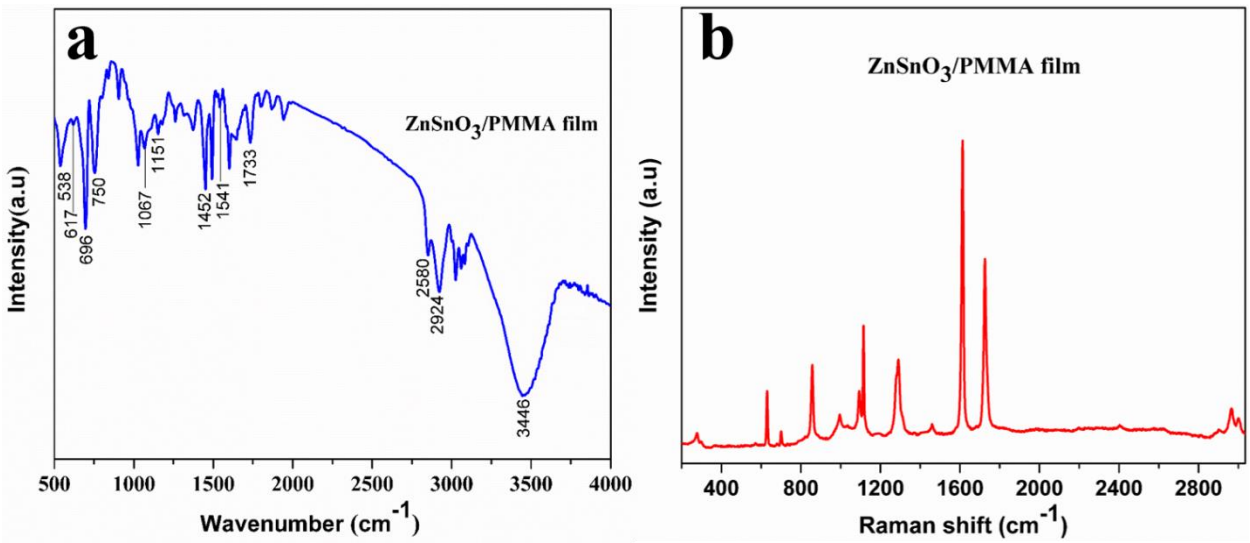

Fig. 2.16. (a) FTIR spectra of $ZnSnO_3$/PMMA composite film on PET showing two peaks 538 and 617 cm-1 from $ZnSnO_3$ and others are from PMMA. (b) Raman spectra of $ZnSnO_3$/PMMA composite film showing only one Raman active mode at 279 cm-1 from ZnSnO3 while others belong to PMMA.

Raman scattering of $ZnSnO_3$/PMMA composite film has been shown in Fig. 2.16 (b) that exhibits only one Raman active mode at 279 cm-1 from ZnSnO3 while other Raman modes noticed in the spectra are from PMMA [55,56].

Transmittance and absorbance of as deposited $ZnSnO_3$/PMMA film on PET was carried out by using UV-VIS-NIR spectrophotometer as shown in Fig. 2.17 (a). It shows the high

transmittance and low absorbance of the deposited film of $ZnSnO_3$/PMMA on PET. It shows an average transmittance of 92%, which indicates that it can be very useful in transparent electronics.

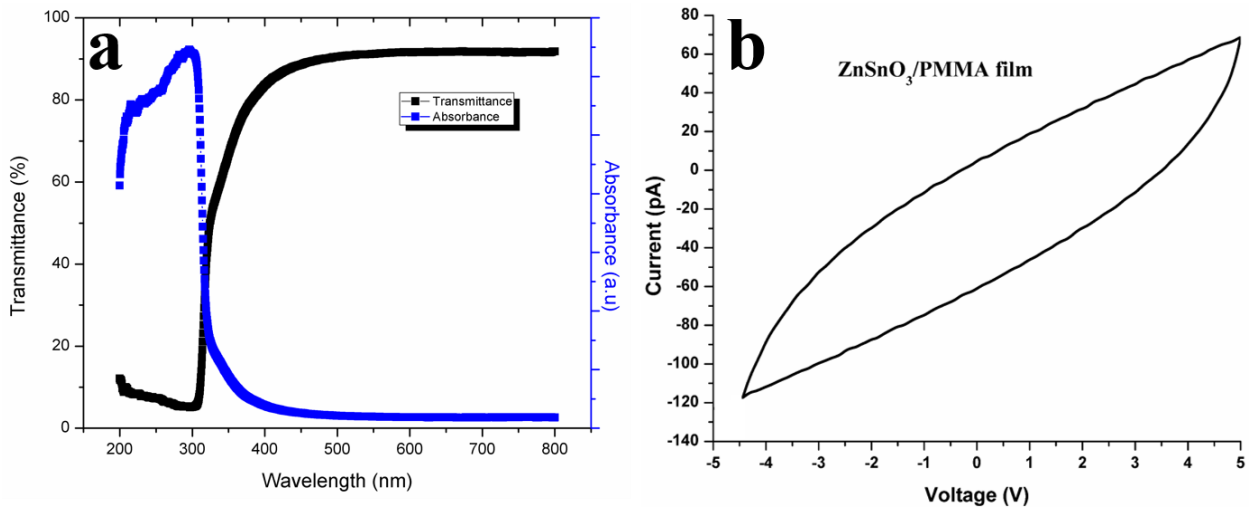

Fig. 2.17. (a) Transmittance and absorbance spectrums of $ZnSnO_3$/PMMA deposited film on PET by ESD. (b) I–V characteristic curve exhibiting the dielectric behavior of $ZnSnO_3$/PMMA composite film on PET with non-linear behavior and low magnitude of current.

Electrical properties of $ZnSnO_3$/PMMA film were measured by semiconductor device analyzer by placing the probes of device on silver contacts deposited on the $ZnSnO_3$/PMMA film so that they may not damage the film. The *I-V* plot for an approximately 110 nm thick $ZnSnO_3$/PMMA film is shown in Fig. 2.17 (b). The *I-V* plot shows very low currents and high resistance at low applied potentials. The resistivity was measured from the slopes of the linear *I-V* plot and using the sheet resistivity formula for thin films:

$$\rho = \frac{\pi t}{\ln 2}\left(\frac{V}{I}\right)$$

Where '*t*' is the thickness of the film (110 nm), while '*V*' is voltage and '*I*' is the current from the *I-V* plot. The calculated resistivity came out to be $\approx 34.88 \times 10^3$ Ω.m. As a passive component we can include the use of this material as dielectric for a wide range of electronic devices.

2.6. Nanocomposite of $ZnSnO_3$/Polyvinyl alcohol (PVOH)

The $ZnSnO_3$ nanocubes were synthesized by aqueous solution method as described in detail section 2.4. The nanocomposite ink of PVOH-$ZnSnO_3$ was prepared in NMP solvent, first 10 wt.% PVOH was dissolved in NMP followed by bath sonication for 10 min in an ultrasonic bath sonicator. The resulting solution was stirred on a magnetic stirrer at 70 ˚C until all the PVOH polymer was completely dissolved in NMP. $ZnSnO_3$ nanocubes (1 wt.%) were dispersed in the PVOH solution and sonicated in an ultrasonic probe sonicator to enhance homogeneity. The final solution was stirred on a magnetic stirrer to check the stability of the ink for overnight at room temperature. The formation of the granular polymer network by mixing the inorganic perovskite $ZnSnO_3$ nanocubes and PVOH has been illustrated in Fig. 2.18.

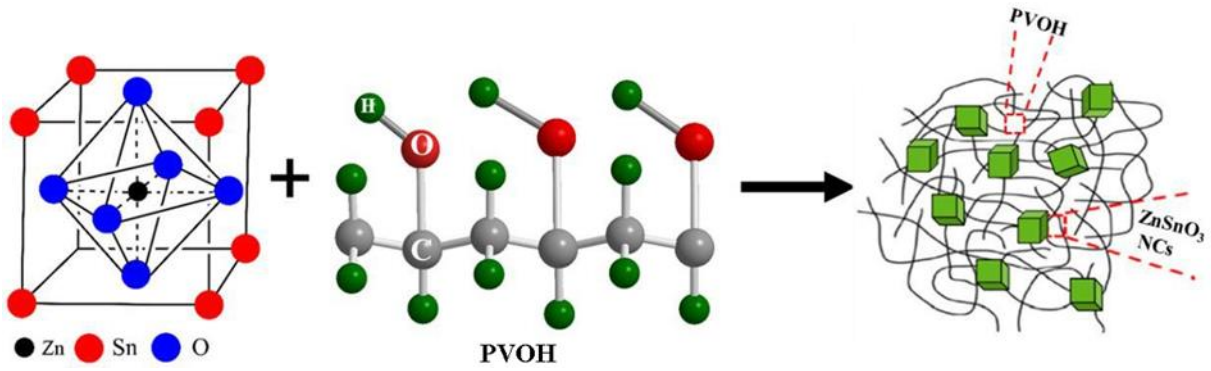

Fig. 2.18. Structural formulas of inorganic perovskite oxide and organic polymer showing interatomic chemical bonds and resulting hybrid nanocomposite solution.

2.6.1 Characterization of thin film of $ZnSnO_3$/PVOH

X-ray diffraction (XRD) is a powerful technique to understand the various characteristics of thin films including determination of crystalline structure and phase analysis. The XRD pattern of PVOH-$ZnSnO_3$ composite thin film has been shown in Fig. 2.19 (a). The large and broad diffraction peak located at $2\theta = 19.04^{\circ}$ corresponds to (101) plane and exhibited the semi-crystalline nature of PVOH [57]. The small hump like pattern located at $2\theta = 39.24^{\circ}$ depicted the presence of $ZnSnO_3$ nanocubes. As the concentration of $ZnSnO_3$ is low compared to PVOH in this nanocomposite so the peak at this point is not prominent. This XRD spectra confirmed

that the prepared thin film of PVOH-$ZnSnO_3$ nanocomposite consists of only two phases i.e. PVOH and $ZnSnO_3$ and ruled out the presence of other phases or impurities.

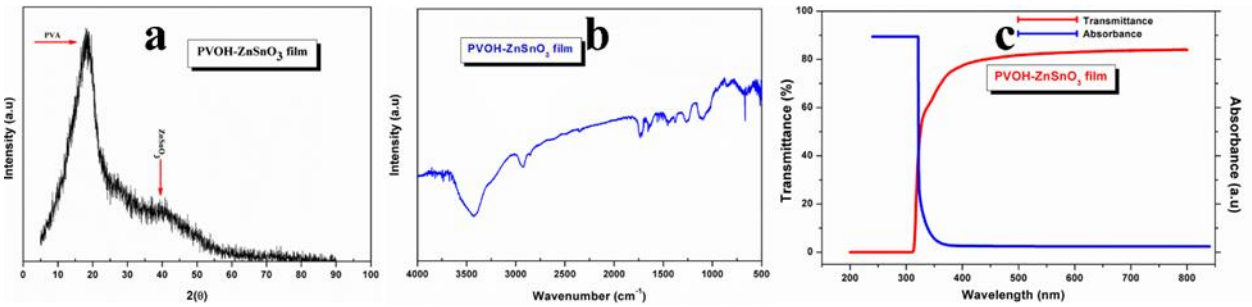

Fig. 2. 19. Structural and optical characterization plots of as synthesized organic-inorganic hybrid nanocomposite (a) XRD spectra (b) Raman spectra (c) UV-vis transmittance and absorbance spectra.

Optical characterization of Fourier Transform Infrared (FTIR) spectroscopy was carried out for determining the chemical composition and interatomic bonding of PVOH-$ZnSnO_3$ hybrid thin film in the IR region of the electromagnetic spectrum as shown Fig. 2.19 (b). The broad peak at 3422 cm^{-1} is assigned to the hydrogen-bonded O-H stretching due to the absorption of moisture. The peak at 2921 cm^{-1} is attributed to the asymmetric stretching vibration of CH_2 group. The two bands at 1739 cm^{-1} and 1653 cm^{-1} correspond to the C=O stretching vibrations in the acetate group and C=C stretching mode of PVOH respectively. The band appeared at 1455 cm^{-1} is attributed to the bending deformation of CH_2 vibrations. The out-of-plane O-H bending vibration and in-plane O-H bending vibration are observed at 1375 cm^{-1} and 668 cm^{-1} respectively. The other two bands observed at 1266 cm^{-1} and 1094 cm^{-1} correspond to the O-C stretching vibrations. Most of the peaks described in the FTIR spectra are related to the PVOH polymer and well matched with the earlier reported nanocomposite thin films of PVOH [57,58]. The single peak at 516 cm^{-1} is assigned to the presence of $ZnSnO_3$ in this nanocomposite thin film [59]. Thus FTIR spectra revealed the formation of PVOH and $ZnSnO_3$ nanocomposite with no other impurities and also proved the effective infiltration of $ZnSnO_3$ nanocubes into the polymer matrix of PVOH.

The UV-vis transmittance and absorbance spectra of PVOH-$ZnSnO_3$ nanocomposite thin film were also recorded by using UV/vis spectroscopy technique. Both transmittance and

absorbance spectra are merged in Fig. 2.19 (c). The PVOH film is highly transparent (~ 90% transmittance across the visible light region) making it extremely useful in various optical applications as reported by Wang et al [60]. In this work; by the addition of $ZnSnO_3$ nanocubes into the polymer matrix of PVOH for the formation of granular polymer network, the transparency has not affected much and found to be ~ 84%.

Fig. 2.20 (a) illustrates the surface morphology of the nanocomposite thin film as deposited by EHDA which exhibited the formation of granular polymeric network. Furthermore, SEM images also revealed that $ZnSnO_3$ nanocubes are homogeneously embedded into the polymer matrix of PVOH resulting in the formation of granular polymer network. The thickness of thin film was measured by cross-sectional FESEM image as shown in Fig. 2.20 (b) and it appeared to be ≈ 238 nm.

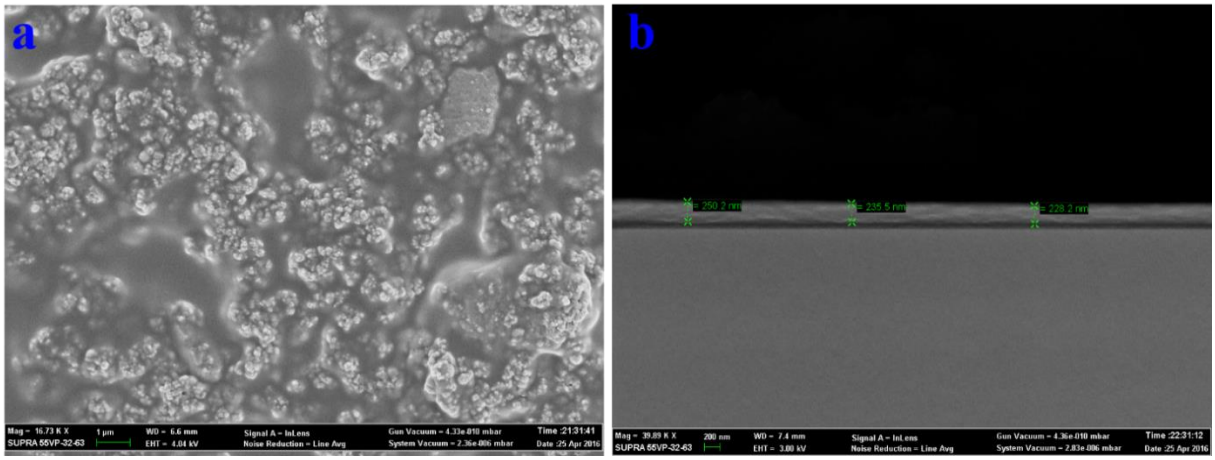

Fig. 2. 20. (a) Surface morphology of PVOH-$ZnSnO_3$ hybrid nanocomposite thin film exhibiting formation of granular polymeric network (b) Cross-section FESEM image illustrating the average thickness of as deposited thin film by EHDA.

2.7. Nanocomposite of hBN/PVOH

Exfoliated of bulk hBN flakes has been described in detail in section 2.3.2. The polymer ink was prepared by dissolving PVOH powder in DI water at 80 ˚C and placed on magnetic stirrer until a transparent solution is formed on complete dissolution of powder. Both, the as prepared hBN solution in IPA and PVOH solution in DI water were homogenously mixed in equal volumes and stirred at high rpm by placing it on magnetic stirrer for overnight to check the

stability of the mixed solution. The schematic of the hBN/PVOH nanocomposite has been shown in Fig. 2.21 in which the structures of hBN and PVOH are exhibited on reactant side and crosslinked nanocomposite of exfoliated hBN nanosheets with polymer chain on the product side. Structure of PVOH shows that it is a branched polymer, significantly suitable for coating a 2D material to form a highly uniform thin film.

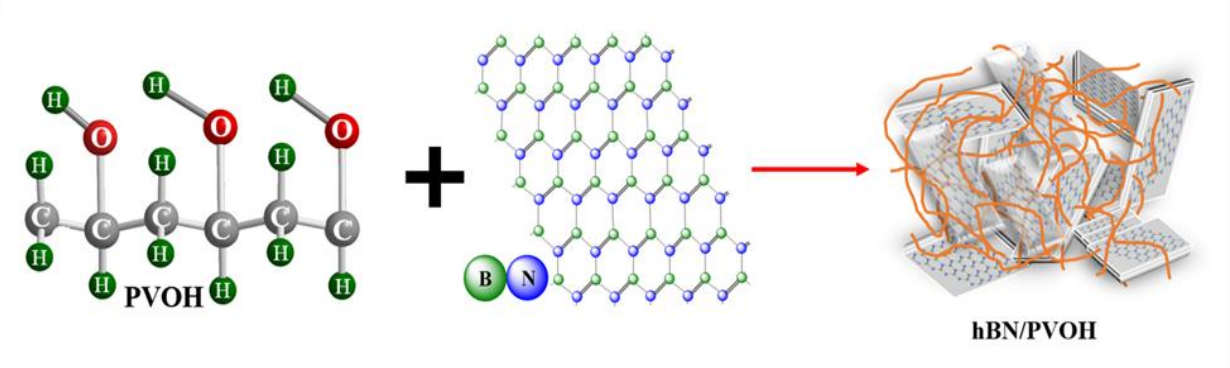

Fig. 2.21. Schematic representation of the structures of hBN and PVOH on reactant side and nanocomposite on product side.

2.7.1 Characterization of thin film of hBN/PVOH nanocomposite

The surface morphology and topography of hBN/PVOH nanocomposite was investigated using FESEM. The morphology of the thin film of hBN/PVOH nanocomposite fabricated by EHDA has been shown in Fig. 2.22 (a,b), it can be observed that hBN nanoflakes are well mixed in the polymeric network of PVOH and wrapped up by the polymer. Both the images show the composite formation is uniform and smooth.

Raman spectroscopy was used to investigate the exfoliation of BN 2D flakes. Fig. 2.23 (a) shows the Raman spectra of both bulk and exfoliated BN flakes.

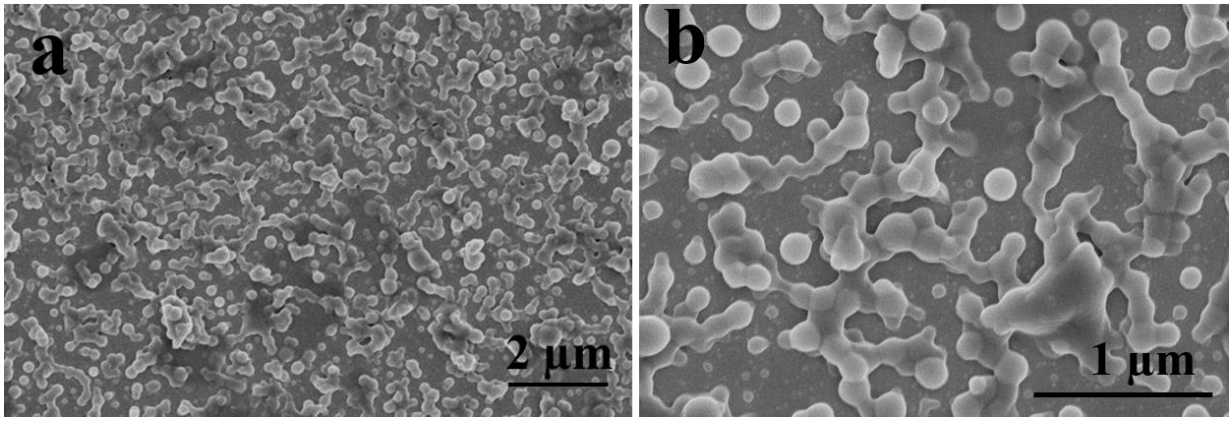

Fig. 2.22. (a,b) FESEM images of the thin film of hBN/PVOH nanocomposite deposited by EHDA.

The E_{2g} vibrational mode is observed in unexfoliated or pristine and exfoliated hBN which is the characteristic of hBN structure. In pristine hBN the E_{2g} mode is observed at 1367 cm $^{-1}$ while in exfoliated hBN it is observed at 1370 cm^{-1} [45,46]. So, there is a blue shift of the E_{2g} vibrational mode up to 3 cm^{-1} in exfoliated hBN which is quite comparable with the earlier reported results [46,47].

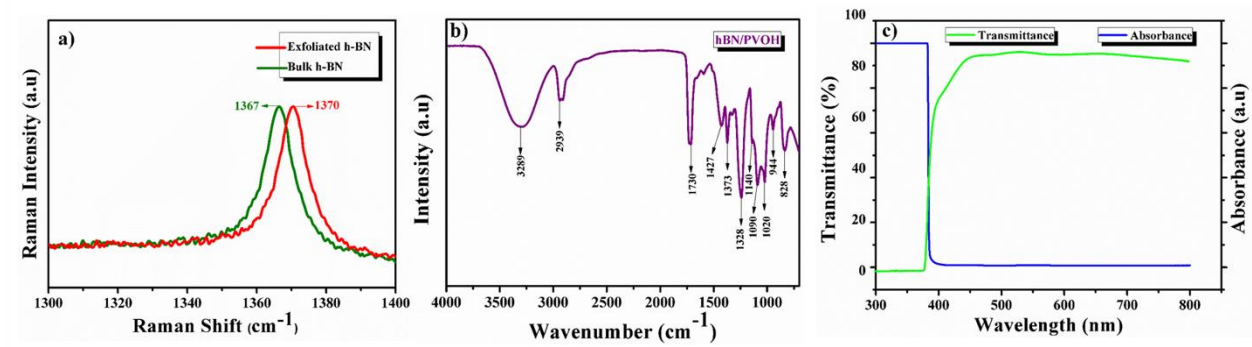

Fig. 2.23. Optical characteristics; a) Raman spectra of as exfoliated hBN nanosheets showing E_{2g} vibrational mode of bulk and exfoliated phases at 1367 cm^{-1} and 1370 cm^{-1} respectively. b) FTIR spectra of PVOH, hBN and their composite demonstrating the compositional analysis of aforementioned materials. c) UV/Vis analysis of as deposited hBN/PVOH nanocomposite thin film as deposited by EHDA showing low absorbance and high transmittance.

To get information about the composition of the hBN/PVOH nanocomposite thin film, FTIR spectroscopy was used. FTIR spectrum of hBN/PVOH nanocomposite thin film has been exhibited in Fig. 2.23 (b) which has both the characteristics bands of hBN and PVOH. Only two distinct peaks one at 828 cm^{-1} and other at 1373 cm^{-1} belong to the hBN. The peak at 828 cm^{-1} can be attributed to the out of plane B−N−B bending vibration (A_{2u} mode) and peak at

1373 cm^{-1} can be attributed to the in-plane B−N ring stretching vibration (E_{1u} mode)[61,62]. Rest of the peaks present in the given FTIR spectra belong to PVOH and have well resemblance with already reported FTIR analysis of PVOH in literature[63,64]. The large and broad band at 3289 cm^{-1} is attributed to O−H stretching vibration from intermolecular and intramolecular hydrogen bonds. The bands at 2939 cm^{-1} and 1427 cm^{-1} are due to the C−H stretching and C−H bending vibration of alkyl group whereas the absorption band at 1730 cm^{-1} is attributed to the C=O and C−O from acetate group. The peak at 1140 cm^{-1} is considered an important peak in the spectrum of PVOH because it exhibits the semi crystalline nature of PVOH. The twin peaks at 1020 cm^{-1} and 1090 cm^{-1} correspond to the C−O bonding in the structure of PVOH. The absorption band at 944 cm^{-1} may be attributed to the out of plane deformation of intra-/intermolecular hydrogen bonded OH groups while the band at 1328 cm^{-1} arises due to the O−H bending vibration.

Fig. 2.23 (c) shows the UV/Vis analysis of as deposited hBN/PVOH thin film in which both transmittance and absorbance spectra are presented. It has shown the low absorbance and high transmittance of the nanocomposite thin film which is considered appreciable in modern electronic devices.

2.8. Nanocomposite of ZnO NWs/$ZnSnO_3$ NCs

ZnO NWs were grown on flexible substrate via aqueous solution method as describes in section 2.2 while $ZnSnO_3$ NCs were synthesized via hydrothermal method as described in section 2.4. $ZnSnO_3$ NCs were sprayed o through EHDA on as grown ZnO NWs, some of the NCs were infiltrated through the pores of ZnO NWs while maximum remained with random orientation on top of NWs.

2.8.1 Characterization ZnO NWs/$ZnSnO_3$ NCs nanocomposite

The morphology of the composite of ZnO NWs and $ZnSnO_3$ NCs has been examined in Fig. 2.24 (a,b). It can be observed that $ZnSnO_3$ NCs are randomly scattered onto ZnO NWs; some

of them have been infiltrated into the pores of NWs while most of them are on the top covering the NWs thoroughly.

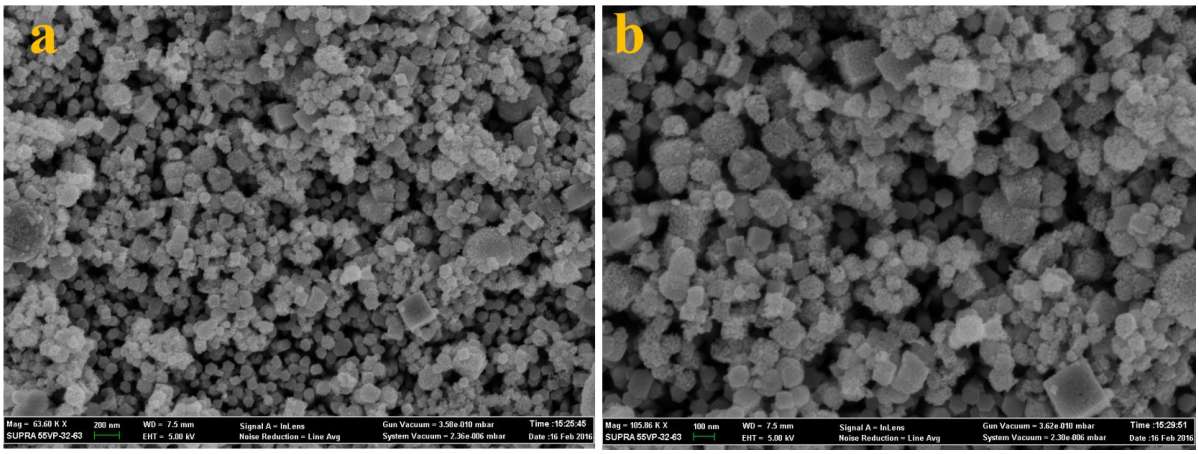

Fig. 2. 24. (a,b) $ZnSnO_3$ NCs are interspersed onto ZnO NWs and some of the NCs are incorporated into the pores of NWs.

Fig. 2.25 demonstrates the X-ray diffraction patterns of nanocomposite material i.e. ZnO NWs and $ZnSnO_3$ NCs. It can be observed that both the materials are present in the sample in their crystalline forms.

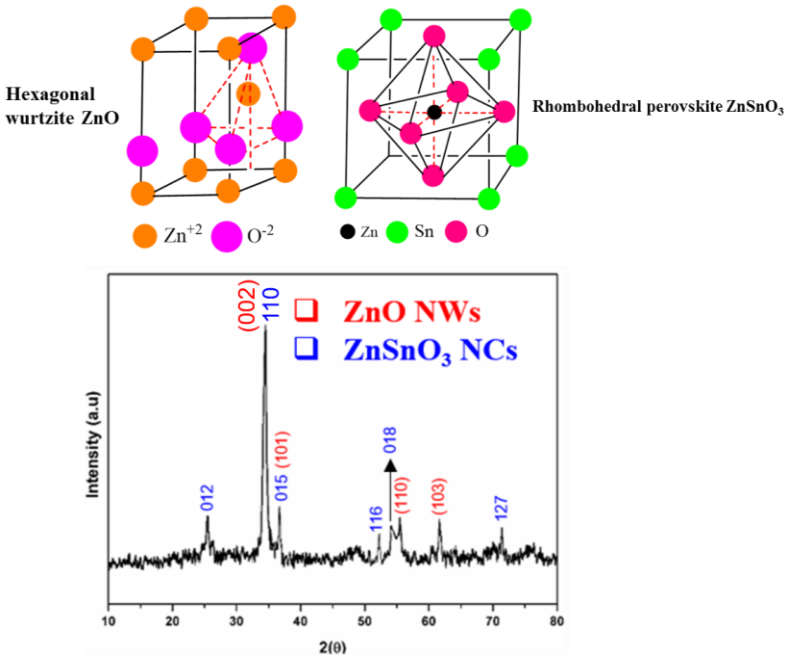

Fig. 2.25. XRD spectra of ZnO NWS/ZnSnO3 nanocomposite showing the characteristic peaks of both materials confirming their hexagonal wurtzite and rhombohedral structures respectively.

The planes (002) and (110) belong to ZnO NWs and ZnSnO3 NCs respectively and both planes are shown by a single peak that proves the effective formation of nanocomposite of $ZnO/ZnSnO_3$.

Chapter 3- Device Fabrication and Results

Organic-inorganic hybrid nanocomposite is an attractive choice for various electronic device applications. Owing to the unique properties of the developed materials and nano-composites, we fabricated different resistive memory devices and sensors and investigated their performance to evaluate the physical and electrical properties of the developed materials for device application. The devices show excellent output response characteristics when compared to the similar works done in the related fields.

3.1. Memristor based on hBN/Polymer nanocomposite

We have explored the memory effect in a device, based on a 2D material; boron nitride (BN) and a polymer; polyvinyl alcohol (PVOH). This memory device has been fabricated on a flexible ITO coated PET substrate by using an all printed approach including Electrohydrodynamic atomization (EHDA) and reciprocating head (RPC). The fabricated device displayed nonvolatile, rewritable and characteristic bipolar resistive switching at a low current compliance and small operating voltage. Conduction mechanism was deduced to be conductive filamentary and verified by the effect of temperature and device size on switching characteristics. Remarkably stable and repeatable results of electrical and mechanical characterization makes this hybrid nanocomposite a potential candidate for the future flexible, robust and low power nonvolatile memory.

3.1.1 Device Fabrication

Thin film of hBN/PVOH nanocomposite was fabricated on ITO coated flexible substrate (PET) by our own in-house built, non-vacuum based EHDA printing system. EHDA has been proved

as a very useful printing technique for deposition of variety of materials including nanocomposite of organic and inorganic materials as thin films. Details of the EHDA system can be found in our earlier reported work[65–69]. For this work, a highly uniform thin film was fabricated by optimizing the different parameters of the EHDA system like flow rate, stand-off distance (the distance between the nozzle and substrate), nozzle size, speed of the moving stage, and applied voltage to the stage and nozzle to obtain the stable cone jet. The flow rate was set 200 µl/h and stand-off distance was fixed 20 mm. ITO coated PET substrate was placed on the moving stage which was moving with the speed of 3mm/sec. The metallic nozzle having internal diameter of 210 µm was used for spray and stable cone jet was obtained between the applied voltages of 5-5.7 KV.

Finally the top circular Ag electrode with three different diameters were deposited by using Ag nanoparticles ink through a glass needle. The capillary force holds the high viscosity Ag nanoparticle ink within the chamber. The stage can move in XY axis with the movement of needle in the Z axis. This process is extremely controllable and has the precision of micrometer scale. This task was performed via employing the in-house developed reciprocating head (RPC) printing system shown in Fig. 3.1 (a). A non-contact printing method like RPC has the advantage that it patterned the top electrode without making even a slight contact with the functional thin film of resistive switch hence protecting the device from possible short circuit. This system has the micrometer precision. The patterning size can be controlled by varying the size and velocity of needle, standoff distance and pneumatic pressure of ink chamber respectively. The diameter of the needle holder was 1 mm and needles of different diameters i.e. 42 µm, 70 µm and 100 µm were used with a standoff distance of 100 µm. Top electrodes with three different diameters 42 µm, 70 µm and 100 µm were successfully deposited to observe the area dependence of bistable resistive states as shown in Fig. 3.1 while the velocity of the

needle was 0.05, 0.03 and 0.02 mm/s to deposit these electrodes. The pneumatic pressure for each dot was kept constant at 0.2 kPa.

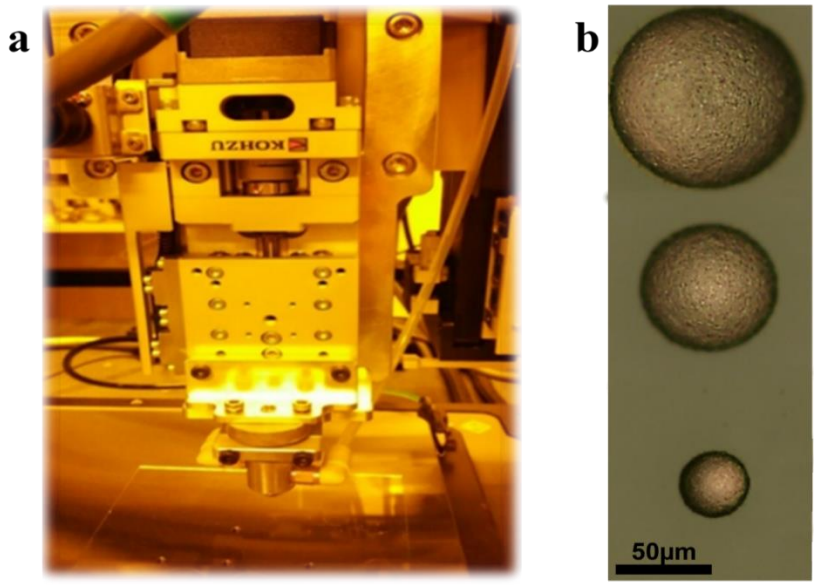

Fig. 3.1. Optical images of a) RPC printing head b) patterned circular top electrodes by RPC head with three different sizes 42 µm, 70 µm and 100 µm respectively.

3.1.2 Device Characterization and Results

Electrical characterization of hybrid hBN-PVOH based memory device was carried out by applying positive biased voltage to the top Ag electrode while grounding the bottom ITO electrode. Electroforming was performed to obtain repeatable and highly stable results of bipolar resistive switching as illustrated in Fig. 3.2 (a) followed by applying double voltage sweep from -1 to +1 volts. DC bias was applied across three different device sizes with a diameter of 42 µm, 70 µm, and 100 µm respectively. Characteristic semi-logarithmic I-V curves displayed typical bipolar resistive switching in hBN/PVOH nanocomposite as illustrated in Fig. 3.2 (b-d). Initially the device was in high resistance state (HRS). Current slightly kept increasing until the applied voltage reached a threshold value (V_{th}) of ≈ 0.78 V. At V_{th} the fabricated device switched from HRS to a low resistance state (LRS) due to the abrupt increase in magnitude of flowing current. This process is known as SET or writing

process. It can be deduced from this information that data can be stored in this hybrid memory device at a voltage of ≈ 0.78 V.

It is evident from Fig. 3.2 (b-d) that no effect on set voltage (V_{set}) or reset voltage (V_{reset}) was observed with varying device size however a considerable change in the switching ratio can be observed at a read voltage of 0.26 V. The off/on ratio has an inverse relation with the device size i.e. the ratio tend to increase with decreasing device size.

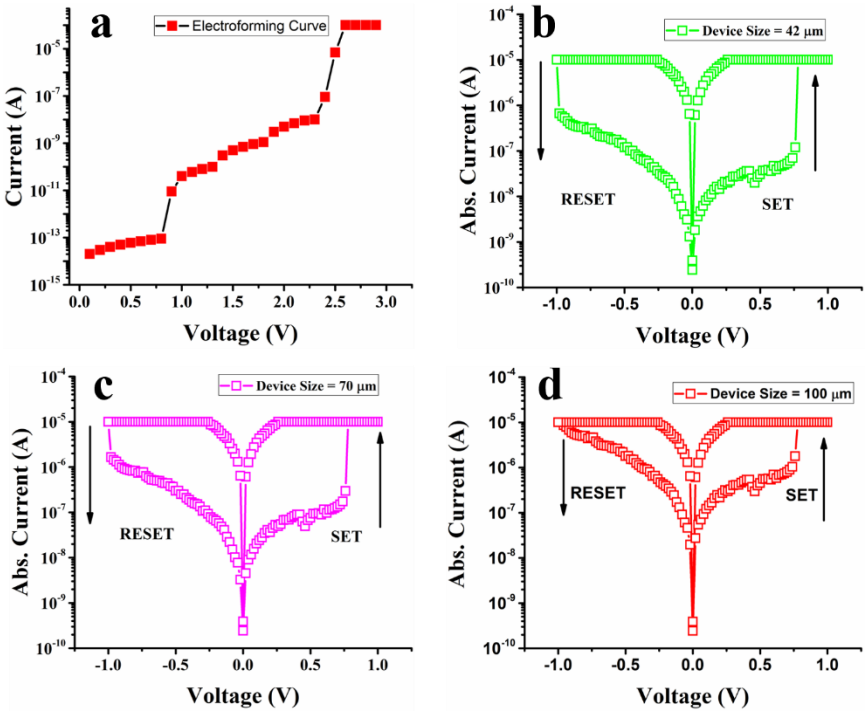

Fig. 3.2. Characteristic bipolar resistive switching curves of as prepared non-volatile flexible memory devices based on hybrid hBN/PVOH nanocomposite a) Electroforming I-V curve to obtain repeatable results by forming a conductive path for further experiments b) I-V characteristic curve of 42 µm device c) I-V characteristic curve of 70 µm device d) I-V characteristic curve of 100 µm device.

The effect of device size on the resistive switching properties will further be elaborated in the conduction mechanism part. Non-symmetric nature of characteristic I-V curves was due to the selection of electrodes with dissimilar work function value. A decent off/on ratio at a read voltage (V_{read}) of 0.26 V was recorded to be equal to 4.8×10^2, 1.9×10^2, and 32.3 for 42 µm, 70 µm, and 100 µm respectively that is enough to distinguish HRS from LRS.

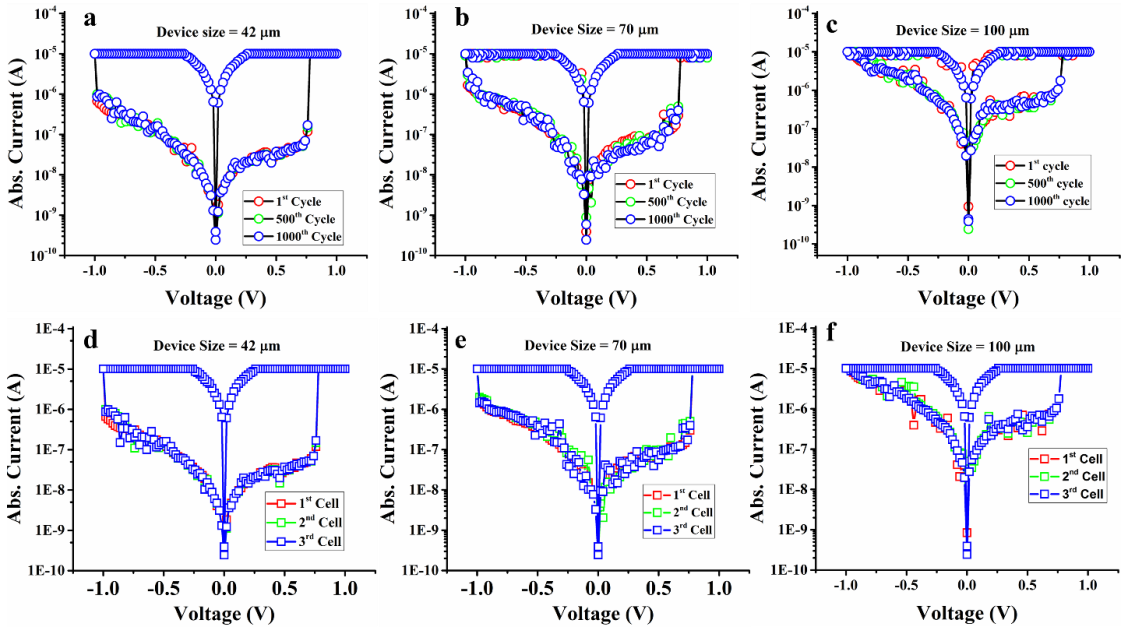

Fig. 3.3. I-V characteristic curves of three different device sizes illustrating excellent endurance and repeatability of bipolar resistive switching a-c) Illustration of high electrical endurance with 42 µm, 70 µm and 100 µm device size for 1000 biasing cycles. These curves are showing that the fabricated device has excellent repeatability validating the high dependability on fabrication technique d-f) I-V curves of each of the three fabricated memory cells with similar top electrode diameter of 42 µm, 70 µm and 100 µm respectively illustrating remarkable repeatability of fabricated devices.

Electrical endurance of each device was tested against 1000 biasing cycles and the characteristic I-V curves showed high stability as illustrated in Fig. 3.3 (a-c). The fabricated device illustrated excellent repeatability when I-V curves of three different memory cells with similar device size were plotted against each other as shown in Fig. 3.3 (d-f). Cumulative plot of threshold voltages (V_{SET} and V_{RESET}) and both resistive states (HRS and LRS) were plotted to illustrate their high stability as displayed in Fig. 3.4 (a, b). Switching ratio of each device size tend to decrease with increasing value of biased voltage as shown in Fig. 3.4 (c).

In order to understand the switching mechanism of fabricated device, we plotted double logarithmic I-V curves and the dependence of bistable resistive states on device size and temperature. The double logarithmic I-V curves as shown in Fig. 3.5 (a-c) illustrate that the conduction mechanism for all the devices with three different sizes is the same with the only difference of gap between both resistive states i.e. variable off/on ratio. The slope of HRS can be divided into three categories. Initially when the applied voltage value is too small, the slop

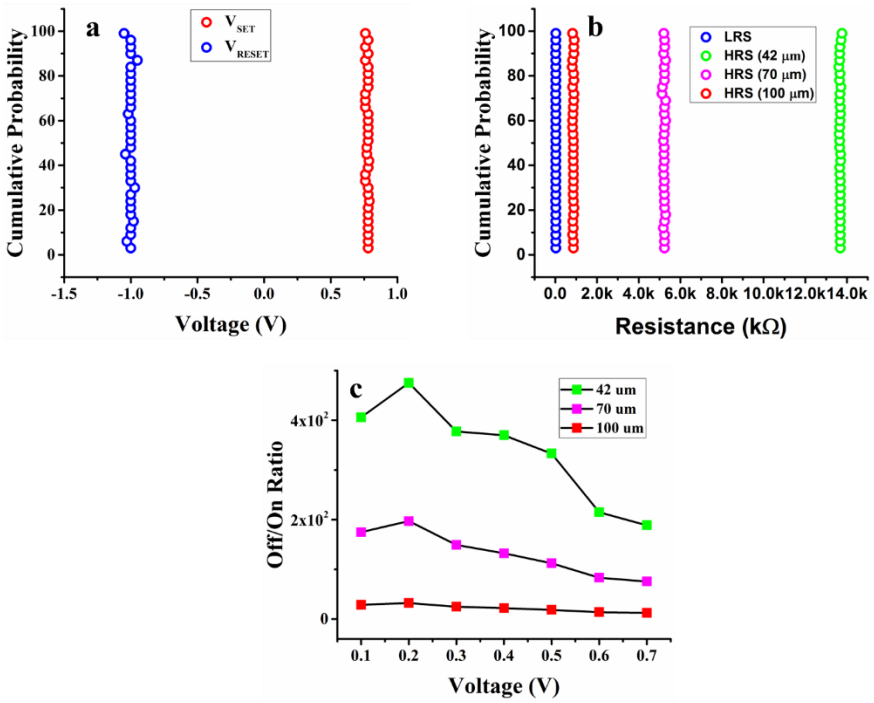

Fig. 3.4. Cumulative Probability plots of threshold voltages and bistable resistive states a) VSET and VRESET b) LRS and HRS of all the three device sizes. All these readings have been taken at a read voltage of 0.26 V c) Inverse relation of off/on ratio with applied external biasing voltage.

is ≈ 1 implying an Ohmic behavior represented as I α V. Such behavior is possibly due to a few charge carriers generated through thermionic emission at low electric field. As the applied bias increases, charge carriers depleting from the metal electrode also increases exponentially with a slope > 2 represented as $I \alpha V^m$. The conduction in HRS seems to be due to the hopping of charge carriers within the available trap states present inside the active layer of hybrid nanocomposite that can be explained by variable range hopping (VRH) model. The conduction at lower electric field can be described mathematically as:

$$\Sigma = 2e^2R^2N(E_F)v_{ph}\exp(-2\alpha R - W/K_B\,T)$$

Where, $W =$ Energy difference between two trap states, $v_{ph} =$ Electron- Phonon relation.

As the applied voltage reaches to V_{SET}, a sudden increase in the current flow is observed possibly due to the formation of a conductive path interconnecting bottom and top electrode. Formation of a conductive channel will be further discussed below with the help of area and temperature dependence plots of resistive states in Fig. 3.6. The device follows Ohmic behavior

after switching to LRS as the slope value of double logarithmic curve is ≈ 1. These results prove that the conduction mechanism observed in our devices is typical trap controlled space charged limited current (TCSCLC) which can be represented mathematically as:

$$ITCSCL = 9A\varepsilon_{\circ}\varepsilon_{r}\mu V^{2}/8d^{3}$$

Where A = junction area, I = Current Density, V = Bias Voltage, $\varepsilon_{\circ}$ = Permittivity of free space, and ε_{r} = relative dielectric constant, and μ = mobility of charge carriers.

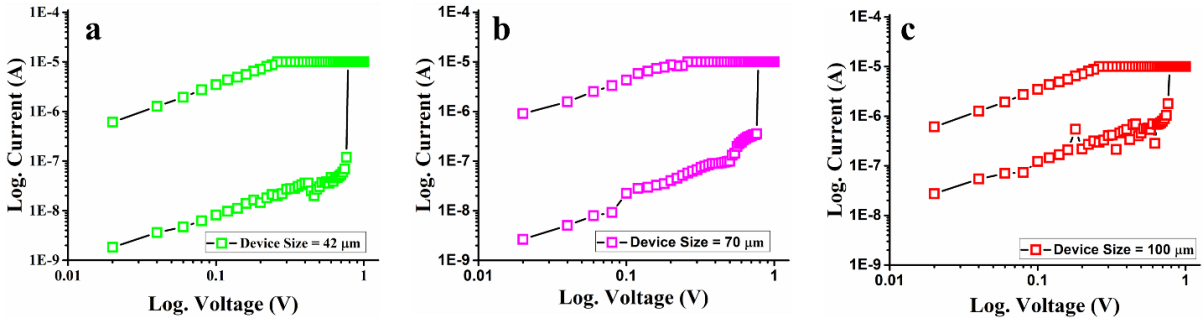

Fig. 3.5. Double logarithmic curves of all the three fabricated devices with different sizes illustrating that all of them follow the same conduction mechanism of TSCLC based on their slope values.

To further understand the conduction mechanism, size dependence of HRS and LRS for each memory device was plotted as illustrated in Fig. 3.6 (b). It was observed that LRS is independent of device size while HRS tend to decrease with increasing device size. The independence of LRS on device area validates the formation of metal filament. Both resistive states were plotted against temperature to further validate the idea of conduction mechanism due to formation of metallic filament. Increasing value of LRS with temperature confirms the metallic behavior owing to the positive temperature coefficient of metals as illustrated in Fig. 3.6 (c). The metallic conductivity can be represented mathematically as [70]:

$$R(T) = R_{\circ}[1 + \alpha(T - T_{\circ})]$$

Where $R_{\circ}$ = Resistance at $T_{\circ}$ (300 K) and α = temperature coefficient.

However, HRS decreases with increasing temperature hence illustrating a negative temperature coefficient which is a characteristic of insulators. The off state conductance of this device can represented as [70]:

$$I_{OFF} = I_{\circ} \exp(-E_a/KT)$$

Where k = Boltzman constant and E_a = Thermal activation energy.

The formation of metallic filament is due to the oxidation of top silver electrode under the influence of strong electric field. This loss of electrons results in the formation of Ag^+ cations that are injected into the active layer. The Ag^+ cations are not able to travel far owing to their low mobility in the insulating layer of hBN-PVOH. These cations are reduced by the trapped electrons in the nearby trapping states hence forming the metallic filament as an extension of the top electrode. The subsequently injected Ag^+ cations then travel to the next hopping site mostly near the edge of already formed filament where they are reduced again causing the enhancement of metallic filament formation. This filament is localized and its thickness decreases downwards until it reaches the bottom electrode that acts as the sink for cations. More than one conductive paths can be formed however, the first complete filament mask other nano filaments.

The formed filament does not break even if the externally applied electric field is turned off referring to the nonvolatile nature of fabricated memory device. In order to switch off the fabricated device, the formed filament should be ruptured by applying voltage of opposite polarity. It is not necessary to totally abolish the formed filament, only a little break disengages the conductive path. When negative bias was applied, dissolution of metallic filament occurred possibly near the bottom electrode where the current density is maximum (RESET process). The rupture of filament occurs due to Joule heating and electrochemical process. Such a formation and rupture of metallic filament is reported in other memory devices as well[71–74]. The complete process of metallic filament formation and rupture is illustrated in Fig. 3.6 (a).

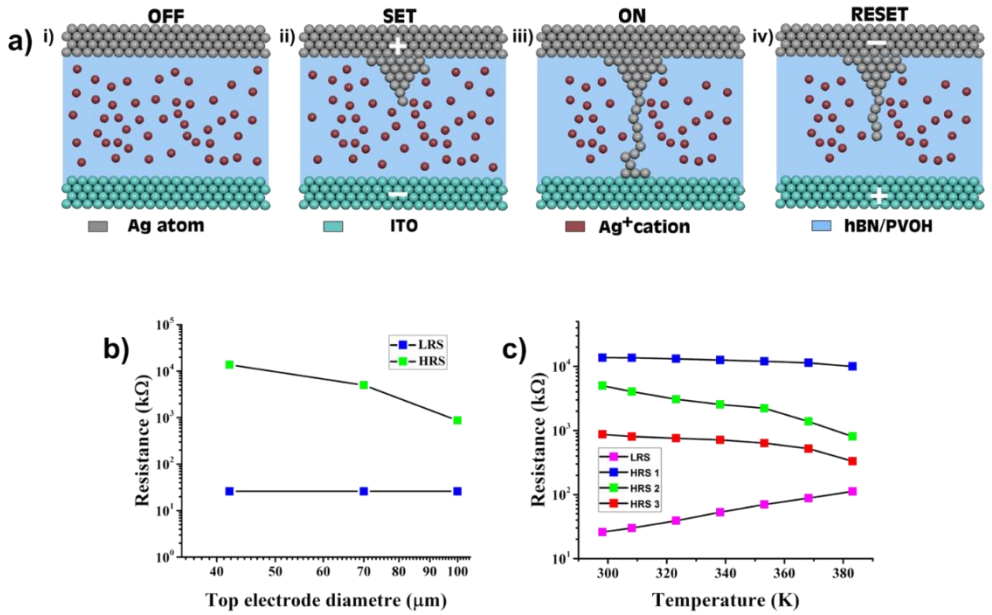

Fig. 3.6. Illustration of formation and rupture of metallic filament from top electrode to bottom electrode under the influence of strong electric field i) Off process in which atoms of Ag electrode oxidize and become Ag+ cations by losing electrons ii) SET process in which the trapped electrons begin to neutralize the Ag+ cations thus resulting in the formation of metallic filament within the functional layer of hBN-PVOH iii) At this point the metallic filament is completely formed from top to bottom electrode bringing the device into ON state iv) The formed filament is ruptured by applying electric potential of opposite polarity resulting in HRS b) Change in HRS and LRS with varying device size c) Dependence of bistable resistive states on temperature.

Keeping in view the gigantic growth of flexible electronics for wearable and bendable applications we fabricated our memory device on a flexible PET substrate. We tested the mechanical strength of our device by bending it at various diameters ranging from 500 mm to 4 mm as illustrated in Fig. 3.7 (a). No prominent change was observed in either of the two resistive states (i.e. HRS and LRS). Furthermore, the mechanical robustness of fabricated device was tested against 1500 bending cycles at a fixed bending diameter of 15 mm by quenching it in the jaws of an in-house build mechanical machine for backward and forward motion. The results of mechanical endurance were highly repeatable as illustrated in Fig. 3.7 (b). The schematic diagram of flexible memory device is shown in Fig. 3.7 (c) in a bend state with labelling of each part while the inset shows the optical image of real device. These bendability tests prove that hBN-PVOH hybrid nanocomposite based memory device is highly suitable for flexible electronics applications.

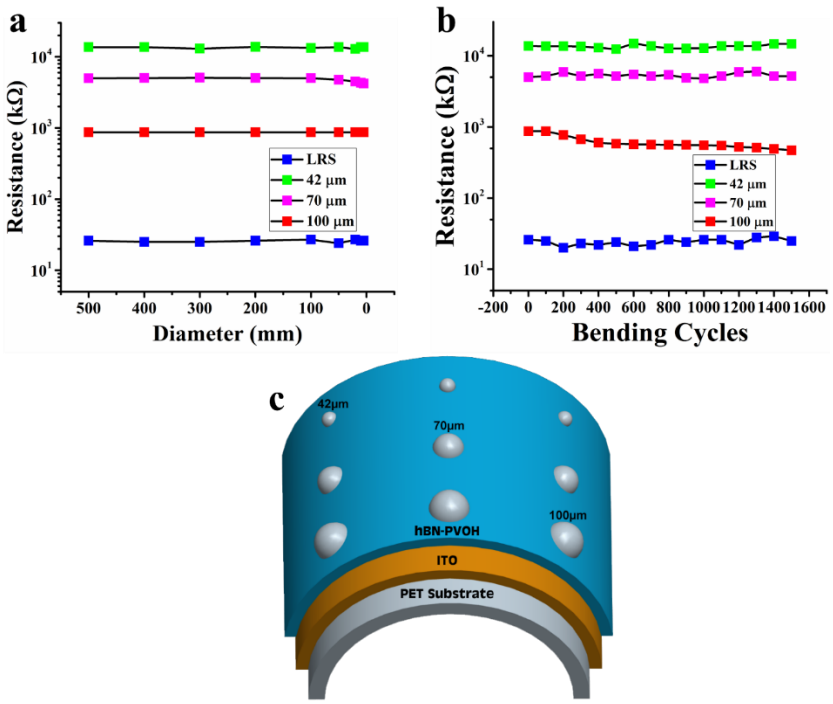

Fig. 3.7. Mechanical Bending test of the hybrid nanocomposite of hBN-PVOH to examine its possible application in flexible electronic devices a) Maximum bending diameter up to which the performance of fabricated flexible memory device is showing highly repeatable results b) Mechanical bendability plot of the fabricated device illustrating highly stable results after 1500 bending cycles c) Layer by layer schematic diagram of ITO/hBN-PVOH/Ag resistive switch in bend state with labelling of each part and beside schematic the optical image of real device in bending state is shown.

The nonvolatile memory device based on hybrid hBN-PVOH nanocomposite exhibited superior electrical and mechanical characteristics such as better off/on ratio, high retention time, lower current compliance, superior endurance, low operating voltage and remarkable mechanical robustness when compared with already reported resistive switching devices based on PVOH nanocomposites with other materials [75–77].

3.2. Memristor based on $ZnSnO_3$ and PVOH composite

Resistive switching effect has been explored in the hybrid nanocomposite of organic-inorganic materials by fabricating all printed memristive device on a flexible PET substrate. Configuration of as fabricated device is Ag/PVOH-$ZnSnO_3$/Ag. Electrical and mechanical characterization showed that resistive switching characteristics of $ZnSnO_3$ were remarkably enhanced by adding PVOH polymer in it. The fabricated device showed bipolar, nonvolatile and rewritable memory behavior at low operating voltage. A high off/on ratio, endurance and

retention time of > 10^2, 500 voltage cycles and 36 hours respectively were recorded without any substantial change in either HRS or LRS.

3.2.1 Device Fabrication

Perovskite oxide and polymer based memory device was fabricated on a flexible and transparent polyethylene terephthalate (PET) substrate. Prior to fabrication, substrate was cleaned by acetone, ethanol and deionized water for 10 min each in a bath sonicator followed by drying in open air. After that substrates were placed in a UV ozone cleaning system to dissociate the contaminant molecules from the surface. In order to further enhance the wettability of the surface, substrates were treated with oxygen plasma.

Moon et.al have recently reported a novel direct contact printing method known as reverse offset for patterning high quality electrodes. This system has the ability to print extremely tiny and complicated structures with uniform thickness [78]. Reverse-offset roll-to-plate printing technique offers high quality surface, simplicity, high resolution, and low resistivity to obtain precise and accurate patterns for electronic device applications [79]. The whole process of reverse offset printing system includes a glass slide to deposit ink, a roller enfolded with a blanket of highly hydrophobic poly-dimethyl siloxane (PDMS) material, a cliché containing the negative of electrode patterns acutely carved on its surface in the form of trenches and finally the chosen substrate for device fabrication. Whole printing process is presented step by step in Fig. 3.8.

Initially Ag ink was spin coated on a coating substrate (glass slide in our case) at 3000 rpm as shown in Fig. 3.8 (a, b). The PDMS blanket roll was rolled over the spin coated Ag ink glass slide to attach a thin yet uniform layer of Ag ink owing to the high absorption coefficient of PDMS as shown in Fig. 3.8 (c). The design of cliché with the negative of bottom electrodes engraved on its surface is shown in Fig. 3.8 (d). Ink coated PDMS blanket roll was rolled over the cliché surface with optimized speed and pressure to transfer the electrode patterns on it by

leaving all the unwanted Ag ink on the cliché surface owing to its higher value of adhesion coefficient (Off Process) as illustrated in Fig. 3.8 (e). The blanket roll was rolled over the desired flexible PET substrate as the final step of printing high quality bottom Ag electrodes (Set Process) as shown in Fig. 3.8 (f). Extremely fine bottom Ag electrodes with 100 µm resolution and outstanding resistivity of 0.4 ohm-cm were realized after sintering for 1 hour at 110 ℃ in a furnace.

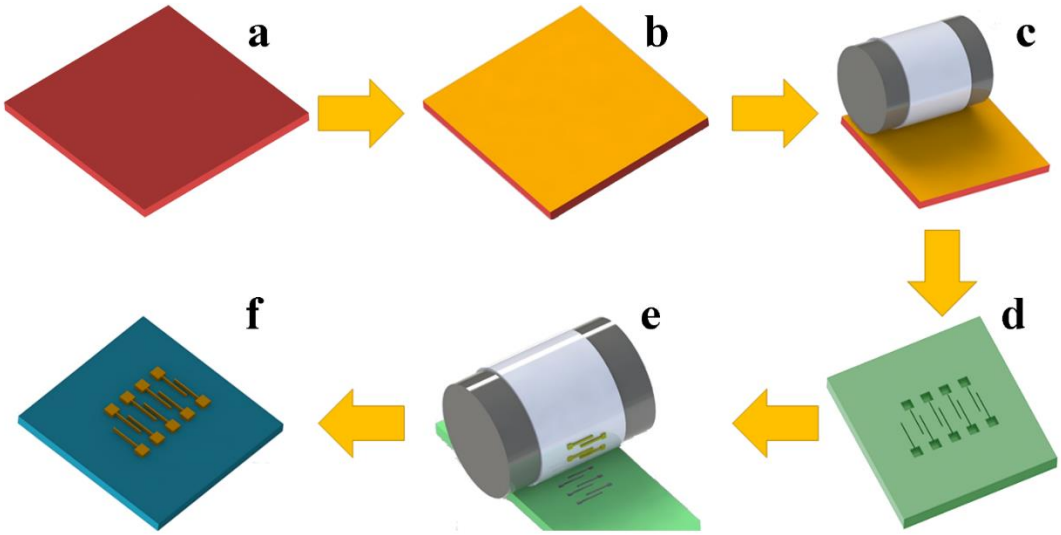

Fig. 3.8. 3D view of various parts of Reverse Off-Set printing system displaying the step by step patterning of bottom Ag electrodes on a flexible PET substrate a) Glass slide b) Ag nanoparticle ink spin coated on glass slide c) PDMS blanket roll lifting Ag ink from the glass slide d) Cliché design displaying the negative of desired bottom electrode patterns engraved on its surface e) Illustration of OFF Process in which PDMS blanket roll is shown to lift the electrode patterns from the cliché surface f) SET Process in which bottom Ag electrodes are transferred onto the desired PET substrate from the PDMS blanket roll.

EHD atomization is a well-established thin film deposition technique in printed electronics. It is a non-vacuum based printing technique to deposit thin films on atmospheric conditions. A variety of composite materials can be sprayed on various substrates by achieving the stable cone jet [68,69]**.** Thin film of PVOH-$ZnSnO_3$ nanocomposite was successfully deposited by using an in-house built EHDA system. EHDA was preferred due to its simplicity, high control, and ability to produce very thin yet uniform films in quick time [68]. Nanocomposite ink being sprayed by EHDA nozzle began to split into small droplets with increasing voltage. Spraying modes varied from dripping to multi-stable jet after passing through micro-dripping, unstable jet and stable jet. The spraying mode was controlled by controlling the parameters of applied

voltage, distance of nozzle from the substrate, nozzle diameter and set value of flow rate. Stable cone jet was achieved between 5.4-6.2 kV at 15 mm stand-off distance at a flow rate of 300 µl/h.

EHD patterning system was employed to deposit top Ag electrode. Non-contact method of EHD patterning was preferred over other contact based printing techniques such as gravure offset, reverse offset and screen printing to avoid possible damage to the PVOH-ZnSnO3 nanocomposite thin film. The Ag nanoparticles (<100 nm) ink was used for EHD pattering having concentration up to 60 wt.% and viscosity 42 cps. The main difference between the EHD atomization and EHD pattering is the stand-off distance (the distance between the nozzle and substrate). A very fine line is obtained by optimizing the parameters of EHD system like nozzle size, stand-off distance, applied voltage and flow rate [80]. In this experiment, a metallic nozzle of 30 µm orifice was used while stand-off distance was ~ 5 µm. The flow rate was kept at 70 µl/h for maintaining the constant pressure of Ag NPs ink to achieve uniform and continuous ejection through the nozzle. The high electric potential (4.0 kV) was applied between the metallic nozzle and moving stage until the attainment of stable meniscus and continuous ejection of ink. A single straight line of Ag nanoparticles ink with ~ 30 µm width and 9 mm length was successfully deposited as the top electrode without damaging active thin film or bottom Ag electrodes. Top Ag electrode was sintered at 110 ℃ for 1 hour. The deposited electrode was highly conductive with its measured resistivity of only 0.4 ohm cm-1. Total area of as fabricated Ag/PVOH-ZnSnO3/Ag single memory cell was 30 µm × 100 µm.

3.2.2 Device characterization and results

Electrical characterization of Ag/ PVOH-$ZnSnO_3$/Ag based memory device was performed to analyze its resistive switching behavior. Top electrode was positively biased while bottom electrode was connected to ground. The electrical characterization was carried out in the operating voltage range of -1.5 V to +1.5 V while current compliance was set at 100 mA to

protect the memory device from excessive current flow that could result in device breakdown. Typical semi-logarithmic curve for bipolar resistive switching were obtained as a result of DC biasing as illustrated in Fig. 3.9 (a). Initially the memory device was in HRS. Current began to slightly increase due to applied external bias while maintaining its original HRS. At a voltage of ~ 1.5 V, a sharp increase in the current value took place resulting in a clear resistive switching from HRS to LRS. This transition is known as the writing process in which a bit is stored in the device at a specific voltage value known as threshold voltage (V_{th}). It can be inferred from this information that data can be stored on this memory device at an extremely low voltage of ~1.5 V.

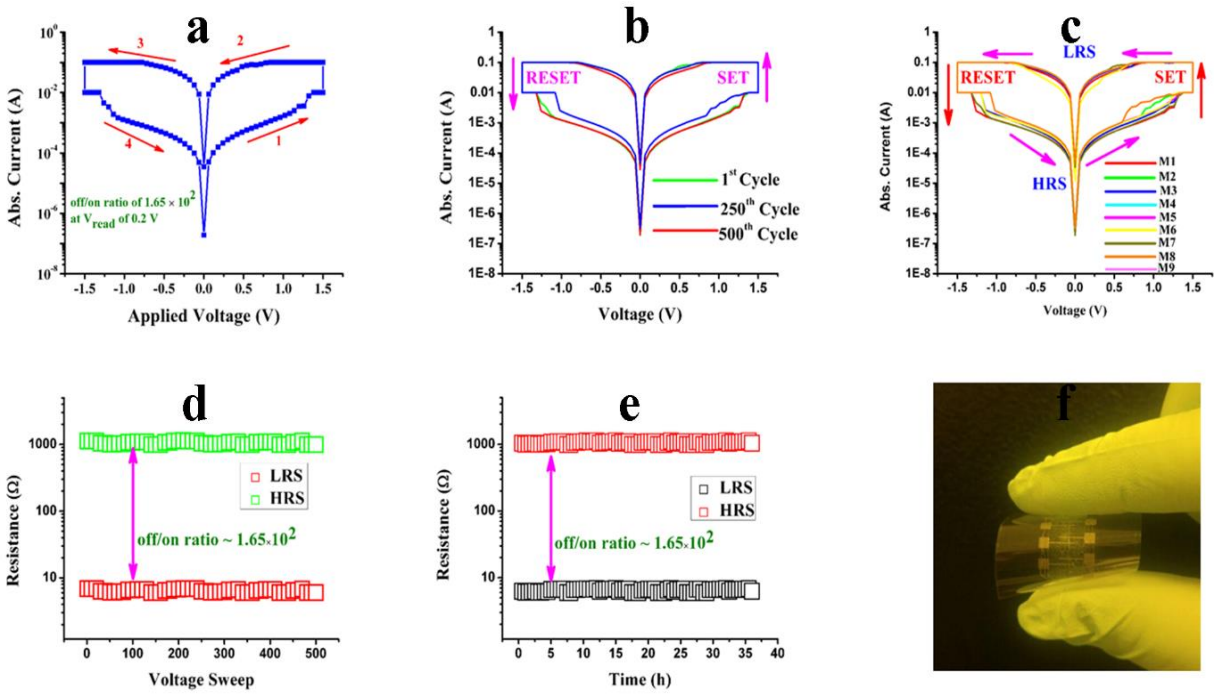

Fig. 3.9. Electrical characterization of as prepared all printed, flexible and hybrid organic-inorganic memory device based on PVOH-$ZnSnO_3$ nanocomposite a) Typical log I-V characteristic curve of a memristor illustrating bipolar resistive switching at a threshold voltage of ~ 1.5V b) Semi-logarithmic I-V curves displaying excellent repeatability for 1st, 250th, and 500th cycle c) Typical semi logarithmic I-V curves showing the bipolar resistive switching effect in all the 9 memory cells of a 9 × 1 matrix of as prepared memory device where M1-M9 signify the labels of 9 memory cells respectively d) Endurance of memory device showing the value of both resistive states for each voltage sweep over 500 voltage cycles while maintaining the off/on ratio of > 102 measured at a reading voltage of 0.2 volt e) Retention of HRS and LRS measured for a longer period of time without any noticeable deviation with an off/on ratio of 1.65×102. All the resistance values were recorded at a reading voltage of 0.2 volts f) Optical Image of as fabricated Ag/PVOH-$ZnSnO_3$/Ag memory device on a flexible PET substrate in bend condition.

A decent off/on ratio of 1.65×10^2 at a read voltage (V_{read}) of 0.2 V was recorded for PVOH-$ZnSnO_3$ nanocomposite based memory device. This value of off/on ratio is high enough to easily distinguish between the two resistive states. Durability of this memory device was tested against 500 voltage sweeps and invariable change in HRS and LRS was observed signifying high endurance value as compared to other reported composites of PVOH as displayed in Fig. 3.9 (b). The as fabricated memory device consisted of an array of nine memory cells. Characteristic semi-logarithmic I-V curve for each memory cell was recorded against each other that showed an excellent repeatability as shown in Fig. 3.9 (c). Endurance of both HRS and LRS for 500 voltage sweeps displaying high stability is illustrated in Fig. 3.9 (d). The time for which a memory device holds its data without the supply of an external voltage source known as retention is another important parameter to evaluate the performance of a memory device therefore we tested our device for 36 hours. Both LRS and HRS showed high stability over this duration without any major deviation that makes it useful for nonvolatile memory applications as illustrated in Fig. 3.9 (e). Optical image of flexible, nonvolatile and rewriteable PVOH-$ZnSnO_3$ nanocomposite based memory device is shown in Fig. 3.9 (f). The resistive switching characteristics our device based on hybrid nanocomposite have been compared with previously reported memory device of only $ZnSnO_3$ and other nanocomposites of PVOH in Table 3.1 and Table 3.2 respectively. Several other memory devices with resistive switching effect in the hybrid nanocomposites of conductive nanoparticles embedded in polymer have also been reported in the past [81–84].

Table 3.1. Comparison of PVOH-$ZnSnO_3$ nanocomposite based memristive device with already reported $ZnSnO_3$ memory device as reported in our previous work. It is evident from the mentioned results that PVOH plays a vital role in improving the resistive switching characteristics of $ZnSnO_3$ based memory device.

Configuration	Substrate	Off/On Ratio	Endurance	Retention	Mechanical Robustness	Bendability	Ref
Ag/PVOH-$ZnSnO_3$/Ag	PET	1.65×10^2	500 cycles	36 hours	1500 cycles	Up to 4 mm	
Ag/$ZnSnO_3$/Ag	Glass	10	100 cycles	24 hours	-	-	[25]

- Represents that this data value was not presented in the reported work.

Table 3.2. Comparison of PVOH-$ZnSnO_3$ nanocomposite resistive switching characteristics with already reported other nanocomposite of PVOH polymer.

Active Layer	Voltage Sweep (V)	Off/On ratio	C.C	Endurance	Retention	Ref
PVOH-$ZnSnO_3$	-1.5 to +1.5	1.65×10^2	100 mA	500 cycles	10^5 s	
GNF–PVOH	-7 to +2	~ 10^2	1 mA	100 cycles	1×10^4 s	[85]
AgNW-PVOH	-10 to +10	~ 10	10 mA	160 cycles	-	[86]
PVOH-PbS	-30 to +30	< 10	30 µ A	-	-	[87]
PEDOT:PSS-PVOH	-2 to +2	~ 10^2	100 mA	-	36×10^4 s	[76]

- Represents that this data value was not presented in the reported work.

Several conduction mechanisms have been suggested for resistive switching such as Space Charge Limited Current (SCLC), Ohmic Current Model, Filament Formation, Thermionic Emission, Interface-Type Switching, Electric-Field-Induced charge transfer, the Simmons and Verderber (SV) model etc. [88]. However the proposed conduction mechanism responsible for the resistive switching in PVOH-$ZnSnO_3$ based nonvolatile memory device from low to a high conductivity state is trap controlled space charge limited current (TCSCLC) in HRS while Ohmic model satisfies the conduction of charge carriers in LRS. These two models are deduced from linear fitting of double logarithmic I-V curve Fig. 3.10.

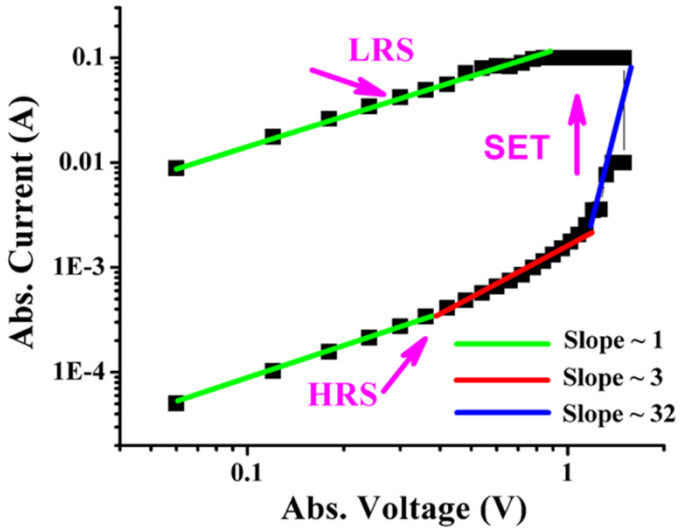

Fig. 3.10. Double logarithmic I-V curve illustrating the slopes for LRS and HRS with unique gradient values. This plot can be distributed into three separate regions as represented by the three different colors. In the green line region, Ohmic conduction takes place as gradient ≈ 1. The red line is the Child's law region as the gradient value ≈ 3. The blue line shows the region of sharp current increase as gradient ≈ 32 where the device switches from HRS to LRS.

These results are comparable to other reported resistive switching mechanisms in PVOH polymer [85], perovskite oxides [89,90] and hybrid organic-inorganic semiconductors [82,91–

95]. Conduction of charge carriers in region I (0.1-0.3 V) is mainly due to thermionic emission owing to the small electric field resulting in Ohmic behavior ($I \propto V$) [82,91–94]. In region II (0.3-1 V), electrons of metallic electrodes gain enough energy and charge transfer into the active layer of $ZnSnO_3$-PVOH nanocomposite takes place. After that, the current abruptly increases and reaches the compliance current value at an applied voltage of 1.5 V. The device follows the SCLC conduction model with an exponential relation between current and applied external voltage ($I \propto V^n$) [82,91–94]. At this point all the available traps within the active layer are filled with charge carriers resulting in the sharp transition from HRS to LRS. Moreover perovskite oxides like $ZnSnO_3$ may contain several types of defects comprising of interstitials, vacancies, and cation substitutions. Vacancy facilitated diffusion is a typical process in ABX_3 type structures. Charge trapping under the influence of electric field and defects migration can both be responsible for the resistive switching behavior of perovskite materials. Vacancy defects hop from one atom to another atom and generate narrow energy levels in the bandgap. Vacancies were dispersed within the perovskite layer before the application of external electric field. When the electric field was applied, these charged vacancies actively participated in conduction process by moving towards oppositely charged electrodes during the set process. These vacancies were neutralized by electrons once they reach the surface of the electrode. These defects form traps that play the role of conducting path as the charge carriers begin to move from one electrode to other electrode under the influence of external applied electric field by hopping through these traps. Primarily, the electrons prefer to reside in energy states with lower mobility which in this case are provided by the defects present in $ZnSnO_3$. Nonvolatile behavior and high retention time shown by our devices is due to the large energy barrier offered by the PVOH polymer which restricts the flow of charge carriers back to their original energy states even after the removal of external voltage supply. In order to bring the device back to its

original resistive state i.e. HRS, voltage of opposite polarity must be applied that would cause de-trapping of charge carriers hence resulting in rupturing of conduction path.

Furthermore optimizing the concentration of both PVOH and $ZnSnO_3$ nanocubes will also have a definite effect on the properties of our device that is yet to be optimized. However the possible effects of change in concentration can be assumed by the previously reported work which state that by using only PVOH as the active layer sandwiched between two metal electrodes, no substantial hysteresis or difference in current value was observed [95–97]. Introducing the $ZnSnO_3$ nanocubes in the active layer of PVOH will introduce new energy levels known as trap states. Increasing the concentration of $ZnSnO_3$ nanocubes will increase the conductivity of device when their concentration will exceed the limit known as percolation threshold. It will increase the overall mobility of charge carriers. This will reduce the threshold voltage value which is possibly due to the decrease in the distance between the isolated $ZnSnO_3$ nanocubes assisting in effective charge carrier hopping [96]. However excessive $ZnSnO_3$ leads to an aggregation of the PVOH matrix and degradation of memory properties. When the concentration of $ZnSnO_3$ nanocubes will be increased far beyond the percolation threshold, the PVOH- $ZnSnO_3$ composite is expected to show no resistive switching behavior due to the formation of a permanent conductive pathway between two electrodes [86]. Presumably due to excessive loading of $ZnSnO_3$ its nanocubes can possibly come in direct contact with the electrode. Moreover, choice of the electrode material is very critical in the operation of a memory device as it determines the height of the energy barrier for the injected electrons from electrode to the functional thin film. It is a fact that lower the value of work function, lower will be the energy barrier heights, resulting in a large charge carrier flow from metal contacts into active thin film. Ag metal has been chosen as the top and bottom electrode owing to its lower work function value (4.26 eV) as compared to other metal electrodes like Pt (5.7 eV), Au (5.4 eV) and tungsten (5.1 eV) [98]. The choice of bottom and top electrodes along with

the composition of PVOH-$ZnSnO_3$ nanocomposite is yet to be optimized as a future study that will surely further enhance the performance of this hybrid nonvolatile memory device.

In summary, adding $ZnSnO_3$ into PVOH increases the mobility of charge carriers resulting in a higher conductivity of thin film. A conduction path is formed within the hybrid active layer from one electrode to the other. Charge transfer takes place within the traps provided by the $ZnSnO_3$ nanocubes under the influence of externally applied electric field. When the external power source is turned off, the insulating capping of PVOH on the nanocubes does not allow the electrons to move back to their original energy states with lower conductivity hence restricting them in the trapped states. PVOH plays a vital role in the non-volatile memory behavior and high retention time of our device. The HRS value is also increased due to high dielectric constant of PVOH that increase the difference between high and low conductivity currents resulting in an increase of off/on ratio of our device as compared to the already reported memory device based on only $ZnSnO_3$ nanocubes as the active layer [25].

The nonvolatile memory was further characterized mechanically against several bending cycles to find its application as a flexible resistive switch in electronic devices. The crossbar array was tested in the wide bending range of 50 mm to 4 mm diameter. No significant change in the repeatability of HRS or LRS was observed till the bending diameter of 5 mm. However after that the device showed an open circuit as illustrated in Fig. 3.11 (a).

Typical logarithmic I-V curve at different bending diameters is presented in Fig. 3.11 (b) showing very little deviation from each other. PVOH-$ZnSnO_3$ based memory device displayed very high mechanical robustness of 1500 bending cycles at a bending diameter of 15 mm as illustrated in Fig. 3.11 (c). Typical logarithmic I-V curve were plotted at different stages of bending cycles that resulted in remarkable repeatability as shown in Fig. 3.11 (d). All the mechanical characterizations were carried out by using an in-house built bending machine. The above results suggest that the prepared memory device is highly reliable electrically and

remarkably stable mechanically, making it extremely useful for applications in flexible electronics such as bendable, wearable and foldable devices.oS_2 nanoflakes ink was prepared by exfoliating the MoS_2 multi flakes by aqueous exfoliation method.

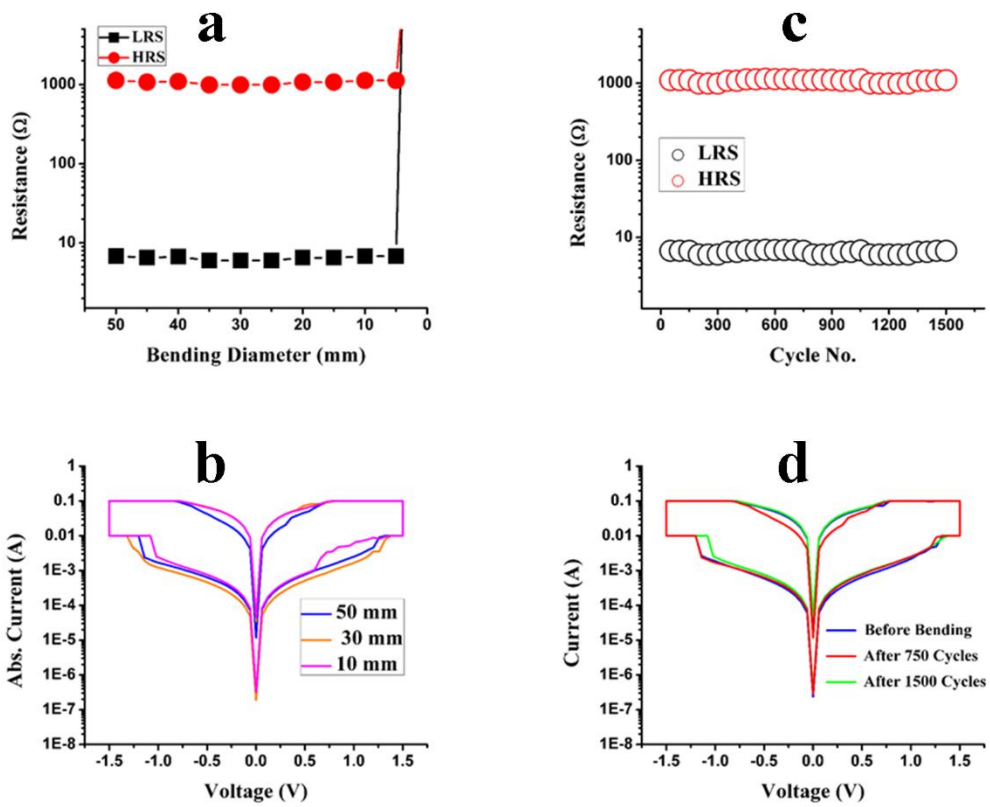

Fig. 3.11. Bendability measurements by using the in-house prepared bending machine illustrating the remarkable flexible properties of as prepared resistive switching device a) Endurance plot clearly showing very less deviation in HRS and LRS with changing values of bending diameters in the range of 50 mm to 4 mm. The device behaved like an open circuit at a bending diameter of 4 mm. b) Typical semi-logarithmic I-V curve at three deferent values of bending diameters c) Endurance curve showing HRS and LRS values for 1500 bending cycles at a fixed diameter value of 15 mm d) Typical semi-logarithmic I-V curves before bending and after bending showing excellent repeatability of bipolar resistive switching.

MoS_2 pristine powder was ground in ethanol for 1 hour in a mortar followed by heating at 100 ℃ for 1 hour to evaporate the solvent. Furthermore, ground MoS_2 was dispersed in 50/50 % solution of ethanol and deionized water for probe sonication for 1 hour as grinding and sonication both are effective in exfoliation of MoS_2 flakes. Finally, centrifugation at 4000 rpm was carried out for 30 min to remove the larger flakes and partially exfoliated crystallites. The supernatant was collected and placed on magnetic stirrer for overnight.

3.3. Memristor based on $ZnSnO_3$ nanocubes interspersed ZnO nanowires

Here, the resistive switching effect in the nanocomposite of zinc oxide nanowires (ZnO NWs) and zinc stannate nanocubes ($ZnSnO_3$ NCs) has been explored. Device has been fabricated on a flexible substrate (PET) on which highly conductive (0.3 Ω-cm) patterns of silver (Ag) were deposited as bottom electrodes by reverse offset printing technique. The fabricated device exhibited characteristics of bipolar, rewritable, and nonvolatile resistive switching memory with off/on ratio of 5.8 × 102 and retention time of 104 s at a small operating voltage (1.2 V). The obtained electrical results of Ag-ZnO/$ZnSnO_3$-Ag memory device were remarkable with appreciable repeatability. The significantly stable, highly durable and promising results of ZnO NWs-$ZnSnO_3$ NCs heterostructure makes this semi conductive nanocomposite a potential candidate for future flexible memory devices.

3.3.1 Device Fabrication

Bottom electrodes of the proposed resistive switching device in this work were fabricated by reverse offset printing system, by using this system high resolution micro pattern electrodes can be achieved. The mechanism and fabrication details of reverse offset printing technique can be found in these earlier reported studies [78,99,100]. A brief description of the fabrication details include, first of all the designing of an intaglio-patterned cliché of the required patterns on a silicon wafer by photolithography. High viscosity Ag NPs ink was spin coated on a glass substrate and then it was placed under the steel cylinder wrapped up by polydimethylsiloxane (PDMS) blanket in reverse offset printing system. As the PDMS blanket roller moved over the glass substrate, the Ag NPs ink was transferred from glass substrate to PDMS blanket roller and a semi-dried thin layer of Ag NPS is formed over PDMS blanket. Subsequently, the PDMS blanket roller covered by the Ag NPs ink was moved over the intaglio-patterned cliché with uniform pressure of 3 KgF and speed of 3 mm/s. The engraved patterns on cliché were completely transferred onto the PDMs blanket roller that was again rolled over the PET

substrate with same pressure and speed. Finally, very fine electrodes were transferred on PET substrate due to the low surface energy of the PDMS blanket i.e. 18.6 mN/m having the 50 µm width and high resistivity of 0.2 Ω-cm. Fig. 3.12 shows the optical image of originally printed cliché design consist of ten memory cells on the PET substrate by reverse offset printing, whereas optical microscopic images show that patterns are clearly unbroken and highly uniform.

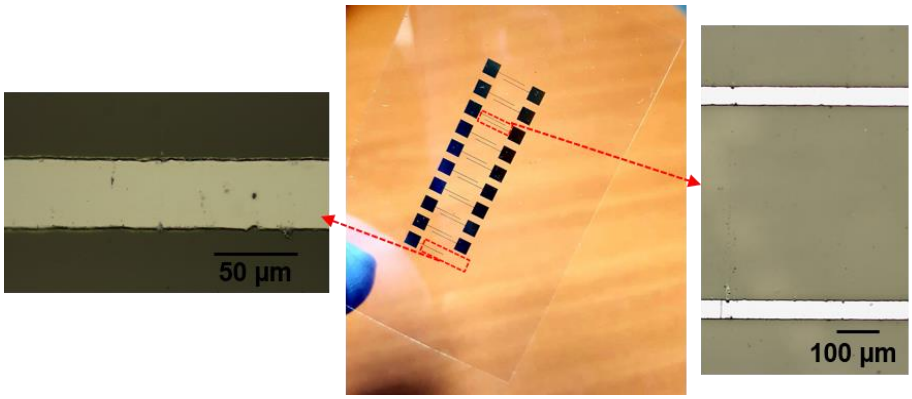

Fig. 3.12. Originally printed cliché design consist of ten memory cells on PET (center), with optical microscopic images of a single memory cell having width of 50 µm (left) and two consecutive memory cells (right).

$ZnSnO_3$ NCs were sprayed onto as grown ZnO NWs through EHD atomization that is a well-established thin film deposition technique in printed electronics [69,101–104]. It is non-contact, vacuum based; a semi-wet processing technique used to deposit a large number of nanomaterials including organic polymers, inorganic nanoparticles and their composites through the formation of spray. The phenomenon related to the spray formation involves the flow of nanoparticles ink from syringe pump to nozzle under the influence of applied potential. The target substrate is placed on a moving stage which works as a ground electrode also; on applying the electric field, the ink forms a cone jet and sprayed onto the substrate in the form of nano droplets. A uniform and semi-wet thin film is deposited when the stable cone jet is obtained and that can be obtained by optimizing the different para meters like applied voltage, stand-off distance, nozzle size and flow rate. Stable cone jet was achieved between 4.2 - 4.9 kV at 20 mm stand-off distance at a flow rate of 200 µl/h by using 310 µm diameter nozzle.

$ZnSnO_3$ NC were randomly oriented onto ZnO NWs and some of them infiltrated into the pores of ZnO NWs as has been depicted in schematic Fig. 3.13.

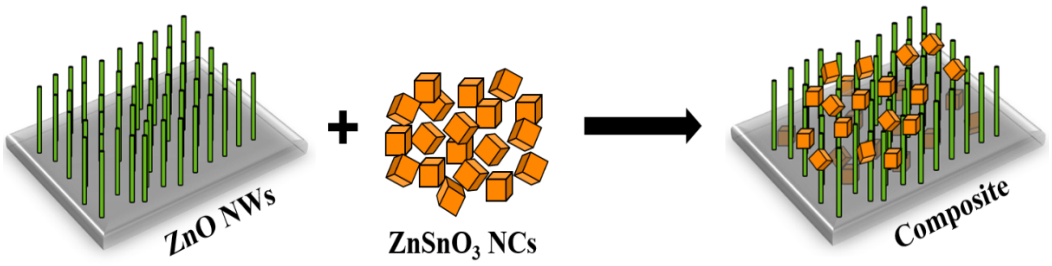

Fig. 3.13. Schematic diagram of the as grown ZnO NWs on flexible substrate and their heterostructure composite with $ZnSnO_3$ NCs, after EHDA spray NCs were supposed to be randomly oriented onto ZnO NWS while some of them infiltrated into their pores.

A very fine and highly uniform top electrode was fabricated by EHD patterning using high viscosity Ag ink. The difference between EHD pattering and EHD atomization is that the former is used for micro-patterning of conductive inks by reducing the distance between the target substrate and nozzle while EHDA is used for thin film deposition through spray.[80] It is a non-contact method and does not damage the thin film while contact methods like reverse offset printing or screen printing can damage the thin film. Experimental details include the filling of Ag ink in a syringe and connecting it to syringe pump through a Teflon tube; flowing the ink at the rate of 80 µl/h to the metallic nozzle of 30 µm orifice caused the ejection of micro drops of ink. On applying the voltage to the metallic nozzle, a meniscus is formed and by increasing the voltage up to 4.0 kV, a stable meniscus is formed resulting the continuous ejection of ink. The distance between the nozzle and substrate was kept 5 µm, a single straight pattern of ≈ 50 µm width and ≈ 25 mm length was continuously deposited on the target substrate without contacting the thin film having very low resistivity of 0.4 Ω cm^{-1}. The optical image of the as deposited top Ag electrode can be seen in Fig. 3.14.

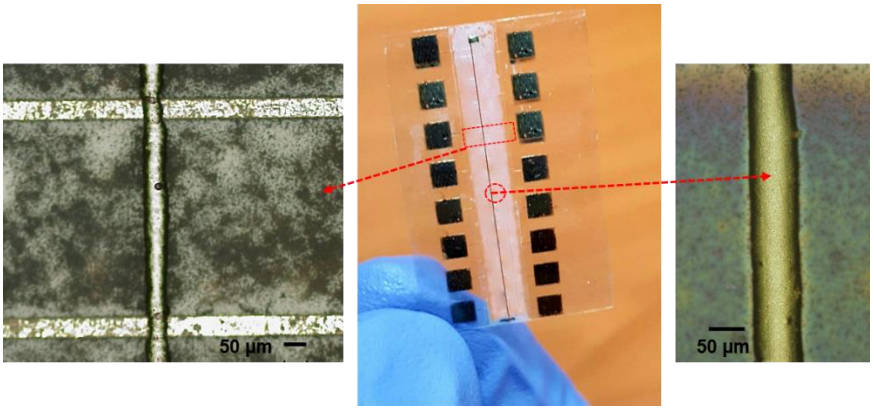

Fig.3. 14. Optical image of the real memory device showing the top electrode on active layers patterned by EHD patterning (Center), optical microscopic images of the top electrode (right) and top electrode crossing above the bottom electrodes (left).

3.3.2 Device characterization and results

DC voltage was applied across the two terminals of the developed ZnO-$ZnSnO_3$ based memory device. At first, electroforming was performed to facilitate the formation of a conduction path between two electrodes and to bring stability in the electrical characteristics of the device as shown in Fig. 3.15 (a). This process is also known as soft breakdown. The current compliance value was optimized to 700 µA to protect the device from sudden breakdown due to Joule heating effect. Afterwards, a double voltage sweep from -2 to +2 volts was applied across the two terminals to evaluate the electrical characteristics of the developed device. The obtained I-V curve shows the behavior of a typical bipolar switching device as illustrated in Fig. 3.15 (b). It can be seen from the electrical characteristic curves of Ag/ZnO-$ZnSnO_3$/Ag that a symmetric bipolar resistive switching is observed on applying cyclic voltage sweep across the two terminals owing to the similar metal electrodes and heterostructure potential barriers. The device was originally in HRS and as the magnitude of positive bias DC voltage increased, it switched to LRS. This transition from HRS to LRS at a threshold voltage (V_{th}) of +1.7 V is termed as SET or writing process at which data can be stored in a memory device. Once a bit is stored in a memory cell, the magnitude of applied positive bias is decreased to zero and a negative bias is applied to switch the device back to its original resistive state of HRS.

Switching from LRS to HRS takes place at a V_{th} of -1.7 V as seen in the Fig. 3.15 (b). This is known as erasing or RESET process at which data is removed from the memory device. The Ag/ZnO-$ZnSnO_3$/Ag based memory device displayed a highly symmetric behavior mainly due to the selection of two similar metal electrodes with equal work function values. The trend of switching ratio with increasing magnitude of applied voltage is illustrated in Fig. 3.15 (c). The switching ratio increases with increasing voltage and remains almost stable in the range of 0.7-0.9 V (memory window) after which it begins to decrease sharply. Moreover, the distribution of bistable resistive states (HRS and LRS) and V_{th} (V_{SET} and V_{RESET}) is shown in the form of their cumulative probability plots as illustrated by Fig. 3.15 (d) and 3.15 (e) respectively.

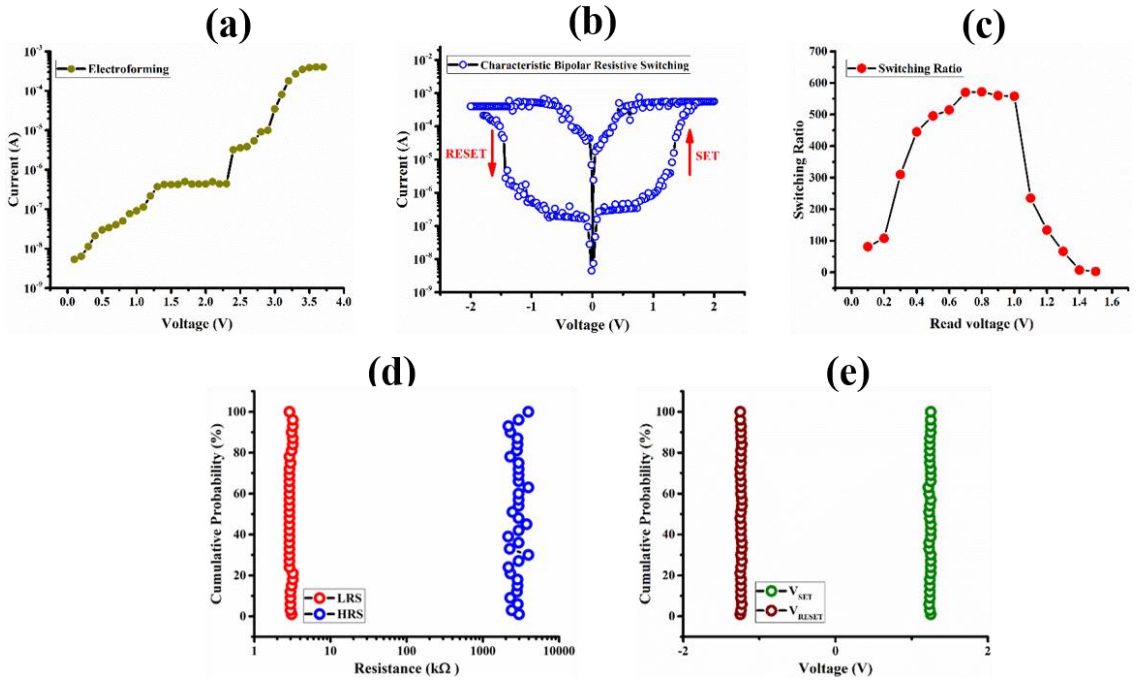

Fig. 3.15. Electrical characterization of as fabricated memory device (a) Electroforming step before applying double voltage sweep (b) Characteristic bipolar I-V curve (c) Trend of switching ratio with increasing value of read voltage (d) Cumulative probability illustrating the distribution of bistable resistive states (e) Cumulative probability plot illustrating the distribution of Vth (Vset and Vreset).

These plots display the high stability and repeatability of our fabricated memory device ensuring its reliable operation. Moreover, electrical endurance and retention time of stored data are two extremely important electrical characteristics of any memory device therefore we measured both these parameters whose results are presented in Fig. 3.16. Characteristic I-V

curves for 1st, 500th and 1000th applied biased voltage cycles are presented in Fig. 3.16 (a). This can be clearly seen that all the three curves are overlapping each other without any substantial deviation verifying high endurance of our proposed memory device.

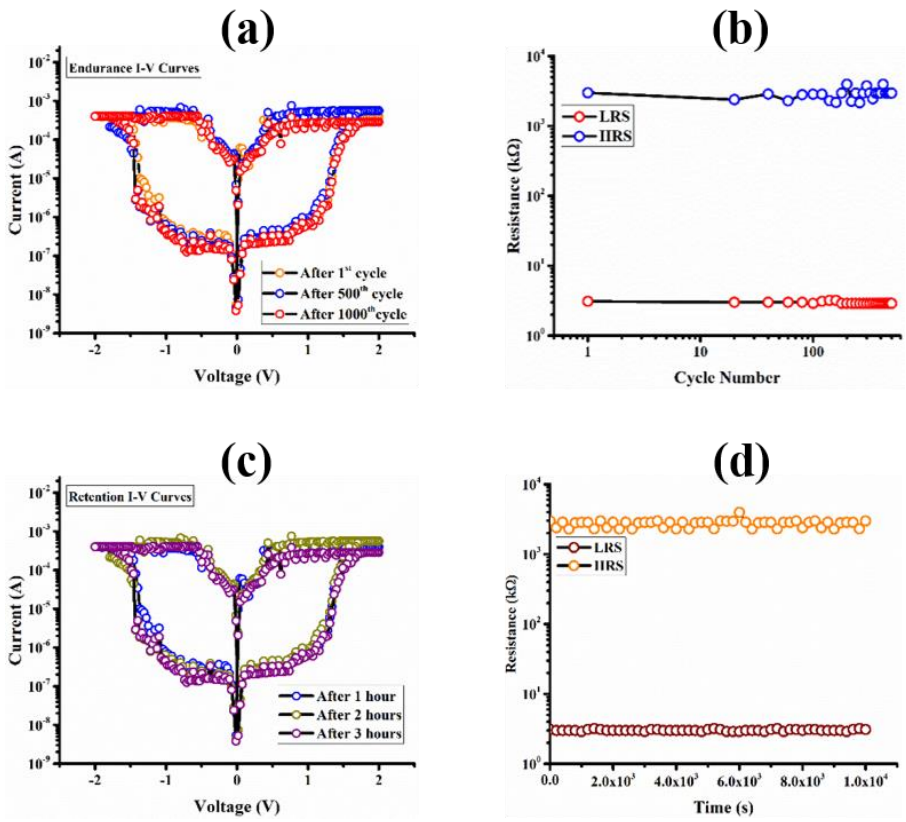

Fig. 3.16. (a) Illustration of high stability against several voltage cycles by displaying I-V curves for 1st, 500th and 1000th cycle (b) Endurance of bistable resistive states for 1000 operating cycles (c) Retention I-V curves of as fabricated memory device for 1h, 2h and 3h respectively (d) High stability of bistable resistive states for a long retention time.

Moreover the electrical endurance of bistable resistive states for 1000 voltage sweeps is also presented in Fig. 3.16 (b). Retention of a memory device is its ability to hold its stored data over a long period of time. We measured the I-V characteristic curves of our device for 3 h and the obtained results are shown in Fig. 3.16 (c). The high stability of bistable resistive states for ~ 10^4 s shows that this device can store data for a long time without any degradation in its electrical properties as illustrated in Fig. 3.16 (d).

Although the working principal of resistive switching in various polymers and inorganic semiconductors has already been proposed but the memory behavior and charge transfer based

on a composite of ZnO nanowires and $ZnSnO_3$ nanocubes is rather different from the classical theory. It is believed that resistive switching in our device is mainly due to the charge injection from the metal electrode into the interface of nanowires and nanocubes that can be explained with the help of a difference in the work function values of metal and semi conductive nanocomposite.

A II-type band alignment would have been formed between ZnO nanowires and $ZnSnO_3$ nanocubes owing to the magnitude of their electron affinity and high bandgap respectively. Electrons in the interior of ZnO nanowires might diffuse onto the interface states resulting in bending of the conduction band and valence band in upward direction. It will form a lower conductivity depletion layer near the interface of nanocomposite. Therefore, the flow of charge carriers is restricted by the formation of this potential barrier preventing them to move freely at the interface of nanoparticles unless an external bias is applied. An Ohmic contact is formed between Ag electrode and ZnO/$ZnSnO_3$ heterostructure because electron affinity of both $ZnSnO_3$ (4.5 eV) and ZnO (4.35 eV) semiconductors is higher than the work function of Ag (4.26 eV). At reverse bias, the direction of diffused electrons is same as that of applied external electric field. At low magnitude of externally applied electric field, only a few charge carriers are able to cross the hetero interface and the device operates in HRS due to less number of freely flowing electrons. As the magnitude of applied bias increases, majority of charge carriers begin to flow from the electrode into the interface states of heterostructure where they are trapped by $ZnSnO_3$ nanocubes due to their quantum confinement effect and the interior of ZnO nanowires. Due to this sudden increase in the electronic drift with increasing voltage, the depletion layer width decreases that consequently diminishes the effective potential barrier height for charge carriers to cross the heterostructure and the energy band moves in downward direction [105]. The downward shift of conduction and valence bands results in the increase of accessible trap sites for the charge carriers. Once the effective height of potential barrier is

lowered for freely flowing charge carriers, it become very easy for them to tunnel through the reduced potential barrier. With further increasing voltage, the potential barrier is finally demolished and effectively injected electrons from the metal electrode can freely flow through the conduction band of semi conductive heterostructure until all traps are occupied [106]. This mutation of potential barrier brings the device in LRS where data can be easily stored or written known as the SET process. Both $ZnSnO_3$ nanocubes and ZnO nanowires contribute in the conductivity of memory device. When the bias of applied voltage is reversed, the trapped electrons from the interior of ZnO nanowires and $ZnSnO_3$ nanocubes gain enough energy to return into the Ag electrode. This effective de-trapping of carrier sites results in turning the device back to its original resistive state of HRS. As a result, width of potential barrier will again begin to increase due to the rising of energy band in upward direction. This clearly exhibits that the stored data can easily be removed by reversing the polarity of applied voltage making it a rewritable memory device.

3.4. Humidity sensor based on 2D MoS_2 flakes and PEDOT:PSS array

Role of materials properties in sensing devices fabrication is of eminent importance. For resistive type gas or humidity sensors, the basic criteria of the materials include high surface area to volume ratio, ionic conductivity, quick adsorption/desorption characteristics, and large absolute change in electrical parameters based on change in the analyte concentration. Device structure and configuration also plays a vital role in defining sensors performance. In this work, 2D MoS_2 flakes have been employed for humidity sensing devices based on their morphological and electrical characteristics. The sensors have been used in series with PEDOT:PSS based device to improve the sensitivity, detection range, and curve linearity. Both materials have different humidity sensing mechanisms and ranges of detection. Their effect is combined to achieve a highly sensitive and near-linear humidity sensor with excellent response time and sensitivity.

3.4.1 Device Fabrication

Bottom electrodes for humidity sensor were fabricated on a glass substrate using reverse offset printing system, the details of which can be found in section 3.2.1. Thin film of exfoliated MoS_2 flakes was deposited through EHD atomization that is a well-established thin film deposition technique in printed electronics [69,101–104]. It is non-contact, vacuum based; a semi-wet processing technique used to deposit a large number of nanomaterials including organic polymers, inorganic nanoparticles and their composites through the formation of spray. The phenomenon related to the spray formation involves the flow of nanoparticles ink from syringe pump to nozzle under the influence of applied potential. The target substrate is placed on a moving stage which works as a ground electrode also; on applying the electric field, the ink forms a cone jet and sprayed onto the substrate in the form of nano droplets. A uniform and semi-wet thin film is deposited when the stable cone jet is obtained and that can be obtained by optimizing the different para meters like applied voltage, stand-off distance, nozzle size and flow rate. Stable cone jet was achieved between 4.2 - 4.9 kV at 20 mm stand-off distance at a flow rate of 200 µl/h by using 310 µm diameter nozzle. MoS_2 nanoflakes were randomly oriented onto IDTs. The schematic of the complete device fabrication process has been presented in Fig. 3.17.

The fabrication of PEDOT: PSS thin films through SAW-EHDA was performed under a set of carefully optimized processing parameters like nozzle diameter, flow rate, standoff distance, applied voltage, applied frequency, deposition time and power. It is evident that most of the experimental parameters that have been used for the deposition of thin film are quite similar. The intention behind the implemented approach of utilizing same parameters, as many as possible, was to effectively investigate and better understand the true potential of this unique technology to develop wide variety of thin films. One of the main parameter i.e. the applied

voltage is mainly dependent on the properties of the deposited material. The applied voltage and power for deposition of PEDOT:PSS thin film were 3.35kV and 5W respectively.

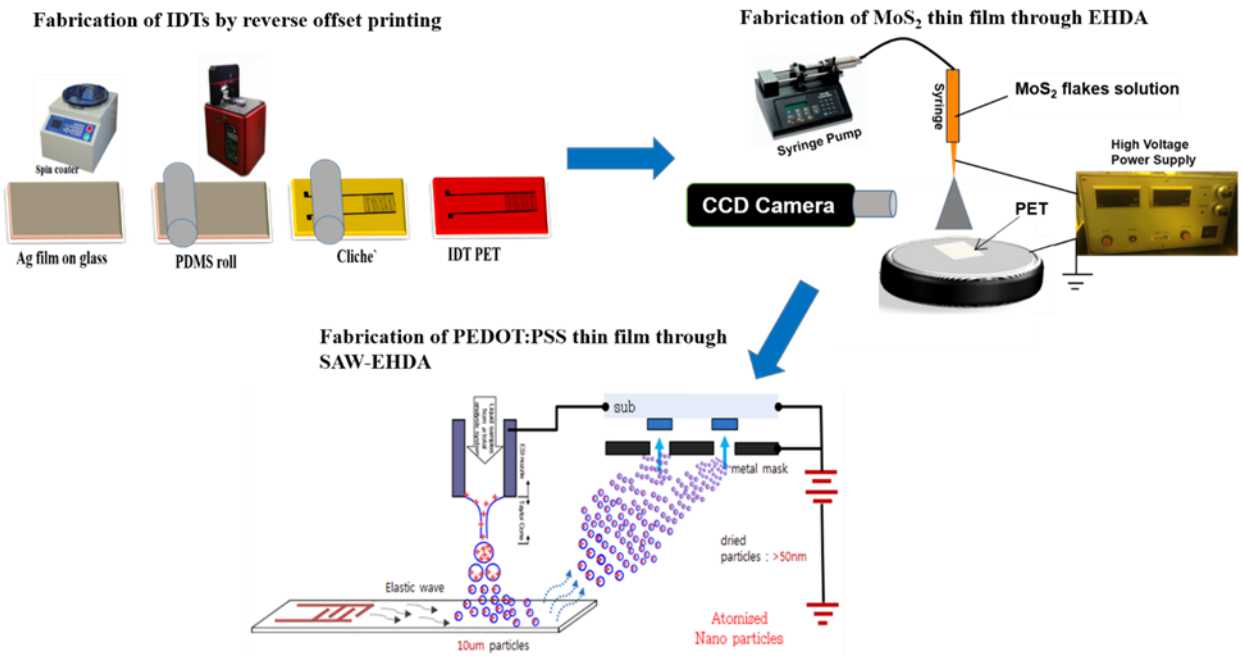

Fig. 3.17. Step by step fabrication process diagram; first IDTs were fabricated by using reverse offset printing system, second thin film of MoS_2 nanoflakes was fabricated through EHDA and in last PEDO:PSS thin film was deposited by SAW-EHDA.

3.4.2 Device characterization and results

The electrical response of the sensors towards change in relative humidity was recorded using an in-house built controlled environmental chamber. The humidity level inside the chamber was regulated using PID based feedback controller. Compressed dry air was used for de-humidification while water vapors from a desktop humidifier were added to the dry air stream to increase the humidity of the chamber. A commercial MEMS based high accuracy temperature and humidity sensor HTU-21D was used as the reference and feedback. The impedance data of the sensor from the LCR meter and the reference humidity sensor values are continuously plotted and logged in to a computer connected through USB communication interface. A 555-timer based square wave oscillator circuit was then designed to convert the

response of the sensors in terms of frequency for a more user friendly interface. The detailed schematic of the characterization setup is shown in **오류! 참조 원본을 찾을 수 없습니다.**.

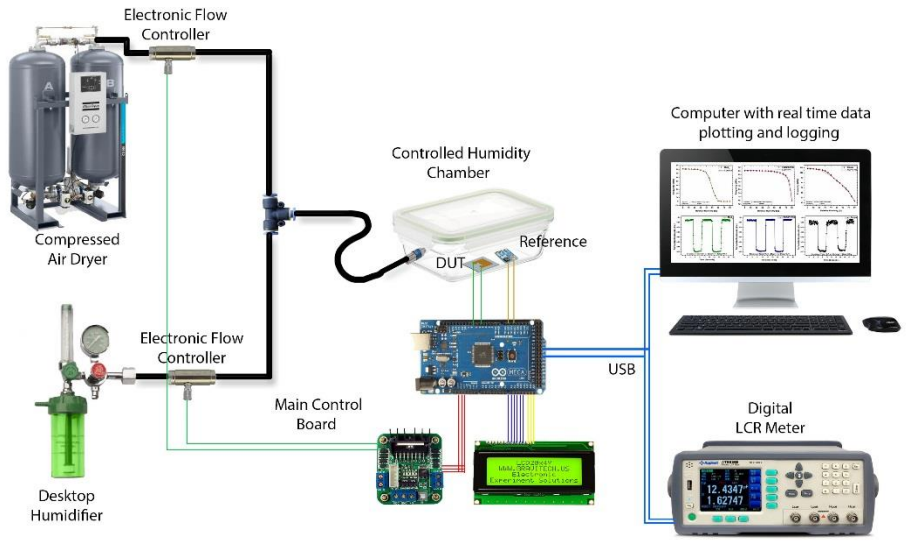

Fig. 3.18. Characterization setup used for the measurement of sensors' electrical response against relative humidity change

Three sensors were fabricated based on the active layers of PEDOT:PSS, MoS_2, and a series combination of both. The impedance of the all the sensors was recorded with respect to change in relative humidity and the test frequency was maintained at 1 kHz. The relative humidity of the controlled environmental chamber was slowly increased from 0% RH to 80% RH and the corresponding impedance values of the sensors were recorded. The results of the impedance response are presented in Fig. 3.19.

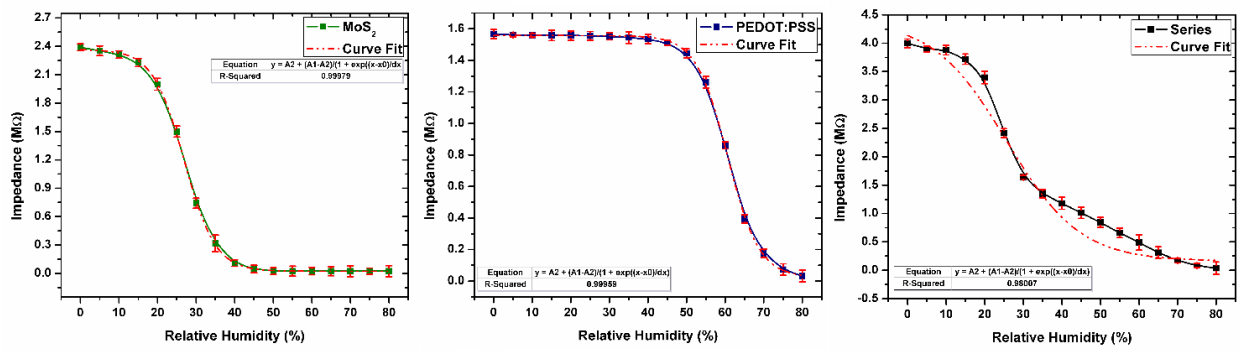

Fig. 3.19. Impedance response of sensors with active layers of (a) MoS_2, (b) PEDOT:PSS, and (c) Series combination of the two showing decrease in impedance with increasing relative humidity.

The results show that the impedance of the sensors decrease with increasing humidity levels for all three types. In case of MoS_2 based sensor as presented in Fig. 3.19 (a), the relative decrease in the magnitude of impedance is very high for the initial half of the humidity range while it slowly gets saturated while entering the second half. The decrease in impedance for the MoS_2 based sensor is mainly due to the resistance drop of the thin film as soon as the humidity of the system is increased. Water vapors are readily adsorbed by the highly porous surface of the MoS_2 thin film and result in an ionic plus proton hopping based current flow through the few layered sheets of the 2D MoS_2 flakes. This quickly reduces the sheet resistance and the impedance of the sensor drops. Once the overall impedance of the sensor reduces from around 2.4 MΩ to several KΩ, the response gets saturated and no visible change is observable upon further increasing the humidity. The major part in case of MoS_2 for impedance change is played by the ionic current while a minor part is also played by the increase in capacitance of the thin film when the water molecules are physisorbed by the active layer. This increases the dielectric constant of the film, thus increasing the capacitance in return. The graphical illustration of the sensing mechanism of MoS_2 based sensor is presented in Fig. 3.20 (a). The impedance of the sensor can be expressed by equation 1.

$$Z = {}^{1}/_{2\pi fC} + R_s \qquad (1)$$

Here, “Z” is the impedance, “f” is the test frequency, and “C” is the capacitance. It is clear that decrease in the series resistance or increase in capacitance results in decrease of impedance. In case of PEDOT:PSS based sensor as presented in Fig. 3.19 (b), there is a relatively small change in impedance for the first half of humidity range while the impedance quickly drops while entering the second half. PEDOT:PSS is a conductive polymer and its resistance also drops with increase in relative humidity but the change is very small because the water molecules do not directly get involved in generating ionic current but only result in facilitating the flow of electronic current by providing better paths to the already flowing current as shown in Fig. 3.20 (b). This is why the relative change in the magnitude of impedance is very small for the lower humidity levels. At higher levels, the effect of change in capacitance of the thin film through physisorbed water molecules dominates in changing the impedance of the sensors. As the magnitude of impedance is still near 1.4 MΩ for PEDOT:PSS at the start of the second half, there is enough room for further decrease in impedance for the higher half of relative humidity.

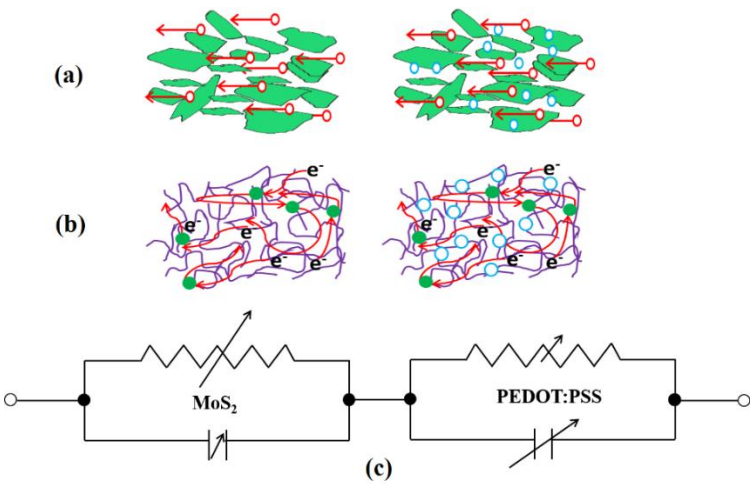

Fig. 3.20. Sensing mechanism of the sensors with active layers of (a) MoS_2, (b) PEDOT:PSS, and (c) simplified equivalent circuit of the series combination of the two sensors.

We can see that the behavior of the two fabricated sensors is opposite in terms of detection range. One sensor is highly sensitive for the humidity range from 0% RH to 40% RH while the

second sensor has major response in the region from 40% RH to 80% RH. To get a highly sensitive sensor for the full range of humidity, the response of these two sensors has to be ideally merged. To achieve this, we propose a novel schematic for the humidity sensor with more than one sensing elements having different active materials and responses. After mathematically analyzing the individual curves, we fabricated a dual cell sensor with the two sensors effectively connected as two series elements. The simplified equivalent circuit of the resulting device is presented in Fig. 3.20 (c). The total effective impedance of the two sensors will be the sum of the impedances of the two individual sensors. In ideal condition, MoS_2 based sensor will play its role for the first half in humidity detection and PEDOT:PSS based portion will play its role for the second half. The results presented in Fig. 3.19 (c) clearly show high sensitivity of the series sensor for the full range of humidity detection. The effect of both individual portions is clearly visible in the resulting impedance curve. The overall impedance changes from 4 MΩ to 10 KΩ from 0% RH to 80% RH. This give us an ultrahigh sensitivity of 50 KΩ/%RH that is higher than most of the reported sensors in literature with a wide detection range. A detailed comparison of different types of humidity sensors is presented in Table 3.3.

Table 3.3. Comparison literature survey table

Materials	Material Category	Device Structure	Sensing Mechanism	Detection Range	Sensitivity	Response Time	Recovery Time	Percentage Error	Curve Shape	Reference
Polyaniline	Conductive Polymer	Chemristor	Resistive	47-87% RH	(12.5 kΩ/sq.)/%RH	27 s	60 s	5%	Linear	[107]
Polyaniline	Conductive Polymer	IDT Single Layer	Resistive	20-85% RH	0.3 kΩ/%RH	5 s	Not Measured	Not Measured	Exponential decay	[108]
Graphene Oxide	2D Conductive material	IDT Single Layer	Resistive	35-75% RH	49 nS/%RH	0.1 s	0.09 s	Not Measured	Linear	[109]
Polyvinyl Alcohol	Insulating Polymer	Optical fiber grating	Optical	30-95% RH	0.54 nW/%RH	2 s	Not Measured	1 %	Almost Linear	[110]
Onion Membrane	Bio Material	IDT Single Layer	Impedance Based	0-80% RH	Not Measured	1 s	11 s	5 %	Exponential Decay	[111]
Zinc Oxide	Inorganic Material	Chemristor	Resistive	5-85% RH	42.678%	3 s	12 s	Not Measured	Non-linear decay	[112]
Titanium Dioxide	Ceramic Nanoparticles	IDT Single Layer	Resistive	30-90% RH	3.6 mV/%RH	58 s	65 s	Not Measured	Almost linear	[113]
PDEB	Organic Polymer	IDT Single Layer	Impedance Based	15-92% RH	120 kΩ/%RH	Not Measured	Not Measured	3%	Exponential Decay	[114]
PPA, PDEB, & NaPSS	Substituted Polyacetylenes	IDT bi-layer	Impedance Based	10-90% RH	100 kΩ/%RH	18 s	Not Measured	Not Measured	Non-linear decay	[115]
Graphene	2D Materials	Bi-layered Chemristor	Resistive	35-95% RH	15 %	Not Measured	Not Measured	Not Measured	Almost Linear	[116]
Graphene Oxide, Silicon	2D Material, Inorganic Material	Bi-Layered Bridge	Resistive	10-100% RH	27 µV/%RH	19 s	10 s	Not Measured	Almost Linear	[117]

Graphene, PSS	2D Material, Conductive Polymer	Bi-Layered Chemristor	Impedance Based	30-95% RH	10 kΩ/%RH	3 s	22 s	Not Measured	Almost Linear	[118]
QC-P4VP, RGO	Polyelectrolyte, 2D Materials	Bi-Layered on IDT	Impedance Based	10-90% RH	1 kΩ/%RH	21 s	78 s	Not Measured	Non Linear Decay	[119]
Zn), CuTCNQ	Organic/Inorganic junction	Diode heterojunction	I-V curves	0-75% RH	Not Measured	60 s	30 min	Not Measured	Linear	[120]
Graphene Oxide, PNaPSS	Composites	Dual plate capacitor	Capacitive charge pump	0-80% RH	35 µV/%RH	Not Measured	Not Measured	Not Measured	Almost Linear	[121]
LiCl, HPPMs	Composite porous polymer, Salt	Double layered capacitor	Impedance Based	10-90% RH	Not Measured	2 s	32 s	Not Measured	Linear	[122]
Ce-doped ZnO	Inorganic Materials	IDT Single Layered	Impedance Based	11-95% RH	1 MΩ/%RH	13 s	17 s	Not Measured	Non-Linear	[123]
TiO_2, LiCl	Inorganic Materials	Adsorption in thin film	SAW Based	25-65% RH	Not Measured	0.75 s	1 s	Not Measured	Non Linear Decay	[124]
PEDOT:PSS/ MoS_2 Flakes	*Conductive Polymer, 2D Material*	*Dual IDT's in Series*	*Impedance Based*	*0-80% RH*	*50 kΩ/%RH, 850 Hz/%RH*	*0.5 s*	*0.8 s*	*2 %*	*Non-Linear*	*Current Work*

To make a sensor suitable for commercialization, its output response should be in terms of a parameter that is easy for read out circuits available to the end user. For this purpose, we have converted the output of our sensors into change in frequency using an oscillator circuit shown in Fig. 3.22. The results of the frequency based output response are presented in Fig. 3.21.

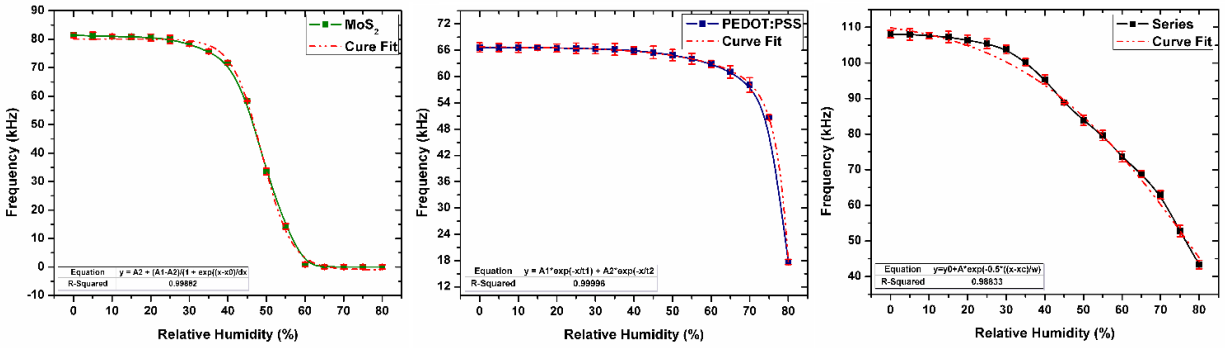

Fig. 3.21. Frequency response of sensors with active layers of (a) MoS_2, (b) PEDOT:PSS, and (c) Series combination of the two showing drop in frequency output with increase in relative humidity.

We can observe here that the magnitude of frequency decreases with increasing humidity for all three types of the sensors. The behavior of change in magnitude and the curve shapes have small differences when compared to the impedance response of the sensors. That can be explained using the frequency response formula of the circuit presented in equation 2.

$$f = \left(\frac{1.49}{(R_A + 2R_B)C}\right) e^{-R/0.53} \qquad (2)$$

R_A and R_B are two fixed resistances in the circuit, C represents the capacitance R represents the resistance of the equivalent circuit of the sensor as presented in Fig. 3.21 (a). The equation is the modified form of a simple 555 timer based oscillator including the factor of a parallel resistance in the equivalent circuit of the sensing device. The effect of resistance is exponentially non-linear on the frequency and as the resistance decreases, the frequency also decreases. Due to the addition of a non-linearity in the output, the frequency response is not exactly the same as that of impedance response but the major theme is same, that is, increasing humidity decreases the frequency. It can also be observed in Fig. 3.21(c) that the curve shape of the frequency response is even closer to linearity that is better for the end user applications.

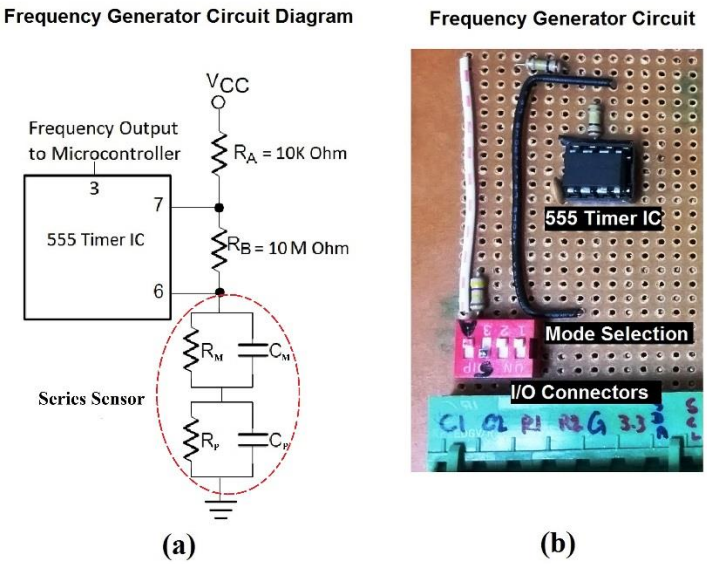

Fig. 3.22. Frequency conversion circuit to translate the output of the sensors in to frequency (a) circuit diagram of the designed oscillator and (b) actual photograph of the fabricated circuit.

The response and recovery times of the sensors was then recorded for all three types. One stream of compressed dry air and a second stream of highly humid air were used to get the response time curves. The electronic valves were completely opened and closed with pulses to expose the sensing area directly to the incoming streams. The impedance data of the sensors was logged in plotted in a computer in real time. The results of the response time recording are presented in Fig. 3.23. The response and recovery times calculated for the MoS_2 based sensor

were 0.4 s and 0.6 s respectively while they were 0.2 s and 0.3 s for the PEDOT:PSS based sensor. The series sensor gave response time of 0.5 s and recovery time of 0.8 s. The results show excellent performance characteristics of the series based sensor that are ideal for real life applications requiring high sensitivity, wide detection range, and fast response and recovery times. The fabricated sensor system is capable of sensing relative humidity with ultrahigh sensitivity (50 KΩ/%RH or 800 Hz/%RH) in a wide range of 0% RH to 80% RH. The response and recovery times are also excellent with values of 0.5 s and 0.8 s respectively.

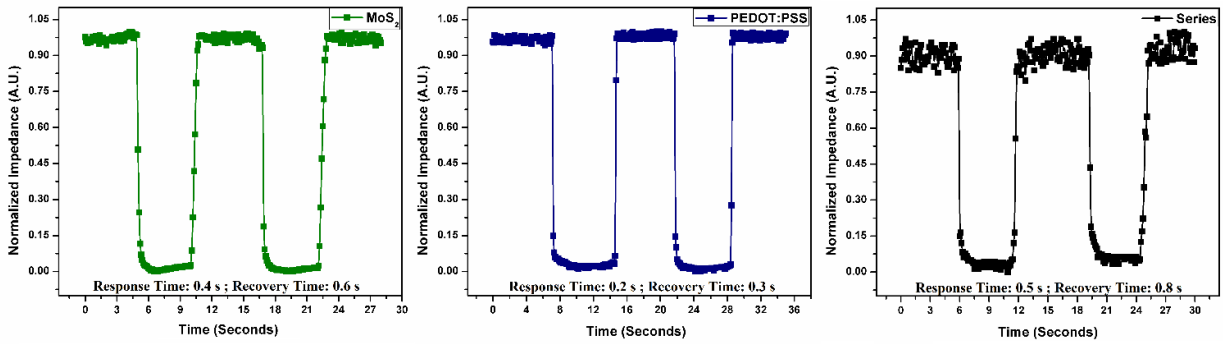

Fig. 3.23. Response and recovery time curves of the sensors with active layers of (a) MoS_2, (b) PEDOT:PSS, and (c) series combination of the two.

The comparison with the most advanced sensors in the literature proves this work to be better than the previous ones in most of the areas. The curve linearity and the range of detection can be further improved in future works using the same approach but employing a multi-sensory array instead of two sensors in series-parallel combinations to achieve the perfect all-purpose humidity sensor.

Chapter-4. Conclusion and Future Work

4.1 Conclusions

This thesis has reported the complete study about the synthesis, characterization, thin film fabrication and applications of nanostructured and nanocomposite materials. The applications included resistive switching devices and humidity sensor fabricated by the printing techniques using nanostructured and nanocomposite materials. Nanostructured low dimensional materials were synthesized and developed including zero-dimensional: MOS_2 QDS, one-dimensional: ZnO NWs, two-dimensional: MoS_2, hBN nanosheets and three-dimensional: $ZnSnO_3$ NCs. Moreover, the nanocomposite of these nanostructured materials were also developed that include $ZnSnO_3$/PMMA, $ZnSnO_3$/PVOH, hBN/PVOH, ZnO/$ZNSnO_3$ and MoS_2-PEDOT:PSS. MoS_2 QDS showed the blue luminescence at 448 nm and their size was less than 10 nm while their concentration was 7 mg/ml that shows the efficiency of the method to synthesized MoS_2 QDs that was based on grinding, mechanical shaking, ultrasonication, and centrifugation using NMP and DCB as solvents.

ZnO NWs were grown by hydrothermal method on flexible substrate with the help of ZnO seed layer. The as grown ZnO NWs were observed highly aligned; average diameter was found to be 100 nm, average length (0.5 µm), and average density ($1\times2\ 10^9\ cm^{-2}$).

Nanosheets of MoS_2 and hBN were exfoliated via liquid exfoliation method to produce solution processable and printable dispersion of layered materials. Nanocomposite of hBN/PVOH was also developed and PVOH worked as dispersant as well to form a stable dispersion exfoliated hBN. The nanocomposite of hBN/PVOH was exploited to use in memory devices that proved to be an appreciable work. The all printed memory device, with the ITO/hBN–PVOH/Ag configuration, exhibited admirable non-volatile and rewritable bipolar resistive switching behavior. Off/on ratio as high as 4.8×10^2 was recorded which is enough to distinguish between HRS and LRS. Significantly high endurance of > 1000 voltage sweeps was recorded at a

reading voltage of 0.26 V. The hybrid nanocomposite of hBN and PVOH displayed excellent durability and mechanical robustness when tested against several bending cycles.

MOS_2 nanosheets were fabricated as thin film in parallel with PEDOT:PSS on a single substrate as two separate humidity sensors but were combined a in a series to fabricate a single humidity sensing device and their response was electronically combined. MoS_2 showed humidity response at low humidity level while PEDOT:PSS at high humidity level that's why these two were combined in a series to obtain a single humidity sensor. The fabricated sensor system is capable of sensing relative humidity with ultrahigh sensitivity (50 KΩ/%RH or 800 Hz/%RH) in a wide range of 0% RH to 80% RH. The response and recovery times are also excellent with values of 0.5 s and 0.8 s respectively.

Highly crystalline $ZnSnO_3$ nanocubes were synthesized via aqueous solution method having average size ≈70 nm and they were further used to develop various nanocomposites including $ZnSnO_3$/PMMA, $ZnSnO_3$/PVOH and ZnO/$ZnSnO_3$. A nonvolatile, rewritable and flexible memory device based on an organic-inorganic hybrid nanocomposite of PVOH-$ZnSnO_3$ was fabricated that showed low operating voltage of 1.5 V, large electrical endurance of 500 voltage sweeps, and long data retention of 36 hour. The nonvolatile and flexible memory device also exhibited tremendous mechanical robustness when tested against 1500 bending cycles.

Another non-volatile memory device was fabricated based on the heterostructure of ZnO NWS and $ZNSnO_3$ NCs. Highly significant ant repeatable results of resistive switching memory were obtained such as off/on ratio of 5.8×10^2, electrical endurance of 1000 voltage cycles and retention time of 10^4 s. Non-significant deviation in the bistable resistive states (HRS, LRS) and threshold voltages (V_{SET}, V_{RESET}) was observed in the obtained cumulative probability plots. Hence, these appreciable results prove the potential of this nonvolatile memory device (Ag/ZnO NWs-$ZnSnO_3$ NCs/Ag) to be used in flexible electronics.

4.2 Future Work

As MoS_2 QDs have shown unique photoluminescence properties when exposed UV light. In future work, the MoS_2 QDS will be used as security inks and get the fluorescent pattern invisible under ambient light. For this application. MoS_2 QDS will be first modified through surface functionalization using dual functional group polymers.

Moreover, the other 2D materials like Mxenes or TMDs will be exfoliated via liquid exfoliation method and chemical methods and their comparison will be demonstrated.

References

[1] A. Valizadeh, H. Mikaeili, M. Samiei, S.M. Farkhani, N. Zarghami, M. Kouhi, A. Akbarzadeh, S. Davaran, Quantum dots: synthesis, bioapplications, and toxicity., Nanoscale Res. Lett. 7 (2012) 480. doi:10.1186/1556-276X-7-480.

[2] H.D. Ha, D.J. Han, J.S. Choi, M. Park, T.S. Seo, Dual Role of Blue Luminescent MoS 2 Quantum Dots in Fluorescence Resonance Energy Transfer Phenomenon, Small. 10 (2014) 3858–3862. doi:10.1002/smll.201400988.

[3] V. Nicolosi, M. Chhowalla, M.G. Kanatzidis, M.S. Strano, J.N. Coleman, Liquid Exfoliation of Layered Materials, Science (80-.). 340 (2013) 1226419–1226419. doi:10.1126/science.1226419.

[4] A. O'Neill, U. Khan, J.N. Coleman, Preparation of High Concentration Dispersions of Exfoliated MoS 2 with Increased Flake Size, Chem. Mater. 24 (2012) 2414–2421. doi:10.1021/cm301515z.

[5] J.N. Coleman, M. Lotya, A. O'Neill, S.D. Bergin, P.J. King, U. Khan, K. Young, A. Gaucher, S. De, R.J. Smith, I. V Shvets, S.K. Arora, G. Stanton, H.-Y. Kim, K. Lee, G.T. Kim, G.S. Duesberg, T. Hallam, J.J. Boland, J.J. Wang, J.F. Donegan, J.C. Grunlan, G. Moriarty, A. Shmeliov, R.J. Nicholls, J.M. Perkins, E.M. Grieveson, K. Theuwissen, D.W. McComb, P.D. Nellist, V. Nicolosi, Two-dimensional nanosheets produced by liquid exfoliation of layered materials., Science. 331 (2011) 568–71. doi:10.1126/science.1194975.

[6] L. Tao, H. Long, B. Zhou, S.F. Yu, S.P. Lau, Y. Chai, K.H. Fung, Y.H. Tsang, J. Yao, D. Xu, Preparation and characterization of few-layer MoS2 nanosheets and their good nonlinear optical responses in the PMMA matrix., Nanoscale. 6 (2014) 9713–9. doi:10.1039/c4nr02664k.

[7] J. Wu, H. Li, Z. Yin, H. Li, J. Liu, X. Cao, Q. Zhang, H. Zhang, Layer thinning and etching of mechanically exfoliated MoS2 nanosheets by thermal annealing in air., Small. 9 (2013) 3314–9. doi:10.1002/smll.201301542.

[8] D.J. Late, B. Liu, H.S.S.R. Matte, C.N.R. Rao, V.P. Dravid, Rapid Characterization of Ultrathin Layers of Chalcogenides on SiO2/Si Substrates, Adv. Funct. Mater. 22 (2012) 1894–1905. doi:10.1002/adfm.201102913.

[9] H. Li, X. Qi, J. Wu, Z. Zeng, J. Wei, H. Zhang, Investigation of MoS_2 and graphene nanosheets by magnetic force microscopy., ACS Nano. 7 (2013) 2842–9. doi:10.1021/nn400443u.

[10] A. Splendiani, L. Sun, Y. Zhang, T. Li, J. Kim, C.-Y. Chim, G. Galli, F. Wang, Emerging photoluminescence in monolayer MoS2., Nano Lett. 10 (2010) 1271–5. doi:10.1021/nl903868w.

[11] G. Eda, H. Yamaguchi, D. Voiry, T. Fujita, M. Chen, M. Chhowalla, Photoluminescence from chemically exfoliated MoS2., Nano Lett. 11 (2011) 5111–6. doi:10.1021/nl201874w.

[12] C. Zhu, Z. Zeng, H. Li, F. Li, C. Fan, H. Zhang, Single-layer MoS2-based nanoprobes for homogeneous detection of biomolecules., J. Am. Chem. Soc. 135 (2013) 5998–6001. doi:10.1021/ja4019572.

[13] J. Zheng, H. Zhang, S. Dong, Y. Liu, C.T. Nai, H.S. Shin, H.Y. Jeong, B. Liu, K.P. Loh, High yield exfoliation of two-dimensional chalcogenides using sodium naphthalenide., Nat. Commun. 5 (2014) 2995. doi:10.1038/ncomms3995.

[14] K. Huang, L. Wang, Y.-J. Liu, Y. Liu, H.-B. Wang, T. Gan, L. Wang, Layered MoS2–graphene composites for supercapacitor applications with enhanced capacitive performance, Int. J. Hydrogen Energy. 38 (2013) 14027–14034. doi:10.1016/j.ijhydene.2013.08.112.

[15] A.B. Laursen, S. Kegnæs, S. Dahl, I. Chorkendorff, Molybdenum sulfides—efficient and viable materials for electro - and photoelectrocatalytic hydrogen evolution, Energy Environ. Sci. 5 (2012) 5577. doi:10.1039/c2ee02618j.

[16] J. Kibsgaard, Z. Chen, B.N. Reinecke, T.F. Jaramillo, Engineering the surface structure of MoS2 to preferentially expose active edge sites for electrocatalysis., Nat. Mater. 11 (2012) 963–9. doi:10.1038/nmat3439.

[17] H. Li, Z. Yin, Q. He, H. Li, X. Huang, G. Lu, D.W.H. Fam, A.I.Y. Tok, Q. Zhang, H. Zhang, Fabrication of single- and multilayer MoS2 film-based field-effect transistors for sensing NO at room temperature., Small. 8 (2012) 63–7. doi:10.1002/smll.201101016.

[18] W. Sik Hwang, M. Remskar, R. Yan, T. Kosel, J. Kyung Park, B. Jin Cho, W. Haensch, H. (Grace) Xing, A. Seabaugh, D. Jena, Comparative study of chemically synthesized and exfoliated multilayer MoS2 field-effect transistors, Appl. Phys. Lett. 102 (2013) 43116. doi:10.1063/1.4789975.

[19] W. Gu, J. Shen, X. Ma, Fabrication and electrical properties of MoS2 nanodisc-based back-gated field effect transistors., Nanoscale Res. Lett. 9 (2014) 100. doi:10.1186/1556-276X-9-100.

[20] E. Gourmelon, O. Lignier, H. Hadouda, G. Couturier, J.C. Bernède, J. Tedd, J. Pouzet, J. Salardenne, MS2 (M = W, Mo) photosensitive thin films for solar cells, Sol. Energy Mater. Sol. Cells. 46 (1997) 115–121. doi:10.1016/S0927-0248(96)00096-7.

[21] G. Kline, K.K. Kam, R. Ziegler, B.A. Parkinson, Further studies of the photoelectrochemical properties of the group VI transition metal dichalcogenides, Sol. Energy Mater. 6 (1982) 337–350. doi:10.1016/0165-1633(82)90039-9.

[22] P. Song, Q. Wang, Z. Yang, Biomorphic synthesis of ZnSnO3 hollow fibers for gas sensing application, Sensors Actuators B Chem. 156 (2011) 983–989. doi:10.1016/j.snb.2011.03.017.

[23] N.D. Md Sin, N. Khadijah, M.H. Mamat, M.Z. Musa, M. Rusop Mahmood, Influence of Cubic Structured-$ZnSnO_3$ Immersion Time to the Performance of Humidity Sensor, Nano Hybrids. 2 (2012) 1–11. doi:10.4028/www.scientific.net/NH.2.1.

[24] K.Y. Lee, D. Kim, J.-H. Lee, T.Y. Kim, M.K. Gupta, S.-W. Kim, Unidirectional High-Power Generation via Stress-Induced Dipole Alignment from ZnSnO 3 Nanocubes/Polymer Hybrid Piezoelectric Nanogenerator, Adv. Funct. Mater. 24 (2014) 37–43. doi:10.1002/adfm.201301379.

[25] G. Siddiqui, J. Ali, Y.-H. Doh, K.H. Choi, Fabrication of zinc stannate based all-printed resistive switching device, Mater. Lett. 166 (2016) 311–316. doi:10.1016/j.matlet.2015.12.045.

[26] J. Zeng, M. Xin, H. Wang, H. Yan, W. Zhang, Transformation Process and

Photocatalytic Activities of Hydrothermally Synthesized Zn 2 SnO 4 Nanocrystals, J. Phys. Chem. C. 112 (2008) 4159–4167. doi:10.1021/jp7113797.

[27] A. Okada, A. Usuki, The chemistry of polymer-clay hybrids, Mater. Sci. Eng. C. 3 (1995) 109–115. doi:10.1016/0928-4931(95)00110-7.

[28] J.W. Gilman, Flammability and thermal stability studies of polymer layered-silicate (clay) nanocomposites, Appl. Clay Sci. 15 (1999) 31–49. doi:10.1016/S0169-1317(99)00019-8.

[29] S. Kim, J. Ok, M. Ahn, D. Park, G. Lee, Electrical Properties of Organic/Inorganic Hybrid Composites for Insulation Materials, Trans. Electr. Electron. Mater. 3 (2002) 9–13. doi:10.4313/TEEM.2002.3.1.009.

[30] A.A. Novakova, V.Y. Lanchinskaya, A. V. Volkov, T.S. Gendler, T.Y. Kiseleva, M.A. Moskvina, S.B. Zezin, Magnetic properties of polymer nanocomposites containing iron oxide nanoparticles, in: J. Magn. Magn. Mater., 2003: pp. 354–357. doi:10.1016/S0304-8853(02)01062-4.

[31] G. Cunningham, M. Lotya, C.S. Cucinotta, S. Sanvito, S.D. Bergin, R. Menzel, M.S.P. Shaffer, J.N. Coleman, Solvent exfoliation of transition metal dichalcogenides: dispersibility of exfoliated nanosheets varies only weakly between compounds., ACS Nano. 6 (2012) 3468–80. doi:10.1021/nn300503e.

[32] T. Skaltsas, N. Karousis, H.-J. Yan, C.-R. Wang, S. Pispas, N. Tagmatarchis, Graphene exfoliation in organic solvents and switching solubility in aqueous media with the aid of amphiphilic block copolymers, J. Mater. Chem. 22 (2012) 21507. doi:10.1039/c2jm33245k.

[33] S. Stankovich, D. a. Dikin, R.D. Piner, K. a. Kohlhaas, A. Kleinhammes, Y. Jia, Y. Wu, S.T. Nguyen, R.S. Ruoff, Synthesis of graphene-based nanosheets via chemical reduction of exfoliated graphite oxide, Carbon N. Y. 45 (2007) 1558–1565. doi:10.1016/j.carbon.2007.02.034.

[34] Y. Yao, L. Tolentino, Z. Yang, X. Song, W. Zhang, Y. Chen, C. Wong, High-Concentration Aqueous Dispersions of MoS 2, Adv. Funct. Mater. 23 (2013) 3577–3583. doi:10.1002/adfm.201201843.

[35] X. Yu, M.S. Prévot, K. Sivula, Multiflake Thin Film Electronic Devices of Solution Processed 2D MoS 2 Enabled by Sonopolymer Assisted Exfoliation and Surface Modification, Chem. Mater. 26 (2014) 5892–5899. doi:10.1021/cm502378g.

[36] R.J. Smith, P.J. King, M. Lotya, C. Wirtz, U. Khan, S. De, A. O'Neill, G.S. Duesberg, J.C. Grunlan, G. Moriarty, J. Chen, J. Wang, A.I. Minett, V. Nicolosi, J.N. Coleman, Large-scale exfoliation of inorganic layered compounds in aqueous surfactant solutions., Adv. Mater. 23 (2011) 3944–8. doi:10.1002/adma.201102584.

[37] K.-G. Zhou, N.-N. Mao, H.-X. Wang, Y. Peng, H.-L. Zhang, A Mixed-Solvent Strategy for Efficient Exfoliation of Inorganic Graphene Analogues, Angew. Chemie Int. Ed. 50 (2011) 10839–10842. doi:10.1002/anie.201105364.

[38] V. Štengl, J. Henych, Strongly luminescent monolayered MoS2 prepared by effective ultrasound exfoliation., Nanoscale. 5 (2013) 3387–94. doi:10.1039/c3nr00192j.

[39] H. Li, Q. Zhang, C.C.R. Yap, B.K. Tay, T.H.T. Edwin, A. Olivier, D. Baillargeat, From Bulk to Monolayer MoS2: Evolution of Raman Scattering, Adv. Funct. Mater. 22 (2012)

1385–1390. doi:10.1002/adfm.201102111.

[40] C. Lee, H. Yan, L.E. Brus, T.F. Heinz, J. Hone, S. Ryu, Anomalous lattice vibrations of single- and few-layer MoS2, ACS Nano. 4 (2010) 2695–2700. doi:10.1021/nn1003937.

[41] R. Anbazhagan, H.-J. Wang, H.-C. Tsai, R.-J. Jeng, Highly concentrated MoS 2 nanosheets in water achieved by thioglycolic acid as stabilizer and used as biomarkers, RSC Adv. 4 (2014) 42936–42941. doi:10.1039/C4RA07512A.

[42] D. Gao, M. Si, J. Li, J. Zhang, Z. Zhang, Z. Yang, D. Xue, Ferromagnetism in freestanding MoS2 nanosheets., Nanoscale Res. Lett. 8 (2013) 129. doi:10.1186/1556-276X-8-129.

[43] V. Chikan, D.F. Kelley, Size-dependent spectroscopy of MoS2 nanoclusters, J. Phys. Chem. B. 106 (2002) 3794–3804. doi:10.1021/jp011898x.

[44] C. Ma, Z. Zhou, H. Wei, Z. Yang, Z. Wang, Y. Zhang, Rapid large-scale preparation of ZnO nanowires for photocatalytic application, Nanoscale Res. Lett. 6 (2011) 536. doi:10.1186/1556-276X-6-536.

[45] X. Li, S. Sundaram, Y. El Gmili, T. Ayari, R. Puybaret, G. Patriarche, P.L. Voss, J.P. Salvestrini, A. Ougazzaden, Large-Area Two-Dimensional Layered Hexagonal Boron Nitride Grown on Sapphire by Metalorganic Vapor Phase Epitaxy, Cryst. Growth Des. 16 (2016) 3409–3415. doi:10.1021/acs.cgd.6b00398.

[46] G. Lu, T. Wu, Q. Yuan, H. Wang, H. Wang, F. Ding, X. Xie, M. Jiang, Synthesis of large single-crystal hexagonal boron nitride grains on Cu–Ni alloy, Nat. Commun. 6 (2015) 6160. doi:10.1038/ncomms7160.

[47] S.M. Kim, A. Hsu, M.H. Park, S.H. Chae, S.J. Yun, J.S. Lee, D.-H. Cho, W. Fang, C. Lee, T. Palacios, M. Dresselhaus, K.K. Kim, Y.H. Lee, J. Kong, Synthesis of large-area multilayer hexagonal boron nitride for high material performance., Nat. Commun. 6 (2015) 8662. doi:10.1038/ncomms9662.

[48] H. Fan, S. Ai, P. Ju, Room temperature synthesis of zinc hydroxystannate hollow core-shell microspheres and their hydrothermal growth of hollow core-shell polyhedral microcrystals, CrystEngComm. 13 (2011) 113. doi:10.1039/c0ce00050g.

[49] Y. Chen, L. Yu, Q. Li, Y. Wu, Q. Li, T. Wang, An evolution from 3D face-centered-cubic ZnSnO3 nanocubes to 2D orthorhombic ZnSnO3 nanosheets with excellent gas sensing performance., Nanotechnology. 23 (2012) 415501. doi:10.1088/0957-4484/23/41/415501.

[50] K.-H.H. Choi, M. Mustafa, J.-B.B. Ko, Y.-H.H. Doh, Investigation of electrostatic atomization of a conjugated polymer (poly[2-methoxy-5-(2′-ethylhexyloxy)-(p-phenylenevinylene)]) and its film characterization for organic diode applications, Thin Solid Films. 525 (2012) 40–44. doi:10.1016/j.tsf.2012.10.048.

[51] M. Mustafa, H.C. Kim, Y.H. Doh, K.H. Choi, Structural, optical, and electrical characterization of the poly[9,9-dioctylfluorenyl-2,7-diyl]-co-1,4-benzo-(2,1,3)-thiadiazole thin film fabricated by electrostatic spray technique, Polym. Eng. Sci. (2014). doi:10.1002/pen.23608.

[52] S. Sathish, B. Shekar, Preparation and characterization of nano scale PMMA thin films, Indian J. Pure Appl. Phys. 52 (2014) 64–67. http://nopr.niscair.res.in/handle/123456789/25145 (accessed July 12, 2014).

[53] B. Chandar Shekar, S. Sathish, B.T. Bhavyasree, B. Ranjith Kumar, Characterization of Nano Scale PMMA Films Prepared by FDC Technique for FET Applications, Adv. Mater. Res. 678 (2013) 309–315. doi:10.4028/www.scientific.net/AMR.678.309.

[54] G. Duan, C. Zhang, A. Li, X. Yang, L. Lu, X. Wang, Preparation and Characterization of Mesoporous Zirconia Made by Using a Poly (methyl methacrylate) Template., Nanoscale Res. Lett. 3 (2008) 118–22. doi:10.1007/s11671-008-9123-7.

[55] C. Hu, S. Chen, W. Zhang, F. Xie, J. Chen, X. Chen, SERS study on surface chain geometry of atactic poly (methyl methacrylate) film and nanosphere, J. Raman Spectrosc. 44 (2013) 1136–1143. doi:10.1002/jrs.4341.

[56] K.J. Thomas, M. Sheeba, V.P.N. Nampoori, C.P.G. Vallabhan, P. Radhakrishnan, Raman spectra of polymethyl methacrylate optical fibres excited by a 532 nm diode pumped solid state laser, J. Opt. A Pure Appl. Opt. 10 (2008) 55303. doi:10.1088/1464-4258/10/5/055303.

[57] E. Gharoy Ahangar, M.H. Abbaspour-Fard, N. Shahtahmassebi, M. Khojastehpour, P. Maddahi, Preparation and Characterization of PVA/ZnO Nanocomposite, J. Food Process. Preserv. 39 (2015) 1442–1451. doi:10.1111/jfpp.12363.

[58] M.I. Abd-Elrahman, Synthesis of Polyvinyl Alcohol–Zinc Oxide Composite by Mechanical Milling: Thermal and Infrared Studies, Nanoscale Microscale Thermophys. Eng. 17 (2013) 194–203. doi:10.1080/15567265.2013.776152.

[59] K.H. Choi, G.U. Siddiqui, B. Yang, M. Mustafa, Synthesis of ZnSnO3 nanocubes and thin film fabrication of (ZnSnO3/PMMA) composite through electrospray deposition, J. Mater. Sci. Mater. Electron. 26 (2015) 5690–5696. doi:10.1007/s10854-015-3121-1.

[60] Y. Wang, Z. Wang, P. Ma, H. Bai, W. Dong, Y. Xie, M. Chen, Strong nanocomposite reinforcement effects in poly(vinyl alcohol) with melanin nanoparticles, RSC Adv. 5 (2015) 72691–72698. doi:10.1039/C5RA12333J.

[61] Y. Shi, C. Hamsen, X. Jia, K.K. Kim, A. Reina, M. Hofmann, A.L. Hsu, K. Zhang, H. Li, Z. Juang, M.S. Dresselhaus, L. Li, J. Kong, Synthesis of Few-Layer Hexagonal Boron Nitride Thin Film by Chemical Vapor Deposition, (2010) 4134–4139. doi:10.1021/nl1023707.

[62] A.S. Nazarov, V.N. Demin, E.D. Grayfer, A.I. Bulavchenko, A.T. Arymbaeva, H.-J. Shin, J.-Y. Choi, V.E. Fedorov, Functionalization and Dispersion of Hexagonal Boron Nitride (h-BN) Nanosheets Treated with Inorganic Reagents, Chem. - An Asian J. 7 (2012) 554–560. doi:10.1002/asia.201100710.

[63] H.S. Mansur, C.M. Sadahira, A.N. Souza, A.A.P. Mansur, FTIR spectroscopy characterization of poly (vinyl alcohol) hydrogel with different hydrolysis degree and chemically crosslinked with glutaraldehyde, Mater. Sci. Eng. C. 28 (2008) 539–548. doi:10.1016/j.msec.2007.10.088.

[64] E.F. dos Reis, F.S. Campos, A.P. Lage, R.C. Leite, L.G. Heneine, W.L. Vasconcelos, Z.I.P. Lobato, H.S. Mansur, Synthesis and characterization of poly (vinyl alcohol) hydrogels and hybrids for rMPB70 protein adsorption, Mater. Res. 9 (2006) 185–191. doi:10.1590/S1516-14392006000200014.

[65] N. Duraisamy, N.M. Muhammad, A. Ali, J. Jo, K.H. Choi, Characterization of poly(3,4-ethylenedioxythiophene):poly(styrenesulfonate) thin film deposited through

electrohydrodynamic atomization technique, Mater. Lett. 83 (2012) 80–83. doi:10.1016/j.matlet.2012.05.127.

[66] N.M. Muhammad, A.M. Naeem, N. Duraisamy, D.-S. Kim, K.-H. Choi, Fabrication of high quality zinc-oxide layers through electrohydrodynamic atomization, Thin Solid Films. 520 (2012) 1751–1756. doi:10.1016/j.tsf.2011.08.065.

[67] M. Maria, D. Navaneethan, K.H. Chan, H.M. Taek, C.K. Hyun, Solution processed fabrication of single wall carbon nanotubes thin film by electrohydrodynamic atomization deposition technique and its characterization, Appl. Phys. A. 109 (2012) 515–522. doi:10.1007/s00339-012-7302-y.

[68] A. Ali, K. Ali, K.-R. Kwon, M.T. Hyun, K.H. Choi, Electrohydrodynamic atomization approach to graphene/zinc oxide film fabrication for application in electronic devices, J. Mater. Sci. Mater. Electron. 25 (2013) 1097–1104. doi:10.1007/s10854-013-1693-1.

[69] M. Zubair, M. Mustafa, K. Lee, C. Yoon, Y.H. Doh, K.H. Choi, Fabrication of CdSe/ZnS quantum dots thin film by electrohydrodynamics atomization technique for solution based flexible hybrid OLED application, Chem. Eng. J. 253 (2014) 325–331. doi:10.1016/j.cej.2014.05.067.

[70] H.-D. Kim, H.-M. An, Y.M. Sung, H. Im, T.G. Kim, Bipolar Resistive-Switching Phenomena and Resistive-Switching Mechanisms Observed in Zirconium Nitride-Based Resistive-Switching Memory Cells, IEEE Trans. Device Mater. Reliab. 13 (2013) 252–257. doi:10.1109/TDMR.2012.2237404.

[71] U. Celano, L. Goux, A. Belmonte, K. Opsomer, A. Franquet, A. Schulze, C. Detavernier, O. Richard, H. Bender, M. Jurczak, W. Vandervorst, Three-Dimensional Observation of the Conductive Filament in Nanoscaled Resistive Memory Devices, Nano Lett. 14 (2014) 2401–2406. doi:10.1021/nl500049g.

[72] B. Zhang, M. Fraenkl, J.M. Macak, T. Wagner, Ag filament and surface particle formation in Ag doped AsS2 thin film, Mater. Lett. 163 (2016) 4–7. doi:10.1016/j.matlet.2015.08.131.

[73] E. Yoo, M. Lyu, J.-H. Yun, C. Kang, Y. Choi, L. Wang, Bifunctional resistive switching behavior in an organolead halide perovskite based Ag/CH 3 NH 3 PbI 3−x Cl x /FTO structure, J. Mater. Chem. C. 4 (2016) 7824–7830. doi:10.1039/C6TC02503J.

[74] J. Kolar, J.M. Macak, K. Terabe, T. Wagner, Down-scaling of resistive switching to nanoscale using porous anodic alumina membranes, J. Mater. Chem. C. 2 (2014) 349–355. doi:10.1039/C3TC31969E.

[75] K. Oh, W. Jeon, S. Lee, One-Dimensional TiO 2 @Ag Nanoarchitectures with Interface-Mediated Implementation of Resistance-Switching Behavior in Polymer Nanocomposites, ACS Appl. Mater. Interfaces. 4 (2012) 5727–5731. doi:10.1021/am301362f.

[76] J. Huang, D. Ma, Electrical switching and memory behaviors in organic diodes based on polymer blend films treated by ultraviolet ozone, Appl. Phys. Lett. 105 (2014) 93303. doi:10.1063/1.4895122.

[77] Y.-C. Lai, D.-Y. Wang, I.-S. Huang, Y.-T. Chen, Y.-H. Hsu, T.-Y. Lin, H.-F. Meng, T.-C. Chang, Y.-J. Yang, C.-C. Chen, F.-C. Hsu, Y.-F. Chen, Low operation voltage macromolecular composite memory assisted by graphene nanoflakes, J. Mater. Chem.

C. 1 (2013) 552–559. doi:10.1039/C2TC00010E.

[78] Y.-M. Choi, E. Lee, T.-M. Lee, Mechanism of reverse-offset printing, J. Micromechanics Microengineering. 25 (2015) 75019. doi:10.1088/0960-1317/25/7/075019.

[79] K.L. Mendoza, A. Ortega, N.S. Kim, Optimization of UV LED-Curable Ink for Reverse-Offset Roll-to-Plate (RO-R2P) Printing, J. Electron. Mater. 44 (2015) 784–791. doi:10.1007/s11664-014-3506-6.

[80] S. Khan, Y.H. Doh, A. Khan, A. Rahman, K.H. Choi, D.S. Kim, Direct patterning and electrospray deposition through EHD for fabrication of printed thin film transistors, Curr. Appl. Phys. 11 (2011) S271–S279. doi:10.1016/j.cap.2010.11.044.

[81] J. Ouyang, Application of nanomaterials in two-terminal resistive-switching memory devices, Nano Rev. 1 (2010) 1–15. doi:10.3402/nano.v1i0.5118.

[82] A. Midya, N. Gogurla, S.K. Ray, Flexible and transparent resistive switching devices using Au nanoparticles decorated reduced graphene oxide in polyvinyl alcohol matrix, Curr. Appl. Phys. 15 (2015) 706–710. doi:http://dx.doi.org/10.1016/j.cap.2015.03.008.

[83] W.T. Kim, J.H. Jung, T.W. Kim, D.I. Son, Current bistability and carrier transport mechanisms of organic bistable devices based on hybrid Ag nanoparticle-polymethyl methacrylate polymer nanocomposites, Appl. Phys. Lett. 96 (2010) 253301. doi:10.1063/1.3453661.

[84] T.W. Kim, Y. Yang, F. Li, W.L. Kwan, Electrical memory devices based on inorganic/organic nanocomposites, NPG Asia Mater. 4 (2012) e18. doi:10.1038/am.2012.32.

[85] Y.-C. Lai, D.-Y. Wang, I.-S. Huang, Y.-T. Chen, Y.-H. Hsu, T.-Y. Lin, H.-F. Meng, T.-C. Chang, Y.-J. Yang, C.-C. Chen, F.-C. Hsu, Y.-F. Chen, Low operation voltage macromolecular composite memory assisted by graphene nanoflakes, J. Mater. Chem. C. 1 (2013) 552–559. doi:10.1039/C2TC00010E.

[86] K. Oh, W. Jeon, S. Lee, One-Dimensional TiO 2 @ Ag Nanoarchitectures with Interface- Mediated Implementation of Resistance-Switching Behavior in Polymer Nanocomposites, Appl. Mater. Interfaces. (2012) 5727−5731.

[87] S. Sarma, B.M. Mothudi, M.S. Dhlamini, Unipolar resistive switching behaviour of copper doped polyvinyl alcohol/lead sulphide quantum dot device, J. Mater. Sci. Mater. Electron. 27 (2016) 3785–3790. doi:10.1007/s10854-015-4223-5.

[88] D.S. Jeong, R. Thomas, R.S. Katiyar, J.F. Scott, H. Kohlstedt, A. Petraru, C.S. Hwang, Emerging memories: resistive switching mechanisms and current status, Reports Prog. Phys. 75 (2012) 76502. doi:10.1088/0034-4885/75/7/076502.

[89] H. Nili, S. Walia, S. Balendhran, D.B. Strukov, M. Bhaskaran, S. Sriram, Nanoscale Resistive Switching in Amorphous Perovskite Oxide (a- SrTiO 3) Memristors, Adv. Funct. Mater. 24 (2014) 6741–6750. doi:10.1002/adfm.201401278.

[90] J.-W. Park, M.K. Yang, J.-K. Lee, Electrode Dependence of Bipolar Resistive Switching in SrZrO[sub 3]:Cr Perovskite Film-Based Memory Devices, Electrochem. Solid-State Lett. 11 (2008) H226. doi:10.1149/1.2937460.

[91] Z. Ma, C. Wu, D.U. Lee, F. Li, T.W. Kim, Carrier transport and memory mechanisms

of multilevel resistive memory devices with an intermediate state based on double-stacked organic/inorganic nanocomposites, Org. Electron. 28 (2016) 20–24. doi:10.1016/j.orgel.2015.10.002.

[92] C. Gu, J.-S. Lee, Flexible Hybrid Organic–Inorganic Perovskite Memory, ACS Nano. (2016) acsnano.6b01643. doi:10.1021/acsnano.6b01643.

[93] Y. Liu, F. Li, Z. Chen, T. Guo, C. Wu, T.W. Kim, Resistive switching memory based on organic/inorganic hybrid perovskite materials, Vacuum. 130 (2016) 109–112. doi:10.1016/j.vacuum.2016.05.010.

[94] B. Singh, B.R. Mehta, D. Varandani, Govind, A. Narita, X. Feng, K. Müllen, Bipolar resistive switching properties of Ti-CuO/(hexafluoro-hexa-peri-hexabenzocoronene)-Cu hybrid interface device: Influence of electronic nature of organic layer, J. Appl. Phys. 113 (2013) 203706. doi:10.1063/1.4807411.

[95] T.W. Kim, Y. Yang, F. Li, W.L. Kwan, Electrical memory devices based on inorganic/organic nanocomposites, NPG Asia Mater. 4 (2012) e18. doi:10.1038/am.2012.32.

[96] S. ChandraKishore, a. Pandurangan, Facile synthesis of carbon nanotubes and their use in the fabrication of resistive switching memory devices, RSC Adv. 4 (2014) 9905–9911. doi:10.1039/c3ra45359f.

[97] S. Sarma, Possible application of lead sulfide quantum dot in memory device, J. Polym. Eng. 36 (2016). doi:10.1515/polyeng-2015-0115.

[98] S. Walia, S. Balendhran, Y. Wang, R. Ab Kadir, A. Sabirin Zoolfakar, P. Atkin, J. Zhen Ou, S. Sriram, K. Kalantar-zadeh, M. Bhaskaran, Characterization of metal contacts for two-dimensional MoS2 nanoflakes, Appl. Phys. Lett. 103 (2013) 232105. doi:10.1063/1.4840317.

[99] Y.-M. Choi, E.-S. Lee, T.-M. Lee, K.-Y. Kim, Optimization of a reverse-offset printing process and its application to a metal mesh touch screen sensor, Microelectron. Eng. 134 (2015) 1–6. doi:10.1016/j.mee.2014.12.007.

[100] M.M. Rehman, G.U. Siddiqui, J.Z. Gul, S. Kim, J.H. Lim, K.H. Choi, Resistive Switching in All-Printed, Flexible and Hybrid MoS2-PVA Nanocomposite based Memristive Device Fabricated by Reverse Offset, Sci. Rep. 6 (2016) 36195. doi:10.1038/srep36195.

[101] N.M. Muhammad, A.M. Naeem, N. Duraisamy, D.-S. Kim, K.-H. Choi, Fabrication of high quality zinc-oxide layers through electrohydrodynamic atomization, Thin Solid Films. 520 (2012) 1751–1756. doi:10.1016/j.tsf.2011.08.065.

[102] K.H. Choi, M. Mustafa, K. Rahman, B.K. Jeong, Y.H. Doh, Cost-effective fabrication of memristive devices with ZnO thin film using printed electronics technologies, Appl. Phys. A Mater. Sci. Process. 106 (2012) 165–170. doi:10.1007/s00339-011-6670-z.

[103] N. Duraisamy, N.M. Muhammad, H.-C. Kim, J.-D. Jo, K.-H. Choi, Fabrication of TiO2 thin film memristor device using electrohydrodynamic inkjet printing, Thin Solid Films. 520 (2012) 5070–5074. doi:10.1016/j.tsf.2012.03.003.

[104] A. Ali, J. Jo, Y.J. Yang, K.H. Choi, Direct fabrication of graphene/zinc oxide composite film and its characterizations, Appl. Phys. A Mater. Sci. Process. 114 (2014) 323–330. doi:10.1007/s00339-013-8136-y.

[105] S. Lee, J. Park, M. Lee, J.J. Boland, Multilevel resistance in ZnO nanowire memristors enabled by hydrogen annealing treatment, AIP Adv. 6 (2016) 125010. doi:10.1063/1.4971820.

[106] J. Park, H. Song, E.K. Lee, J.H. Oh, K. Yong, ZnO Nanowire Based Photoelectrical Resistive Switches for Flexible Memory, J. Electrochem. Soc. 162 (2015) H713–H718. doi:10.1149/2.1111509jes.

[107] R. Nohria, R.K. Khillan, Y. Su, R. Dikshit, Y. Lvov, K. Varahramyan, Humidity sensor based on ultrathin polyaniline film deposited using layer-by-layer nano-assembly, 114 (2006) 218–222. doi:10.1016/j.snb.2005.04.034.

[108] M. V. Kulkarni, S.K. Apte, S.D. Naik, J.D. Ambekar, B.B. Kale, Ink-jet printed conducting polyaniline based flexible humidity sensor, Sensors Actuators B Chem. 178 (2013) 140–143. doi:10.1016/j.snb.2012.12.046.

[109] S. Borini, R. White, D. Wei, M. Astley, S. Haque, E. Spigone, N. Harris, J. Kivioja, T. Ryhänen, Ultrafast graphene oxide humidity sensors, ACS Nano. 7 (2013) 11166–11173.

[110] X. Dong, T. Li, Y. Liu, Y. Li, C.-L. Zhao, C.C. Chan, Polyvinyl alcohol-coated hybrid fiber grating for relative humidity sensing., J. Biomed. Opt. 16 (2011) 77001. doi:10.1117/1.3595845.

[111] M. Sajid, S. Aziz, G.B. Kim, S.W. Kim, J. Jo, K.H. Choi, Bio-compatible organic humidity sensor transferred to arbitrary surfaces fabricated using single-cell-thick onion membrane as both the substrate and sensing layer, Sci. Rep. 6 (2016) 30065. doi:10.1038/srep30065.

[112] P. Karthick, R. Saraswathi, J. Bosco, B. Rayappan, Sensors and Actuators A : Physical A highly sensitive humidity sensor based on DC reactive magnetron sputtered zinc oxide thin film, Sensors Actuators A. Phys. 164 (2010) 8–14. doi:10.1016/j.sna.2010.09.006.

[113] Y.-C. Hu, C.-L. Dai, C.-C. Hsu, Titanium dioxide nanoparticle humidity microsensors integrated with circuitry on-a-chip., Sensors (Basel). 14 (2014) 4177–88. doi:10.3390/s140304177.

[114] M. Yang, Y. Li, X. Zhan, M. Ling, A Novel Resistive-Type Humidity Sensor Based on Poly (p-diethynylbenzene), 74 (2015) 2010–2015.

[115] Y. Li, M.J. Yang, Bilayer thin film humidity sensors based on sodium polystyrenesulfonate and substituted polyacetylenes, Sensors Actuators, B Chem. 87 (2002) 184–189. doi:10.1016/S0925-4005(02)00233-2.

[116] M. Chen, C. Hsu, T. Hsueh, Fabrication of Humidity Sensor Based on Bilayer Graphene, 35 (2014) 590–592.

[117] Y. Yao, X. Chen, H. Guo, Z. Wu, X. Li, Sensors and Actuators B : Chemical Humidity sensing behaviors of graphene oxide-silicon bi-layer flexible structure, Sensors Actuators B Chem. Journa. 161 (2012) 1053–1058. doi:10.1016/j.snb.2011.12.007.

[118] I. Ferroelectrics, I. Tech, Electrical and Humidity Sensing Properties of Graphene and Polystyrene Sulfonic Sodium Bilayer Thin Film Integrated Ferroelectrics : An Properties of Graphene and Polystyrene, (2013). doi:10.1080/10584587.2013.787828.

[119] Y. Li, K. Fan, H. Ban, M. Yang, Sensors and Actuators B : Chemical Detection of very low humidity using polyelectrolyte / graphene bilayer humidity sensors, Sensors

Actuators B. Chem. 222 (2016) 151–158. doi:10.1016/j.snb.2015.08.052.

[120] K. Wang, X. Qian, L. Zhang, Y. Li, H. Liu, Inorganic − Organic p ‑ n Heterojunction Nanotree Arrays for a High- Sensitivity Diode Humidity Sensor, (2013).

[121] H. Yu, H.K. Kim, T. Kim, K.M. Bae, S.M. Seo, J. Kim, T.J. Kang, Y.H. Kim, Self-Powered Humidity Sensor Based on Graphene Oxide Composite Film Intercalated by Poly(Sodium 4 ‑ Styrenesulfonate), (2014).

[122] K. Jiang, H. Zhao, J. Dai, T. Fei, T. Zhang, Excellent Humidity Sensor Based on LiCl Loaded Hierarchically Porous Polymeric Microspheres, (2016). doi:10.1021/acsami.6b08071.

[123] R. Earths, Humidity sensing properties of Ce-doped nanoporous ZnO thin film prepared by sol-gel method, (2016). doi:10.1016/S1002-0721(10)60635-7.

[124] A.I. Buvailo, Y. Xing, J. Hines, N. Dollahon, E. Borguet, TiO 2 / LiCl-Based Nanostructured Thin Film for Humidity Sensor Applications, (2011) 528–533.